Application of calcium phosphate based gels for encapsulation of therapeutic molecules

by Peih-Jeng Jiang

A thesis submitted to the School of Chemical Engineering of the
University of Birmingham
for the degree of
Doctor of Philosophy

Chemical Engineering
University of Birmingham
Edgbaston, Birmingham
B15 2TT, UK

Abstract

There is increasing clinical need for bone substitutes because of the limited supply of autogenous tissue, and the significance of inherited or other bone diseases. The ultimate aim of this study was to form calcium phosphate (CaP) based matrices as bone grafts for medical applications. Amongst CaP based materials, CaP gels made by the sol-gel process have attracted much interest since they can be processed at room temperature allowing the incorporation of environmentally sensitive molecules such as growth factors. CaP gels can be engineered by changing process conditions. There is little previous work however on the effect of drying regimes on the CaP materials formed using the sol-gel process. The objectives of this research were to investigate the influence of drying conditions on the physicochemical properties of CaP gels and the effect of the resultant structures of CaP gels on the function of the incorporated therapeutic molecules. In addition, surface modification of the CaP gels was investigated as a means to enhance biological interaction and also a potential way of creating primary bonds between apatite crystals enabling mechanical reinforcement of the material, which is currently too weak to bear load. This work has confirmed that different drying regimes have a significant influence on the formation of the gel pore structure, with the storage of gel in humid conditions, enabling reprecipitation of an apatitic phase. This variation in pore structure has a significant influence on the catalytic of encapsulated enzymes. In addition, the pH fluctuation of CaP based matrices during processing determines the activity of biomolecules after incorporation. It has also been shown that it is possible to form thiol functional groups on the surface of CaP gels, which could be used in future for mechanical reinforcement or for the attachment of biological moieties.

Acknowledgments

I am deeply indebted to my supervisor Dr. Liam Grover who has supported, encouraged, and guided through my PhD. I would like to thank to the academic staff in the School of Chemical Engineering, including Dr. James Bowen, Dr. Paula Mendes and Dr. Rachel Bridson. I would also like to thank Dr. Adrian Wright who is in the School of Chemistry.

I would like to express my gratitude to all technicians and staff who have helped with a number of aspects of my PhD in Biochemical engineering, School of Chemistry and Centre for Microscopy. Especially, thank to Ms Elaine Mitchell, Mrs Ming Chu, and Mrs Theresa Morris.

Thanks to my colleagues who have been great support and encouragement during my PhD. I would like to thank my friends, in particular Clive and Margaret who have taken care of me and supported me.

Most importantly, I would like to thank my parents for their continual financial and emotional support, and encouragement.

To Dad, Mum, Clive, and Margaret

Table of contents

List of Figures

List of Tables

Chapter 1 Introduction

Human life expectancy has increased dramatically since the discovery of antiseptics, penicillin and other antibiotics, chemical treatment to improve hygiene, and vaccination [Hench and Wilson (1993)]. Since the mean age of the population of the developed world is continuosly increasing there is a large and growing need for materials to replace diseased and damaged hard tissues. At present, there are two possible treatments for bone disease, which are both used to replace hard tissue: 1) transplantation and 2) implantation. Although autograft is preferable, it is in limited supply, and lacks mechanical integrity. Alternative sources of hard tissue are obtained from other humans (allograft) or animals (xenograft). This resolves one difficulty-supply, but raises others, including immunological rejection and disease transmission. There is a need, therefore, for developing synthetic biomaterials for bone graft replacement. As the mineral component of bone consists mainly of calcium phosphate salts, calcium phosphate materials have become widely used as bone substitutes [LeGeros (2008)]. Calcium phosphate materials are osteoconductive, but for a successful clinical outcome, it is sometimes necessary to incorporate antibiotics, enzymes or other therapeutic molecules that are able to provide prophylactic treatment for osteomyelitis or can stimulate local bone formation.

Calcium phosphate materials have been used for clinical bone augmentation for over 30 years. Most of them are synthesised at high sintering temperatures [Itokazu et al. (1998), Saito et al. (2002)], which may destroy the activity of environmentally sensitive therapeutic molecules. In contrast, calcium phosphates formed by the sol-gel process are advantageous for the encapsulation of these molecules since this process can occur at room temperature. In a delivery system, there are many factors determining the activity of the incorporated molecules and their loading-efficiency. The activity of the therapeutic

molecules also depends on the physicochemical properties of the calcium phosphates, such as pore structure, and adhesive forces between the calcium phosphates and the biomolecules [Komleva et al. (2002), Fellah et al. (2007)]. Amongst these factors, pore structure has been demonstrated to be most important as it is critical to the rate of release from the structure. In previous studies, the pore structure of calcium phosphate based matrices has been modified by adding a porogen [Gabriel Chu et al. (2002), Ramay and Zhang (2003)], or using a freeze-drying processes [Lu et al. (1998), Zhang and Yokogawa (2008)], or controlled sintering temperature [Best and Bonfield (1994)]. There is little information about using different drying processes to control pore structure.

Effective delivery is partly related to the loading efficiency of the incorporated therapeutic molecules. Therefore, most research focuses on increasing efficacy of loading biomolecules into CaP ceramics [Habraken et al. (2009), Rawat et al. (2008)]. Few studies, however, have considered the causes of the reduction or loss of therapeutic activity. For example, a change in pore size distribution may result in mass transport limitations and influence the release behaviour of the incorporated molecules. In addition, variables such as pH may control both the release and performance of these biomolecules. Although there is little change in the temperature of CaP cements during setting which is similar to the CaP gel, there can be significant fluctuations in the pH of the setting cement slurries. Furthermore, the bonding between materials and biomolecules may control the loading efficiency. It has been demonstrated that chemical bonding increases the amount of loading of proteins, drugs, and enzymes [Wright et al. (2006), Nishioka et al. (2006)]. With effective loading, it is possible to avoid side effects, and toxic reactions because of overdoses [Radin et al. (1997)], in addition to promoting healing.

Alternatively, the type of bonding within materials may strengthen the structure of linking networks.

In this study, a variety of process conditions were applied during the fabrication of CaP gels on the assumption that the regimes would allow control over pore structure. The physicochemical properties of these resulting CaP gels were investigated. The resulting CaP gels were used as carriers or stores of antibiotics or enzymes. Although one major limitation of CaP gels is their low strength, the mechanical performance of the material is considered beyond the scope of this project. The effect of pore size on the release of vancomycin hydrochloride, horseradish peroxidase, and alkaline phosphatase was discussed. In addition, it was hypothesised that the bonding can be strengthened by forming a covalent bond with the surface of the CaP gels. Therefore, the introduction of thiol functional groups by reacting organosilanes with silicon substituted CaP gels is suggested in the expectation of increase the numbers of potential binding sites of functional groups.

Chapter 2 Bone and Bone replacement

2.1 Bone

2.1.1 Composition of bone

Bone is a living tissue composed predominantly of mineral (inorganic material) and protein (organic material). The biological component includes cells, fat, natural polymers such as polysaccharides, collagen, and polyphosphates [Ravaglioli and Krajewski (1992)]. Bone cells include osteoblasts, osteoclasts, osteocytes, osteoprogenitors and bone-lining cells [LeGeros (2008), Miller (1987)]. The main constituents of bone are 70 wt% of calcium phosphate minerals, 22 wt% of collagen, and 8 wt% of water [Suchanek and Yoshimura (1998), Bilezikian et al. (1996)]. The mineral constituent of bone is hydroxyapatite (HA) (formed predominantly of calcium and phosphate ions) with a trace amount of ions such as CO_3^{2-}, Mg^{2+}, Fe^{2+}, Na^{+}, K^{+}, and F^{-}, Cl^{-}. Some specific heavy metals, for example, Ba^{2+}, S^{2+}, Pb^{2+}, may occasionally be found [Ravaglioli and Krajewski (1992)]. Amongst these minor ions, carbonate (7.4 wt%), sodium (0.9 wt%) and magnesium (0.72 wt%) are the most important. The collagens are fibrous proteins composed of tropocollagen macromolecules [Hancox (1972)].

2.1.2 Bone cells

Bone cells play important roles in maintaining and remodelling the structure of bone. There are five types of bone cells present in the matrix of bone (Figure 2.1). The following section describes the function of these cells.

Osteoblasts

Osteoblasts are responsible for the production and mineralisation of the bone matrix [LeGeros (2008)]. To produce bone, osteoblasts of mesenchymal origin secrete collagen fibres, which then self-assemble to form segments or plates of the osteoids (non-calcified

bone matrix) and this subsequently becomes mineralised. The process of mineralisation occurs by the addition of HA to the collagen matrix, which is mediated by matrix vesicles exocytosed by the osteoblasts [Hessle et al. (2002)]. As mineralisation proceeds, the number of osteoblasts progressively reduces with time. Osteoblasts are localised particularly in the periosteal membrane. Osteoblasts are confined within their osteoid shells inside the bone matrix. When osteoblasts approach the end of their activity, they are encapsulated in bone matrix and subsequently differentiate to form osteocytes. The presence of osteoblasts is often evidenced by the activity of alkaline phosphatase, an enzyme synonymous with bone formation [Ravaglioli and Krajewski (1992)].

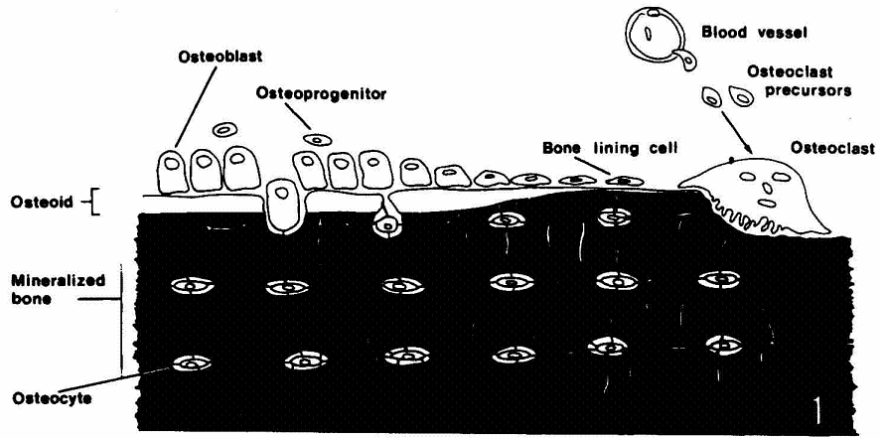

Figure 2.1 A schematic diagram showing the location of cells on bone (taken from Mark and Popoff 1988). Osteoblasts, osteoclasts, and bone lining cell are present on the bone surface, but osteocytes are encapsulated in the mineralised interior. In addition, osteoblasts, osteocytes, and bone-lining cells are derived from local osteoprogenitor cells. The osteoclast, however, originates from the fusion of mononuclear precursors.

Osteocytes

Osteocytes are mature osteoblasts within the bone matrix and are thought to be responsible for osteoblast maintenance, among other roles [Bilezikian et al. (1996)]. Each osteocyte is derived from an osteoblast through a complex change of form and activity.

The function of osteocytes is controversial, but most probably they act as a mechanical and metabolic pump for the bone lymphatic flow, a regulator of mineralisation and enable bone to respond to the application of applied loads [Ravaglioli and Krajewski (1992)].

Osteoclasts

Osteoclasts are responsible for resorption of bone and maintain the bone matrix [LeGeros (2008)]. Osteoclasts are derived from the mononuclear lineage of cells found in blood [Vaughan (1981)]. Active osteoclasts are polarised cells, originating from haemopoietic precursors in the bone marrow where they are composed of a baso-lateral membrane and an apical zone. An apical zone includes the light zone and the brush border (or striated border). The working space where osteoclasts dissolve the bone matrix is defined by the brush border and forms an envelope. This enclosed environment where the osteoclasts cause resorption exhibits a pH value of 4.5 (ruffled border). The ruffled border is often used to identify active osteoclasts [Ravaglioli and Krajewski (1992), Teitelbaum (2000)].

Osteoprogenitors

Osteoprogenitors are derived from cells present in the bone marrow or an inducing agent, capable of forming bone. Osteoprogenitors are located in the periosteum and the bone marrow [Vaughan (1981)]. Osteoprogenitor cells are the cells from which osteoblasts and osteocytes are differentiated [Ravaglioli and Krajewski (1992)].

Bone-lining cells

The bone-lining cells are flat mesenchymal cells that inactively line bone surfaces. Bone-lining cells contain the greatest fraction of membranes in an adult skeleton, and they separate the bone fluids from the interstitial fluids, and regulate mineral homeostasis. The bone-lining cell is also considered as support cells for osteocytes [Miller (1987)].

2.1.3 The structure of bone

Mineralised bone can be organised to form woven or lamellar bone (Figure 2.2). Microscopically, the collagenous fibres are 80-100 nm in thickness and 100-2000 Å in diameter [Suchanek and Yoshimura (1998), Dorozhkin and Epple (2002)]. The calcium phosphate ions are in the form of crystalline hydroxyapatite (HA) and/or amorphous calcium phosphates. The crystals of HA are plates or needles with size of length 50 nm, width 25 nm, and thickness 4 nm (Figure 2.3) [Suchanek and Yoshimura (1998)].

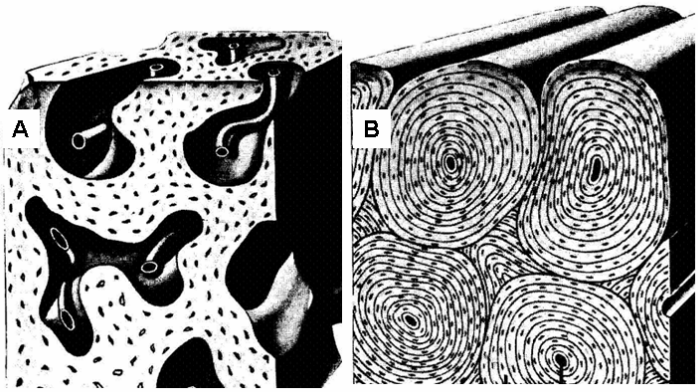

Figure 2.2 (A) Woven bone is composed of large and tortuous channels; (B) lamellar bone is formed by Haversian canals and a regular arrangement of osteocytes (taken from Hancox (1972))

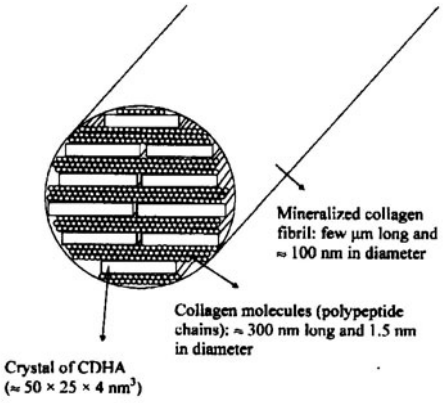

Figure 2.3 The mineralised collagen fibrils which range from a few μm in length and 100 nm in diameter and are composed of polypeptides with approximately 300 nm in length and 1.5 nm in diameter. The crystal of carbonated deficient HA (CDHA) is 5000 nm^3 (taken from Dorozhkin and Epple (2002)).

Both woven and lamellar bones may form either compact or cancellous bone, depending on the volume of vascular spaces [Hancox (1972]. Woven bone is composed of coarse collagenous fibres interweaving in all spatial directions and without an ordered arrangement. In addition, the osteocytes of woven bones are randomly distributed. In lamellar bones, the fibres are finer and organised into unit layers or sheets, and the osteocytes are evenly distributed. Bone exhibits a hierarchical structure usually consisting of a dense outer layer (compact bone) surrounding a less dense core (cancellous bone) [Hancox (1972), Dorozhkin and Epple (2002)].

Generally, bone formation can be divided into two stages. The first includes synthesis and extracellular assembly of the collagen I matrix, which is followed by mineralisation. The HA crystals precipitate in a parallel orientation into the regions known as hole-zones of the collagen matrix [Dorozhkin and Epple (2002)].

2.1.4 Types of bone

Compact bone (Cortical bone)

Compact bones are made up of densely packed vascular canals, which form concentric lamellae. Fibrils in neighbouring lamellae are arranged perpendicular to one another [Bilezikian et al. (1996)]. Such a vascular canal together with its adjacent concentric lamellae is defined as a Haversian canal or osteon [Hancox (1972)]. In the Haversian system, there are blood vessels which deliver nutrients to the cellular components of the bone along Haversian canals [Suchanek and Yoshimura (1993)]. Compact bone has a low surface area because of its high density [Dorozhkin (2007)]. The structure of compact bone fulfils mechanical and protective functions, including: supporting the body, protecting organs, and providing levers for movement.

Cancellous bone (Spongy bone)

Cancellous bones are composed of loosely packed trabeculae with an open network-like structure, and therefore, they have a high surface area [Dorozhkin (2007)], precluding the need for the presence of significant numbers of blood vessels. The structure of cancellous bone provides the metabolic function such as hematopoiesis, exchange of calcium ions [Bilezikian et al. (1996)]. In addition, cancellous bone is considerably lighter than compact bone and so plays a weight saving role. It is also thought that cancellous bone has greater impact resistance.

2.2 Clinical need for bone replacement

Over time, medical care has developed and, for this and other reasons, human life expectancy has increased. In terms of bone disease, this poses particular problems since the mechanical integrity of the skeleton tends to decrease with age. In addition, the highly

organised structure of bone can make treatment very difficult. Here, both bone disease and synthetic biomaterials for bone replacement are described.

2.3 Bone disease and treatment

Bone diseases can occur because of congenital disorder; age; or infection. Whatever the cause, it is without doubt that new and effective treatment is required. In this section, some frequently encountered diseases are briefly described.

2.3.1 Disease

Osteomyelitis

Osteomyelitis is a kind of bacterial infection caused by pyrogenic bacteria, mycobacteria or fungi. Osteomyelitis, depending on its aetiology, is either a haematogenous or a contiguous focus of infection. Haematogenous osteomyelitis usually occurs in paediatric patients. A contiguous focus of infection results from inoculation of bacteria into bone at the time of trauma or during surgical operation on a fracture. *Staphylococcus aureus* is usually the microorganism responsible for the infection [Conterno and da Silva Filho (2009)]. The treatment of osteomyelitis includes antibiotic therapy, and resection of infected bone which, sometimes requires a bone replacement.

Osteoporosis

Osteoporosis is a disorder characterised by the reduction of bone density, which may cause thinner trabeculae and larger resorption cavities. There is no alteration of the external structure of remnant bone. Osteoporosis is associated with ageing, especially of women after the menopause. It is rarely found in younger people, except for idiopathic osteoporosis. Oestrogen is used as a treatment [Vaughan (1981), Hancox (1972),]. Also, it has been demonstrated that bone graft combined with pulsing electromagnetic fields

reduce bone loss [Bassett et al. (1982)] and the administration of oestrogen directly or indirectly to osteoblasts and osteoclasts by delivering oestrogens from HA [Ishizaki et al. (2009)].

Hypophosphatasia

Hypophosphatasia is an inherited disorder, characterised by defective bone and tooth mineralisastion and deficiency of serum and bone alkaline phosphatase activity. This disease results from mutations in the liver/bone/kidney alkaline phosphatase gene. The treatment includes bone marrow cell transplantation and plasma cell membrane glycoprotein-1 gene [Mornet (2008)]. Alkaline phosphatase was delivered to the bone by incorporating into HA, it was suggested that the localisation of alkaline phosphatase can induce bone mineralisation [Ishizaki et al. (2009)].

Osteogenesis imperfecta

Osteogenesis imperfecta is a rare autosomal disorder of bone characterised by brittle bone and defective connective tissue. This disease is due to the deficiency of Type I collagen. As a genetic disorder, osteogenesis imperfecta mostly occurs through parental inheritance, but in a few cases it is due to an individual genetic mutation [Vaughan (1981)]. An intramedullary rod system composed of stainless steel has been developed to treat osteogenesis imperfecta [Wilkinson et al. (1998)].

2.4 Autograft

Autograft is bone obtained from another anatomic site of the same human body [LeGeros (2008), Hench (1998)]. Autograft is the gold standard for bone repair, but it has limitations, including possible morbidity of the donor site, the limited volume of donor

bone, and also anatomical and structural problems, and increased resorption during healing [Ducheyne and Qiu (1999)].

2.5 Allograft

An alternative to autograft is allogeneic bone. Allograft is harvested from another human body. The allograft, however, has disadvantages including limited supply, viral or bacterial transmission, and immune rejection [LeGeros (2008)]. The mechanism of allograft for the bone substitute is osteoconduction. Due to the chemical treatments applied to the tissue prior to treatment, however, no osteogeneration or osteoinduction occurs following implantation of allografts [Urist et al. (1994)].

2.6 Xenograft

Xenografts are bone which has been obtained from animal sources. Xenograft, however, is not widely used as a bone graft because of the risk of acute immune response. To avoid this biological reaction, donor bone is deproteinated and defatted, both of which reduce antigenic response. This treatment process results in the osteoinductive proteins found in the bone becoming damaged and thus xenografts are less likely to stimulate bone formation than other forms of tissue graft. This causes failure in a large proportion of implantations [Damien and Parsons (1991), Urist et al. (1994)].

2.7 Biomaterials for bone replacement

Due to both the shortcomings of allografts and the increasing requirement of materials for bone replacement, repair, and augmentation, there has been a considerable need to develop alternative biomaterials. The chief characteristics of suitable implant materials are biocompatibility in a bony site, ease of sterilisation and use, and price. Various commercial bone substitutes are already in use, including metals, polymers, corals,

processed cadaver bone, cow bone, and synthetic bioceramics [LeGeros (2008)]. The most clinically used bioceramics are calcium phosphates such as hydroxyapatite (HA), ß-tricalcium phosphates (β-TCP) as their compositions are similar to the mineral components of hard tissue. In this section, the bioceramic materials used as hard tissue replacements are described.

2.7.1 Bioceramics

The word ceramic derives from the Greek “Keramos”, meaning burnt-stuff or pottery [Anderson et al. (1990)]. Ceramics are inorganic and non-metallic materials, usually inorganic, including silicate, metallic oxides, and sulphides. Oxides such as Al_2O_3, MgO, SiO_2, and ZrO_2 contain metallic and non-metallic elements as well as ionic salts for example, NaCl, CsCl, and ZnS [Park and Bronzino (2003)]. According to the arrangement of their atoms, ceramics can be classified as amorphous and crystalline. In amorphous ceramics such as glasses, the order is only in the short-range. Polycrystalline ceramics are solids in which the atoms or ions are arranged in regular arrays [Park and Bronzino (2003), Hench and Jones (2005)].

Bioceramics are those ceramics mainly used for medical applications such as repair and reconstruction of bone defects and diseased or damaged musculoskeletal systems [Habraken et al. (2007)]. According to the biological response, bioceramics can be classified as 1) bioinert (alumina, zirconia, carbons), 2) bioactive (bioglass and Ceravital, and sintered HA), and 3) bioresorbable (biphasic calcium phosphate, β-TCP). These definitions are developed from the definitions put forward by Hulbert et al. who classified bioceramics as inert, surface reactive, and resorbable [Shackelford (1999)]. The distinct feature of a bioinert ceramic is extremely slow reaction kinetics with their environments.

In contrast, bioactive materials exhibit faster reaction kinetics that results in the formation of a bond with bone at the interface with the material. Hench et al. defined bioactivity as the formation of bonds between materials and bone. All bioactive materials are also osteoconductive [LeGeros (2008)]. A suitable bone substitute should lead to new bone forming from the graft bed into the bone defect [Urist et al. (1994)]. Osteoconductivity means that the matrix serves as a template or scaffold resulting in the formation of bone along its surface. The majority of calcium phosphates are known to be osteoconductive. Bioresorbable materials are those bioactive materials which can be replaced by hard tissue [Park and Bronzino (2003), Vallet-Regí (2001)] and include β-TCP and biphasic calcium phosphate.

2.7.2 Alumina, zirconia based ceramics

Alumina and zirconia ceramics were the first ceramics used for medical applications because of their perceived bioinertness *in vivo* [Vallet-Regí (2001), Urist et al. (1994)]. Due to their relatively high mechanical strengths, alumina and zirconia are suitable for bearing surfaces in joint replacement. Alumina used as an implant should contain 99.5 % pure alumina and less than 0.1 % of SiO_2 and alkali oxides according the American Society for Testing and Materials [Park and Bronzino (2003)]. Zirconia combined with Y_2O_3 has been used for implantation of bone [Hentrich et al. (1971)].

2.7.3 Poly(methyl methacrylate) (PMMA)

Poly(methyl methacrylate) (PMMA) beads or cements have been used widely as bone grafts. One problem, however, is that they do not form an intimate attachment to bone and some authors have reported bone resorption around PMMA cement following implantation. Furthermore, on mixing of the PMMA cement, the exotherm associated

with polymerisation has been shown to locally increase temperature to over 100˚C and has been shown to damage bone [Hench and Wilson (1993)].

2.7.4 Calcium phosphate (CaP) ceramics

CaP ceramics have been used as implant materials for over three decades because of their potential bioactivity [LeGeros (2008), Urist et al. (1994)]. They include HA, β-TCP, biphasic calcium phosphate (BCP), amorphous calcium phosphate (ACP), calcium deficient apatite, and carbonated apatite (CA). CaP ceramics are generally bioactive, but only some of them are bioresorbable. Bioresorbability depends on composition, particle size, porosity, and preparation conditions of CaP ceramics. The rate of dissolution of CaP ceramics can be arranged in a decreasing order: β-TCP>CA>HA, which has been determined by monitoring dissolution in real-time [LeGeros (2008)].

HA is the most used CaP product in implantation because it forms an intimate bond with bone. HA has been used for alveolar ridge augmentation and the filling of bone defects [Damien and Parsons (1991)]. HA has, however, only been used for non-load bearing applications since it is brittle and failure can be catastrophic. These limitations can be compensated by combining HA with other materials such as metallic particles or polymers, or by increasing the porosity of the HA and encouraging rapid bone in growth to augment the structure [Suchanek and Yoshimura (1998), Damien and Parsons (1991)]. Porosity (100-600 μm) can be incorporated into CaPs by adding porogens, such as paraffin or naphthalene or hydrogen peroxide. The Food and Drug Administration (FDA) has approved porous HA for the treatment of bone defects caused by trauma [Damien and Parsons (1991)]. It has reported that resorption is related to porosity [Damien and Parsons (1991)].

Another dominant problem with HA is its low solubility in physiological conditions. Although HA has been used in dental applications due to the lack of resorption, HA has not been extensively used for orthopaedic applications other than to coat metallic prostheses.

TCP can exist as α-TCP and β-TCP. The rate of dissolution of TCP is greater than HA. It has been demonstrated that most TCP implants are resorbed within one month of implantation. β-TCP has been used for the repair of periodontal defects and augmentation of bone and has been formed into a cylindrical geometry for use as a drug delivery matrix [Park and Bronzino (2003), Damien and Parsons (1991)].

2.7.5 Calcium phosphate (CaP) cement

CaP cements are formed by mixing a powder phase of calcium and/or phosphate salts with an aqueous phase, which might be distilled water, phosphate buffered saline, sodium orthophosphate, orthophosphate acid or citric acid in ambient conditions. After mixing the powder and aqueous phase together, a moldable paste is formed that typically sets to form a hardened graft within a few minutes. The biggest advantages of CaP cements are that it can be easily shaped to an irregular defect and will then harden *in-situ*, making it suitable for filling bone defect as compared with the HA solid blocks or granules [Suchanek and Yoshimura (1998)], which can migrate from the implant site. In addition, CaP cements can be injected directly into fractures and bone defects [Dorozhkin (2008)].

2.7.6 Ceramic/polymer composites

Composite materials such as porous bioceramics combined with polymers such as poly (lactic acid), chitosan, and collagen have effectively replaced CaP because of their improved mechanical properties [Habraken et al. (2007), Hench and Jones (2005)].

Bonfield et al. have demonstrated that HA with polyethylene composites increased Young's modulus and reduced ductility, whilst retaining the bioactivity of HA [Bonfield (1988)]. Medical applications of the HA/polymer composites have not been as load-bearing implants, but only for bone repairs [Hench and Wilson (1993)].

2.7.7 Glasses and glass ceramics

The bioactive glasses developed for implantation are composed of SiO_2, Na_2O, CaO, and P_2O_5 (Bioglass) and Li_2O, ZnO, and SiO_2 [Park and Bronzino (2003)]. The most important characteristic of Bioglass is its rapid rate of surface reaction, which results in the rapid formation of tissue bonding [Hench and Wilson (1993)]. Ceravital, a number of different products with various compositions of glass and glass-ceramics is similar to Bioglass to the extent that it includes SiO_2, with several other components to induce crystallisation within the glass matrix [Hench and Wilson (1993), Park and Bronzino (2003)].

2.8 Surface modification of CaP based materials

The functionality of CaP based materials can be improved by introducing functional groups onto the surface of CaP crystals. The surface modification of CaP materials can promote the bonding between the matrix and bone which improves bone formation and can assist in promoting cell adhesion and the attachment of type I collagen and fibronectin. Generally, surface modification can be categorised into: a) introduction of desirable functional groups onto the surface, b) formation of functional topographies by conversion of the original surface and, c) the creation of functional topographies by removal of compositions from the original surfaces [Duan and Wang (2006)].

These modifications can be obtained through physical methods and chemical methods. The physical methods include plasma spray coating, physical vapour deposition, ion implantation, and surface machining. The chemical methods comprise the addition of functional groups, electrochemical oxidation, and acidic etching. Amongst these preparations, the chemical methods are most widely as they can be undertaken at relatively low temperatures (<100 ˚C) which is tolerable for most temperature sensitive molecules, enables the formation of crystals at micro scale and even nano scale, and the incorporation of organic or biological components [Duan and Wang (2006)]. In this section, the incorporation of functional groups on the surface of CaP materials is described.

2.8.1 Surface modification with polymers

As it has been shown that the surface hydroxyl groups of HA can react with organic isocyanate groups, polymers such as polyethylene glycol (PEG), poly (methyl methacrylate) (PMMA), poly (n-butyl methacrylate) (PBMA), and poly (hydroxyethyl methacrylate) have been used in combination with HA. The HA/polymer composites are formed by introducing coupling reagents capable of forming covalent bonds between the crystal surfaces and the polymers. The coupling reagents include isocyanateoethyl methacrylate (ICEM), hexamethylene diisocyanate (HMDI), and organosilanes have been shown to covalently bond with the hydroxyl groups of calcium phosphates [Liu et al. (1998a), Liu et al. (1998b), Santos et al. (2001)]. This combination was claimed to enhance the mechanical strength of HA. However, the lack of adhesion between the interfaces of HA and polymers often results in the failure of the composite materials [Liu et al. (1998a)].

2.8.2 Surface modification with alkyl phosphates

There are a variety of organic phosphates existing in living organisms. Therefore, some researchers have investigated the effect of the addition of organic phosphates on CaP materials. CaP materials have P-OH groups to act as a site for the attachment of a range of moieties. The synthesis of CaPs with alkyl phosphates is undertaken using the hydroxyl groups of CaP materials to bond with other functional groups by soaking the CaP particles in alkyl phosphate containing solutions. It has found that alkyl phosphate layers were formed on the HA, which cause the formation of mesopores and consequently a high specific surface area (>200m^2/g) [Tanaka et al. (1997), El-Hammari et al. (2008)]. Lebugle et al. reported that the modification of HA with (hydroxyethyl)-methacrylate phosphates and dodecanol phosphates can form a composite with polymers in dental and medical applications [Brown and Constatz (1994)].

2.8.3 Surface modification with phosphoric acids

Some workers have introduced additional OH groups on the surface of CaP materials. Amongst the reagents that contain hydroxyl groups, phosphoric acid based reactants are favoured because the P-OH groups adsorb proteins such as bovine serum albumin and lysozyme [Tanaka et al. (2004)]. The modification is performed by mixing CaPs with phosphoric acids such as pyrophosphoric acid, n-alkyl and n-fluoroalkylphosphonic acid [Tanaka et al. (2004), D'Andrea and Fadeev (2003)]. It has been confirmed that the surface properties were successfully modified because the hydrophilic surface of CaPs became hydrophobic and mechanical strength exhibited by the resulting materials was improved [Tanaka et al. (2004)].

Chapter 3 Calcium phosphates and apatites

3.1 Calcium phosphates

In addition to PO_4^{3-}, calcium phosphates can contain acidic orthophosphate anions such as HPO_4^{2-} or $H_2PO_4^-$, and/or combine with water such as $CaHPO_4 \cdot 2H_2O$. They can also be formed from different types of phosphates which include ortho (PO_4^{3-}), meta (PO_3^-), pyro ($P_2O_7^{4-}$), and poly $(PO_3)^{n-}_n$ phosphates. Pyrophosphates are potent inhibitors of nucleation and crystal growth of calcium phosphates in aqueous systems [Elliott (1994)]. Calcium phosphates can be crystallised into different phases as summarised in Table 3.1, depending on temperature, partial pressure of water, and impurities [Dorozhkin (2007), Elliott (1994)]. The lower the Ca/P molar ratio, the more acidic and water soluble the calcium phosphates are [Elliott (1994)]. The solubility isotherms of calcium phosphate phases (Figure 3.1) show the likely conditions required for synthesis. The curve of each calcium phosphate composition is the saturation boundary. The calcium phosphate compositions below the curve are supersaturated whereas those above are under-saturated. Hydroxyapatite (HA) is the least soluble calcium phosphates at a pH value of > 4.2. Therefore, at above this pH all calcium phosphates are likely to hydrolyse to HA. The points where these solubility isotherms cross are described as singular points. When two salts are immersed in the water, despite different starting compositions, the liquid composition move toward the singular point: this is the attraction effect.

The chemical formula of apatite is $Ca_5(PO_4)_3X$, where X is commonly hydroxide or a halogen (F^-, Cl^-) [Park and Bronzino (2003), Shi et al. (2004)]. However, the formula of apatite ($Ca_{10}(PO_4)_6X_2$) is often written as double as $Ca_5(PO_4)_3X$.

Table 3.1 Physical properties of various calcium phosphate salts including the formula, Ca/P ratio, density and solubility (Reproduced from Elliott et al. (1994) and Fernandez et al. (1999)).

Phase	Chemical formula	Ca/P ratio	Density (g cm^{-3})	Solubility at 25˚C, -log (K_{sp})
Monocalcium phosphate monohydrate	$Ca(H_2PO_4)_2 \cdot H_2O$	0.50	2.23	1.14
Monocalcium phosphate anhydrate	$Ca(H_2PO_4)_2$	0.50	2.23	1.14
Dicalcium phosphate dihydrate	$CaHPO_4 \cdot 2H_2O$	1.00	2.31	6.59
Dicalcium phosphate anhydrate	$CaHPO_4$	1.00	2.89	6.9
Octacalcium phosphate	$Ca_8(HPO_4)_2(PO_4)_4 \cdot 5H_2O$	1.33	2.61	96.6
α-Tricalcium phosphate	$Ca_3(PO_4)_2$	1.50	2.86	25.5
β-Tricalcium phosphate	$Ca_3(PO_4)_2$	1.50	3.07	28.9
Amorphous calcium phosphate	$Ca_xH_y(PO_4)_z \cdot nH_2O$, n=3-4.5; 15-20 % H_2O	1.20-2.20		a
Hydroxyapatite	$Ca_{10}(PO_4)_6(OH)_2$	1.67	3.16	116.8
Tetracalcium phosphate	$Ca_4P_2O_9$	2.00	3.05	38-44

a: Cannot be measured precisely. However, some values at certain pH were reported: 25.7 ± 0.1 (pH 7.4), 29.9 ± 0.1 (pH 6), 32.7 ± 0.1 (pH 5.28).

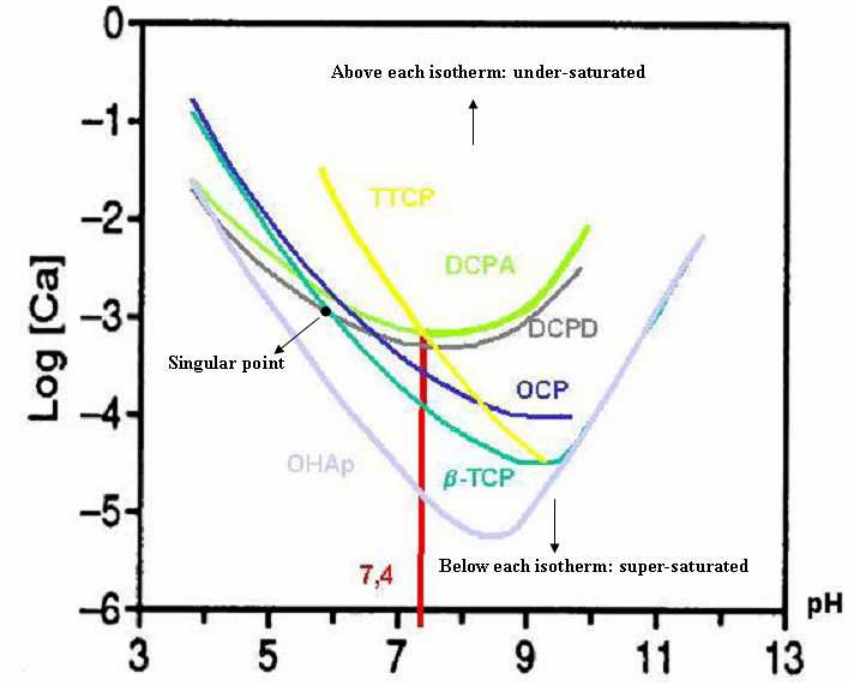

Figure 3.1 Solubility isotherm of calcium phosphate phases in the ternary system $Ca(OH)_2$-H_3PO_4-H_2O at 37 ˚C is present as the graph of Log [Ca] versus pH (reproduced from Hoffmann (2003)).

In addition, ionic substitutions of apatite readily occur, and charges of apatite balance by removing ions from other compositions. Generally, Ca^{2+} ions can be partly or completely replaced by the same charge ions, Ba^{+2}, Sr^{+2} or Pb^{2+}, or by differently charged ions, Na^{+} and K^{+}. PO_4^{3-} ions can also be replaced by ions of the same charge, AsO_4^{3-} or by differently charged ions such as CO_3^{2-}. A.G. Werner in 1786 named apatite from the Greek word “apataw”, meaning to deceive [Guelcher and Hollinger (2006)], since the apatite was initially confused with several other minerals such as aquamarine, crystollite, and fluorite [Elliott (1994)]. In 1926, the apatitic form of calcium phosphate was identified as the main mineral phase of human bone (~50-60 wt%) [Dorozhkin (2007)].

In this chapter, a brief description of the calcium phosphates is addressed, including their structural characterisation, preparation methods, and biocompatibility when implanted in hard tissue.

3.2 Monocalcium phosphates (monohydrate and anhydrate)

Monocalcium phosphate occurs as the monohydrate (MCPM) and anhydrous salt (MCPA). MCPM and MCPA are the most acidic and water solubility calcium phosphates as Table 3.1 shows [Dorozhkin (2007)].

Both MCPA and MCPM can be prepared by lowering the temperature of acidic solutions of calcium oxide and phosphorous pentoxide (P_2O_5). In addition, MCPM has been formed by adding CaO or $Ca(OH)_2$ to concentrated H_3PO_4, followed by recrystallisation, washing, and drying. After heating the recrystallised MCPM solution to 130 $^{\circ}$C, MCPA is formed [Lehr et al. (1967)].

The presence of MCPA and MCPM can be distinguished from the peaks of an XRD pattern at 7°, 23-24°, and 24-26° 2θ. In addition, the HPO_4^{2-} is present at 870 cm^{-1} in the FTIR spectrum.

Because of their high acidity, and solubility, MCPM and MCPA rarely exist in calcified tissue. Although MCPM is not biocompatible, it is used as a self-hardening component of calcium phosphate cements in medicine. MCPM crystallises in highly acid solutions. When the temperature of the precipitation conditions is above 100 $^{\circ}$C, MCPM dehydrates, and transforms to MCPA [Elliott (1994)].

3.3 Dicalcium phosphate (dihydrate-brushite and anhydrate-monetite)

Dicalcium phosphate anhydrate (DCPA) is the anhydrous form of dicalcium phosphate dihydrate (DCPD). DCPD can be precipitated by simultaneously adding aqueous solutions of Na_2HPO_4 and KH_2PO_4, and $CaCl_2$ solution at room temperature [Tovborg and Rathlev (1953)]. DCPD is also formed by neutralising dilute H_3PO_4 by the addition of calcium sucrate (calcium carbonate and sucrose) [St. Pierre PDS (1955)]. DCPD crystals are grown by the diffusion of Ca^{+2} into silica gel containing HPO_4^{2-} at pH 4 to 8 [Mooney and Aia (1961)]. It is well known that the final product of DCPD hydrolyses to HA. The hydrolysis of DCPD to octacalcium phosphate (OCP) occurs in the range pH 6.2 to 7.4 if the temperature is within 25 to 37 $^{\circ}$C, but apatites are formed when the pH or temperature increases. In fact, OCP is formed instead of HA. This is because OCP has a lower solubility than DCPD, and grows faster than HA at a pH above the singular point of DCPD (Figure 3.1).

At a temperature above 60 to 90 $^{\circ}$C in water, DCPD transforms into DCPA. When DCPD is heated at 180 $^{\circ}$C, DCPA is formed. DCPD precipitates more readily than DCPA because the rate of crystal growth of DCPA is slower than DCPD, even though thermodynamically DCPA is the more stable salt.

The method to precipitate pure DCPA is similar to that for DCPD, but at 100 $^{\circ}$C rather than room temperature [Elliott (1994)]. DCPA can also be precipitated by double decomposition of $CaCl_2$ and H_3PO_4. Like other acid phosphates, DCPA hydrolyses to HA under controlled conditions: 4 to 300 mM of $CaHPO_4$ solution were performed at CO_2

free nitrogen gas at pH in the range 6.4 to 9 with the presence of 25-100 mM $CaCl_2$ at 37 °C [Ishika and Eanes (1993)].

DCPD is found in the pathological calcifications, but DCPA is not present in any pathological calcification. Therefore, DCPD is of more biological importance than DCPA, although both are used in calcium phosphate cements in medicine [Dorozhkin (2007)].

3.4 Octacalcium phosphate

OCP is often present as a transient intermediate in the precipitation of the thermodynamically more stable HA, and biological apatites. The growth and hydrolysis of OCP has been considered as an important procedure in the mineralisation process of bone and teeth. Because OCP has a similar structure to HA, the incorporation of impurities such as carbonate, magnesium, and sodium into the crystal lattice is possible.

OCP can be prepared by the slow hydrolysis of DCPD at 40 °C. Alternatively, OCP can be formed by hydrolysis of DCPD at 80 to 85 °C in dilute nitric acid at pH 5 for 30 min. Pure OCP can be precipitated by the addition of calcium acetate to an equal volume of sodium phosphate at pH 5 and 60 °C or pH 4 and 70 to 80 °C for 3 to 4 h. However, in solution and gel systems, it has been verified that pyrophosphates inhibit the growth of OCP and result in the growth of amorphous calcium phosphates instead, but carbonate (CO_3^{2-}) or citrate favoured the formation of apatitic calcium phosphates. Depending on the availability of calcium ions, OCP hydrolyses to HA in water, which can be expressed by the following (Equation 3.1) [Elliott (1994)].

$$Ca_8H_2(PO_4)_6 5H_2O + 2Ca^{2+} \rightarrow Ca_{10}(PO_4)_6(OH)_2 + 3H_2O + 4H^+ \qquad \text{Equation 3.1}$$

OCP exhibits HPO_4^{2-} bands at 865 and 910 cm^{-1} on FTIR spectra. In addition, a ^1H resonance of HPO_4^{2-} in NMR spectrum from the apatite has been demonstrated [Elliott (1994)]. Intense peaks are presented at 26° and 32° 2θ in the XRD pattern. Although OCP has not been observed in vascular calcifications, it has been suggested as precursor phases to biological apatites of natural and prosthetic heart valves [Dorozhkin (2007)].

3.5 Tricalcium phosphates and whitlockite

Tricalcium phosphates (TCPs) may exhibit a Ca/P ratio close to 1.5, but do not exhibit a typical apatitic structure. TCPs exist in four forms: amorphous TCP, apatitic TCP, α-TCP, and β-TCP. Amorphous TCP traditionally is fromed by double decompostions between calcium and hydrogen phosphate salt solution at ambient temperature at pH around 10. Apatitic TCP is derived from crystallisation in aqueous system of amourous TCP. α- and β-TCP cannot be directly precipitated in aqueous systems, but these two forms of TCP can be obtained by sintering mixtures of calcium phosphate salts for example, DCPA and calcium carbonate. α-TCP can be formed by heating β-TCP at 1125 °C which is the transition temperature for β to α [Kokubo (Ed.) (2008), Dorozhkin (2007), Elliott (1994)].

The synthetic methods of β-TCP manufacture include the solid state process and wet chemistry [Kalita et al. (2007)]. For wet chemistry, one needs to sinter at 700 to 800 °C as the initial products are calcium deficient HA ($Ca_9(HPO_4)(PO_4)_5(OH)$) with the same Ca/P ratio of TCP as shown in Equation 3.2.

$$Ca_9(HPO_4)(PO_4)_5(OH) \rightarrow 3Ca_3(PO_4)_2 + H_2O \qquad \text{Equation 3.2}$$

Another method is to precipitate pure β-TCP and whitlockite with Ca/P or Ca/(P+Mg) ratio of 1.5 at a pH value of 11.2 and then heat to a temperature of 900 ˚C for 2 h. Although the crystal structures of β-TCP and whitlockite are similar, the crystal composition of whitlockite include magnesium (Mg^{+2}) and HPO_4^{2-} ions. In addition, β-TCP can not form at room temperature below 100 ˚C whereas whitlockite can be precipitated in ambient conditions [Elliott (1994)]. Whitlockite is a TCP derivative with magnesium, and occurs in ectopic pathological calcification. Whitlockite may form under physiological conditions, and crystallise *in vivo* in different disease states [Kokubo (Ed.) (2008)]. In addition, whitlockite can be precipitated in aqueous conditions with the presence of Mg^{+2} and HPO_4^{2-} ions [Kokubo (Ed.) (2008)].

The difference amongst apatitic TCP, α-TCP and β-TCP can be identified by XRD patterns and FTIR spectra. The characteristic of apatitc TCP is observed along with the phosphate band at 875 cm^{-1} [Kokubo (Ed.) (2008)]. The phosphorus absorption is present at 600 cm^{-1} as a single band for α-TCP, but at 550 and 616 cm^{-1} as split bands for β-TCP. For whitlockite, there is a P-OH stretching band at 850 cm^{-1} [Elliott (1994)].

3.6 Amorphous calcium phosphates

Amorphous calcium phosphates (ACPs) often exist as a transient phase during the formation of calcium phosphates in aqueous systems, particularly non-stoichiometric HA (ns-HA). ACPs can be made by the rapid addition of calcium and phosphate ions solutions, followed by washing and freeze-drying. ACPs also can be prepared with other ions in addition to Ca^{2+} and PO_4^{3-} ions [Elliott (1994)]. The presence of pyrophosphate, carbonate, and magnesium ions retards ACPs crystallisation, but the presence of fluoride ions promotes crystallisation [Dorozhkin (2007)]. The Ca/P ratio of ACPs varies from

1.18 to 1.50, depending on the pH and the concentration of mixing solutions [Dorozhkin (2007), Elliott (1994)]. The transformation of ACPs with and without water results in the formation of different products. There is no change in the Ca/P ratio of ACPs when water is absent. However, ACPs usually transform to HA or ns-HA in slightly alkaline solutions. DCPD and OCP can also be formed from ACPs. According to the solubility, an OCP-like material was an intermediate phase of the transformation of ACPs [Elliott (1994)].

The phosphate absorption of ACPs is featureless and broad in the IR spectra, which is similar to the phosphate ions in solution. However, there are some phosphate bands between 1250 and 890 cm^{-1} in FTIR spectra [Elliott (1994)]. ACPs are usually formed from spherical particles with diameter between 20 and 120 nm. According to the XRD patterns, ACPs are structurally distinct from HA. However, it is possible that ACPs have an apatitic phase, which consists of small crystals which cannot be detected by X-ray diffraction. ACP with sodium, magnesium, carbonate and pyrophosphate is found present in soft tissue pathological calcifications. In addition, pure ACPs have been used in the calcium phosphate cements as filling materials in dentistry [Dorozhkin (2007)].

3.7 Hydroxyapatite

Forster was first to present the formula of HA ($Ca_{10}(PO_4)_6(OH)_2$) [De Groot (1983)]. The Ca/P ratio of HA reflects the purity of the final material, that is whether the material contains only stoichiometric hydroxyapatite (1.67) or is mixed with other calcium phosphate phases (>1.67 or <1.67). A Ca/P ratio above 1.67 indicates the presence of calcium rich HA or carbonated HA, whereas a Ca/P ratio below 1.67 means that the apatite is calcium deficient [Hench and Wilson (1993)] or contains impurity phases. HA

has drawn significant interest as a biomaterial because of its similarity in composition to mineral component of bone [Shi et al. (2004)].

The methods to produce synthetic HA may be divided into the dry chemical reaction (solid state processing), and the wet chemical reaction. The dry chemical reaction (solid state reaction) uses high temperature treatment to enhance diffusion of ions during the chemical reaction. However, heterogeneity and agglomeration of HA is a problem with the solid state reaction since the starting elements must diffuse through the layers formed at powder interfaces to allow chemical reactions occur [Ratner et al. (2004)]. Wet chemical synthesis methods include: hydrothermal synthesis; hydrolysis; and precipitation [Ratner et al. (2004), Koutsopoulos (2002)]. These methods are used to prepare stoichiometric HA (s-HA) by using stoichiometric quantities of Ca^{2+} and PO_4^{3-} ions. By comparison, the wet chemical reaction allows the formation of HA at low temperatures because the liquid precursors are mixed at the atomic level [Kokubo et al. (2008)]. Drying processes may be divided into heating processes and non-heating processes and both affect the crystal structures of secondary particles since the powders coarsen easily. The heating processes include hot gas drying, hot-plate drying, infrared drying, spray drying and microwave drying. The non-heating processes include reduced pressure drying, freeze-drying, centrifuge drying, drying by using a desiccating agent, ultrasonic drying and critical point drying [Kokubo (Ed.) (2008)].

For stoichiometric methods, the reactants must be H_3PO_4 and $Ca(OH)_2$ or salts of calcium and phosphates with ions such as nitrates or ammonium which are unlikely to be incorporated in the apatite phase. Because of the low solubility of apatites, if the calcium and phosphate ions have exact molar values in the reaction medium, s-HA can be

obtained. For stoichiometric methods based on equilibrium syntheses, the compositions of calcium and phosphates ions must be controlled so that the solution is supersaturated with HA. The other method is to assume that s-HA is the most stable phase at a pH above the HA/DCPD singular point. Theoretically, any calcium phosphates left in solution should transform to HA with sufficient time, if the pH is maintained above the singular point. However, in reality, the product often hydrolyses to DCPA/DCPD rather than calcium deficient HA. An alternative is to hydrolyse by directly precipitating HA above the HA/DCPD singular point. For example, HA is precipitated by the addition of sufficient $Ca(OH)_2$ to saturate H_3PO_4 until the pH exceeds 9. The methods described above can also be used for the production of ns-HA [Elliott (1994)].

In the solid state reaction, mixtures of calcium and phosphate reactants are heated to over 700 $^{\circ}$C to obtain s-HA, one calcium phosphate or a mixture of calcium phosphate salts. In solid reactions, it is of utmost importance to ensure that the reaction is complete in order to produce a singular, pure phase. The reactants are usually chosen from $CaCO_3$, CaO, $Ca(OH)_2$, DCPD, DCPA, and $Ca_2P_2O_7$. The solid state reaction results in a stoichiometric and highly-crystalline HA, but high temperature treatment is necessary [Groot (1983), Suchanek and Yoshimura (1998)].

The wet chemical reaction generally leads to a more homogeneous product than the solid state reaction, and results in the formation of nano- to submicron- crystals [Liu et al. (2001), Ferraz et al. (2004)]. The wet chemical reactions occur between calcium and phosphate ions at a specific rate of addition, pH value and temperature [Liu et al. (2001), Kumar et al. (2004) and Ferraz et al. (2004)]. The purity of the HA is determined by the addition rate of a reactant and pH. If the pH during the reaction falls below pH 9 it results

in the formation of calcium-deficient HA [Jillavenkatesa and Condrate Sr. (1998)]. The main problem, however, with the wet method is the incorporation of carbonate during the preparation of HA [Suchanek and Yoshimura (1998)].

Hydrothermal processing uses water or aqueous solutions at high pressure and temperature such as 12000 psi and 275 ˚C, which results in a highly crystalline and stoichiometric product [Norton et al. (2006)]. Hydrothermal preparation has been developed using different calcium phosphate precursors such as DCPA, phosphoric acid, DCPD, calcium acetate, and triethyl phosphate. Hydrothermal processing generally results in single large crystals of HA. [Shi (2004), Suchanek and Yoshimura (1998)], but it may cause the formation of intermediate products such as β-dicalcium pyrophosphate or MCPM [Jillavenkatesa and Condrate Sr. (1998)].

Hydrolysis of TCP, DCPA, DCPD, or OCP at a temperature below 100 ˚C results in the formation of needles or blades of HA. The Ca/P ratio of the resulting HA is between 1.5 and 1.7. In the case of precipitation of HA, the temperature is lower than 100 ˚C; however, a nanometric size crystal with needles, blades, or rods of HA can be obtained. The crystallite and stoichiometry of the HA is typically lower than with other methods [Suchanek and Yoshimura (1998)]. HA can also be prepared by the sol-gel processing. The preparation and nature of sol-gel HA is described fully in the next section (Chapter 4).

The deposition of HA coatings onto prostheses can be accomplished by spontaneously nucleating and growing HA using metastable synthetic body fluids composed of an inorganic salt composition [Ferraz et al. (2004)]. Coating HA on metal alloys provides a

stable fixation between bone and implant and reduces adverse reaction [Suchanek and Yoshimura (1998)] following implantation. The thickness of HA coating is usually in the range of 200 to 400 μm. Other techniques of HA coating include plasma spraying, sputter coating, laser deposition, and sol-gel processing. Plasma spraying uses a stream of gas such as pure argon or a mixture of argon and other gases to carry HA powders, which are then passed through plasma produced using a low voltage, and high current electrical discharge. However, plasma spraying has its own problems including: binding between coatings and the substrates, and the alteration of HA structure [Yang et al. (2005)]. Like plasma spraying, sputter coating coats HA layers on the substrate, but with low pressure during sputtering. The composition of the coating may be different from the intended composition, depending on the type of sputtering system and the parameters used for deposition [Yang et al. (2005)]. Laser deposition uses an active medium to produce the optical gain under proper pumping conditions, and the optical resonator is composed of a pair of mirrors and reflects to produce optical feedback and an amplified beam [Paital et al. (2008)].

The IR spectra of HA has been summarised in Table 3.2 [Elliott (1994)]. HA is characteristic for the HPO_4^{2-} ion adsorption at 870 cm^{-1}. However, the carbonate ion absorption appears at 870 cm^{-1} because of the out-of-plane stretching. Therefore, it will interfere with the analysis of HA. In addition to PO_4^{3-} bands, the OH^- band is expected at 3600 cm^{-1}.

Pure HA never occurs in biological system, but due to the similarity to bone and teeth, HA is widely used as a coating on orthopaedic prostheses, and also with biological components for drug delivery [Dorozhkin (2007)].

Table 3.2 Positions of different vibrations of hydroxyl, phosphate, and carbonate in FTIR analysis of HA and carbonated substituted apatite (CA) gels. All values are represented as wave numbers (cm^{-1}).

Sample	PO_4^{3-} ν_3 Stretching mode	PO_4^{3-} ν_1 Stretching mode	PO_4^{3-} ν_2 Vibration mode	PO_4^{3-} ν_4 Bending mode	CO_3^{2-} ν_2 Vibration mode	CO_3^{2-} ν_3 Stretching mode	CO_3^{2-} ν_4 Bending mode	OH^- Rotary mode
HA	1029 1092	963	470	536 603	876	-	-	635 679
CHA	1023	960		561 603	875	1409 1486		

3.8 Tetracalcium phosphate (Hilgenstockite)

Tetracalcium phosphate (TTCP) is the most basic of the calcium phosphates, but its solubility in water is higher than that of HA (Table 3.1). TTCP can be formed by a solid state reaction at temperatures of 1300 °C [Elliott (1994)]. The reaction occurs in a dry environment or in a vacuum with the combination of equimolar of DCPA and calcium carbonate as the Equation 3.3 shows. If there is excess water, the reaction results in the formation of HA (Equation 3.4). This suggests that TTCP is unstable in aqueous systems, and hydrolysis of TTCP results in a mixture of HA and CaO. TTCP unlike other calcium phosphates cannot be formed from an aqueous solution [Dorozhkin (2007), Elliott (1994)].

$$2CaHPO_4 + 2CaCO_3 \rightarrow Ca_4(PO_4)_2O + 2CO_2 + H_2O \qquad \text{Equation 3.3}$$

$$3Ca_4(PO_4)_2O + H_2O \rightarrow Ca_{10}(PO_4)_6(OH)_2 + 2CaO \qquad \text{Equation 3.4}$$

In medicine, there is no product composed of only TTCP, but TTCP combined with DCPD or DCPA is used as bone cement which sets to HA in the presence of water.

3.9 Substitution of calcium phosphates

Besides the major components, Ca^{2+}, PO_4^{3-}, and OH^-, bone contains trace mineral ions, CO_3^{2-}, HPO_4^{2-}, F^-, Si^{2+}, Na^+ which play important roles in bone. Therefore, it has been hypothesised that incorporating these elements into synthetic HA can further enhance the biological response to the ceramic [Pietak et al. (2007)]. The ionic substitutions such as Mg^{2+}, Zn^{2+}, and F^- of apatites has little effect on the crystal structure since these ions are ions of like charge such as Ca^{2+} or OH^-. However, ion substitution results in the crystal lattice when CO_3^{2-} or SiO_4^{4-} takes the place of PO_4^{3-} since they have different valences [Putlyaev and Safronova (2006)]. The mineral components present in bone and s-HA are summarised in Table 3.3 [Dorozhkin (2007)]. The use of substituted apatites has been shown to exhibit favourable to bone growth when compared with non-substituted materials [Pietak et al. (2007)].

Table 3.3 Chemical composition of human bone and HA reproduced from Dorozhkin et al. 2007.

Composition	Bone (wt%)	HA (wt%)
Calcium	34.8	39.6
Phosphorus as P	15.2	18.5
Ca/P (molar ratio)	1.71	1.67
Sodium	0.9	-
Magnesium	0.72	-
Potassium	0.03	-
Carbonate as CO_3^{2-}	7.4	-
Fluoride	0.03	-
Chloride	0.13	-
Pyrophosphate as $P_2O_7^{4-}$	0.07	-
Total inorganic components	65	100
Total organic components	25	-
H_2O	10	-

3.9.1 Substitution with halides

Fluorapatite (FA) is formed by substituting the OH^- of apatite with F^-. The chemical formula of FA is $Ca_{10}(PO_4)_6F_2$. The solubility (log (K_s) =120 at 25 $^\circ$C) of FA is lowest of the apatites. The preparation of FA in solution is similar to that for HA. However, an additional amount of fluorine provided as sodium fluoride, calcium fluoride or ammonium fluoride is necessary for the formation of FA. FA readily forms a solid solution with HA to make fluorhydroxyapatite ($Ca_{10}(PO_4)_6(OH)_{2-x}F_x$, where $0<x<2$) [Dorozhkin (2007)]. FA can be precipitated by heating a stoichiometric mixture of CaF_2 and any TCP at 900 $^\circ$C or agitation of a mixture of any CaP and CaF_2 or NaF. When FA is heated in steam at 1360 $^\circ$C, it can be converted to HA [Elliott (1994)]. Pure FA hardly exists in the biological systems. However, fluoride is found in human calcified tissue [Dorozhkin (2007)]. Fluoride is also added to drinking water in order to prevent the acid dissolution of tooth mineral [LeGeros (1981)].

Chlorapatite forms by substituting OH^- with $Cl^{- -}$, and is represented by the formula $Ca_{10}(PO_4)_6Cl_2$. Chlorapatite can also be prepared either by precipitation of calcium chloride with sodium phosphate or by hydrolysis of $CaHPO_4$ in sodium chloride solution [LeGeros (1981), Elliott (1994)]. Although in the human body 70 wt% of the total ionic content is Cl^-, the average Cl^- content of enamel is only 0.25 wt%, and less than 0.01 wt% of bone and dentine, which suggests Cl^- does not readily incorporate into apatite in tissue [LeGeros (1981)].

3.9.2 Substitution of Carbonate

Carbonated apatite (CA) is closer in composition to bone and dental enamel than HA. The solubility of apatite that is substituted with carbonate is higher than stoichiometric hydroxyapatite. Furthermore, CA has been shown to have a lower thermal stability

[Elliott (1994), de Jonge et al. (2008)]. Carbonate is mainly present as three different phases in hard tissue: (a) an admixed phase either as calcite ($CaCO_3$), dolomite ((Ca, Mg) CO_3), or as a component of amorphous calcium phosphate; (b) a substituent in the apatitic structure, either substituting for hydroxyl (OH^-) or phosphate (PO_4^{-3}) or both; (c) a lattice substitution and a surface component [LeGeros (1981)]. The mode of CA can be detected by infrared and Raman spectroscopy through the presence of three equal, symmetrical C-O bonds which are present respectively at 1063 $cm^{-1}(\nu_1)$, 879 $cm^{-1}(\nu_2)$, and doubly degenerated peaks at 1514 $cm^{-1}(\nu_3)$ and 680 $cm^{-1}(\nu_4)$ (Table 3.2). Nevertheless, the ν_1 is only recognised using Raman spectroscopy, and the ν_2 is only active for the IR spectroscopy [Elliott (1994)].

CA can be classified as type A ($Ca_{10}(PO_4)_6CO_3$) or type B substituted, or type AB depending on whether the carbonate substitutes hydroxyl groups (OH^-, A type) or phosphate groups (PO_4^{3-}, B type) or both (OH^- or PO_4^{3-}, AB type). For type A, the substitution of the larger planar carbonate for the smaller linear hydroxyl group results in an expansion in the a-axis and contraction in the c-axis dimensions. If all OH groups are replaced by carbonates, an A type CHA should contain 35.3 mol% of phosphates [Nordström (1990)]. Assuming one carbonate group substitutes two hydroxyl groups, the A-type substitution mechanism can be expressed as Equation 3.5 [Norton et al. (2006)].

$$Ca_{10}(PO_4)_6(OH)_2 + CO_2 \rightarrow Ca_{10}(PO_4)_6(OH)_{2-x}(CO_3)_x H_2O \qquad \text{Equation 3.5}$$

But in the case of type B, the substitution of the smaller planar carbonate for a larger tetrahedral phosphate (PO_4^{3-}) causes a contraction in the a-axis and an expansion in the c-axis dimensions [LeGeros (1981), Elliott (1994)], suggesting that CO_3^{2-} causes a certain

modification of the structure. Assuming that sodium carbonate solution is used for the source of carbonate during precipitation, the B-type mechanism of the phosphate group replaced by the carbonate group is described by Equation 3.6 [Norton et al. (2006)].

$$Ca_{10-x}Na_x(PO_4)_{6-x}(CO_3)_x(OH)_2 \quad \text{or} \quad Na^+ + CO_3^{-2} \leftrightarrow Ca^{+2} + PO_4^{-3} \qquad \text{Equation 3.6}$$

If x=1, $Ca_{10}[(PO_4)_{6-x}(CO_3)_x](OH)_2$, B-type CHA contains 27.8 mol% phosphates [Nordström and Karlsson (1990)]. The presence of carbonate in the apatite lattice also affects the vibration modes of the phosphate groups. It was found that the concentration of carbonate is related to the loss of resolution of phosphate absorption bands [LeGeros (1981)]. The difference between these two types (A and B type) can be recognised by the infrared spectrum. LeGeros et al. showed that the substitution of carbonates for the phosphate groups and the substitution of sodium for calcium affect the size and shape of the apatite crystal. They also showed that the carbonate can be used as an effective crystal growth inhibitor because of the small size of carbonated substituted HA (CHA) [De Jonge et al. (2008)]. The shape of the crystal changes with the increasing concentration of the carbonate. Moreover, the solubility of the CHA is less than apatite without carbonate.

A-type CHA is prepared by replacing the OH in s-HA for a carbonate group at a temperature from 900 to 1000 ˚C in a CO_2 atmosphere. Nordström et al. reported that CHA was made through ion-exchange carbonate ions from solution into HA [Nordström and Karlsson (1990)]. In brief, the mechanism of A-type substitution is simple, but the reaction time is long, and also the carbon content is not easily controlled [Gibson and Bonfield (2002)].

The substitution of CO_3^{2-} for PO_4^{3-} in apatite (B-type) is made by any of the following: (1) precipitation at 60 ˚C to 100 ˚C; (2) hydrolysis of $CaHPO_4$ in a hot carbonated solution; (3) hydrolysis of $CaCO_3$ in a phosphate solution or in a solution containing carbonate and phosphate ions; (4) hydrothermal treatments or pyrolysis at 600 ˚C of carbonate containing ACPs; (5) pyrolysis at 600 ˚C of poorly crystallised calcium carbonate phosphate at 37 ˚C [LeGeros (1981)]. The B-type substitution is much more complicated than the A-type substitution for HA. Because the problem of charge balance occurs when a carbonate replaces a phosphate, there will be a loss of negative charge from the phosphate ions. This problem can be solved by using sodium or ammonium containing carbonate reagents in the precipitation which results in the incorporation of sodium or ammonium ions [Gibson and Bonfield (2002)] into the crystal lattice.

3.9.3 Substitution of Silicate

Silicon is the second most abundant element on Earth after oxygen. The content of Si in the human body varies, there being for example 100 ppm in bone and ligaments and 200-600 ppm in cartilage and other connective tissues. Since the pioneering experiments of Carlisle, silicon has been proposed to play a significant role in biomineralisation. Aqueous Si has been demonstrated to promote osteoblast proliferation, differentiation and collagen production [Pietak et al. (2007) and Carlisle (1970)].

There are several methods by which silicon substituted HA (SiHA) and silicon substituted α-TCP (Si-α-TCP) may be formed. The preparations are divided into wet chemical methods and solid state reactions [Suchanek and Yoshimura (1998)]. For wet methods, the sources of silicon are tetraethyl or propyl orthosilicate (TEOS or TPOS), silicon tetraacetate, or nano particulate silica. But it has always been difficult to make

pure SiHA without producing secondary phases such as β-TCP, silicocarnotite ($Ca_{10}(PO_4)_4(SiO_4)_2$) or α-TCP. When Si^{4+} is introduced as tetraethyl silicate or silicon tetraacetate, a lower proportion of α-TCP or Si-TCP is present. Besides those TCPs, at higher silicon concentration, silicocarnotite is frequently observed [Pietak et al. (2007)]. In the solid state, the materials are generally sintered at 700 to 1200 ˚C. However, in this case, the secondary ions, La^{3+}, SO_4^{2-} are also incorporated [Boyer et al. (1997)].

The phase compositions of SiHA and Si-α-TCP are highly dependent on the ratio of Ca/(P+Si) and Ca/P, the concentration of Si, the synthetic method and sintering temperature. Based on these parameters, different mechanisms are proposed to explain the substitutions of Si in calcium phosphates. The simple assumption is that SiO_4^{4-} substitutes for PO_4^{3-} groups. Since the substitution of SiO_4^{4-} causes loss of charge, this requires other phases of SiHA and Si-α-TCP to compensate for the deficit. There are some effects from the charge compensation, including O vacancies and excess Ca, which can each compensate for two silicons. Pietak et al. [Pietak et al. (2007)] assumed that Si-α-TCP balances its charges by creating water and oxygen vacancies resulting in the formation of an oxygen deficient Si-α-TCP. The mechanism can be described as the following (Equation 3.7).

$$6Ca_5(PO_4)_3OH + 2SiO_2 \rightarrow 10Ca_3(P_{1-x}Si_xO_{4-x/2})_2 + 3H_2O \qquad \text{Equation 3.7}$$

The other mechanism (Equation 3.8) is based on the hypothesis that Si-α-TCP is a calcium rich HA.

$$4Ca_5(PO_4)_3OH + SiO_2 \rightarrow 13/2Ca_{3+y}(P_{1-y}Si_yO_4)_2 + 2H_2O$$ Equation 3.8

Providing that OH and O compensate for the charge deficit, the formulae of SiHA and Si-α-TCP are $Ca_5(PO_4)_{3-x}(SiO_4)_xOH_{1-x}$, and $Ca_3(P_{1-x}Si_xO_{4-x/2})_2$, respectively [Pietak et al. (2007)].

Alternatively, excess H^+ in SiHA and Si-α-TCP can balance the charge deficit. However, for SiHA, OH^- vacancies can also compensate for charge imbalance as shown in Equation 3.9. In this mechanism, Gibson et al. reported that the addition of 0.4 wt% silicon resulted in x=0.16.

$$10Ca^{2+} + (6-x)PO_4^{3-} + xSiO_4^{4-} + (2-x)OH^- \rightarrow Ca_{10}(PO_4)_{6-x}(SiO_4)_x(OH)_{2-x}$$ Equation 3.9

In fact, there is usually a little carbonate precipitated during the formation of SiHA. As carbonate can replace either phosphate or hydroxyl groups, there are two hypotheses: (1) Assuming that carbonate locates in the B site of the apatite (the phosphate site), the charge balance is maintained by creating the vacancies from Ca^{2+} and OH^-: the formula is $Ca_{10-y}(PO_4)_{6-x}(CO_3)_y(SiO_4)_w(OH)_{2-x}$ where y is the molar of carbonate and part of initial silicon corresponds to y mole of carbonate, w=x-y. Therefore, there must be calcium and silicon existing as a secondary phase, which is identified as wollastonite, $CaSiO_3$. The substitution mechanism of SiHA with carbonate can be shown as Equation 3.10, but wollastonite is rarely detected since the amount and crystallinity are beyond the analytical limits.

$$(10-y)Ca^{2+} + (6-x)PO_4^{3-} + (x-y)SiO_4^{4-} + yCO_3^{2-} + (2-x)OH^- \rightarrow$$

$$Ca_{10-y}(PO_4)_{6-x}(CO_3)_y(SiO_4)_w(OH)_{2-x} + yCaSiO_3 \qquad \text{Equation 3.10}$$

The other suggested mechanism assumes that the molar number of silicate groups substituted into the apatite equates to that of the carbonate. The chemical formula is written as $Ca_{10}(PO_4)_{6-2y}(CO_3)_y(SiO_4)_y(OH)_2$ where w=y=x/2; however, only when x=0.4 (Equation 3.9). At x>0.4, there are hydroxyl vacancies because of the additional silicates (u). The resulting mechanism can be expressed as the following (Equation 3.11):

$$10Ca^{2+} + (2y+u)PO_4^{3-} + (y+u)SiO_4^{4-} + yCO_3^{2-} + uOH^- \rightarrow$$

$$Ca_{10}(PO_4)_{6-2y}(CO_3)_y(SiO_4)_{y+u}(OH)_{2-u} \qquad \text{Equation 3.11}$$

Similarly, there must be some silicon left, not incorporated into the apatites. Since there is no substitution of Ca^{2+}, it could be present as amorphous $Si(OH)_4$. The chemical formulae can be expressed as the following: (a) $Ca_{10}(PO_4)_{6-2y}(CO_3)_y(SiO_4)_y(OH)_2ySi(OH)_4$ or (b) $Ca_{10}(PO_4)_{6-2y}(CO_3)_y(SiO_4)_{y+u}(OH)_{2-u}$ + $ySi(OH)_4$. However, these secondary phases might not be detected by XRD because of the poor crystallinity and low content [Palard et al. (2008)].

Chapter 4 Sol-gel processing

4.1 Sol

A sol is a colloidal suspension of solid particles in a liquid (Figure 4.1) [Zelinski and Uhlmann (1984)]. Since the particles do not adhere to adjacent particles, each particle remains completely dispersed [Kendall (2001)]. Sols can be formed with different kinds of structure depending on the suspension, and are the simplest colloid dispersion. An aerosol, for example, is a colloidal suspension of particles in a gas (if the particles are liquid it is named fog; if the particles are solids called, it is smoke); an emulsion is a suspension of liquid droplets in another liquid [Brinker and Scherer (1990)].

4.2 Colloids

Colloids are solid particles with diameters of 1-100 nm (a suspension) [Hench and West (1990), Brinker and Scherer (1990)]. Colloids can mimic the behaviour of atoms in the dispersed: liquid, gas, and deposit a thin film with an amorphous or crystalline structure. Heller [Heller (1980)] classified four types of colloids: coacervates, tactoids, crystalloids, and flocks (Figure 4.2). Coacervates are particles that attract one another but are not bound together by van der Waals attraction or surface charges. Tactoids are particles arranged regularly, but are not bonded with one another. If tactoids are slowly dried or the repulsive barrier is gradually reduced, the particles will irreversibly bond in an ordered arrangement known as a crystalloid. However, if particles rapidly aggregate, they form disordered clusters termed flocks [Heller (1980)]. As a result of low adhesion between particles, interaction is negligible within particles which are dominated by weak forces, such as van der Waals attraction and surface charges. As coagulation of colloidal particles occurs, if the size of particles is near 0.5 μm, a colour change occurs which is visible to the naked eye [Kendall (2001)].

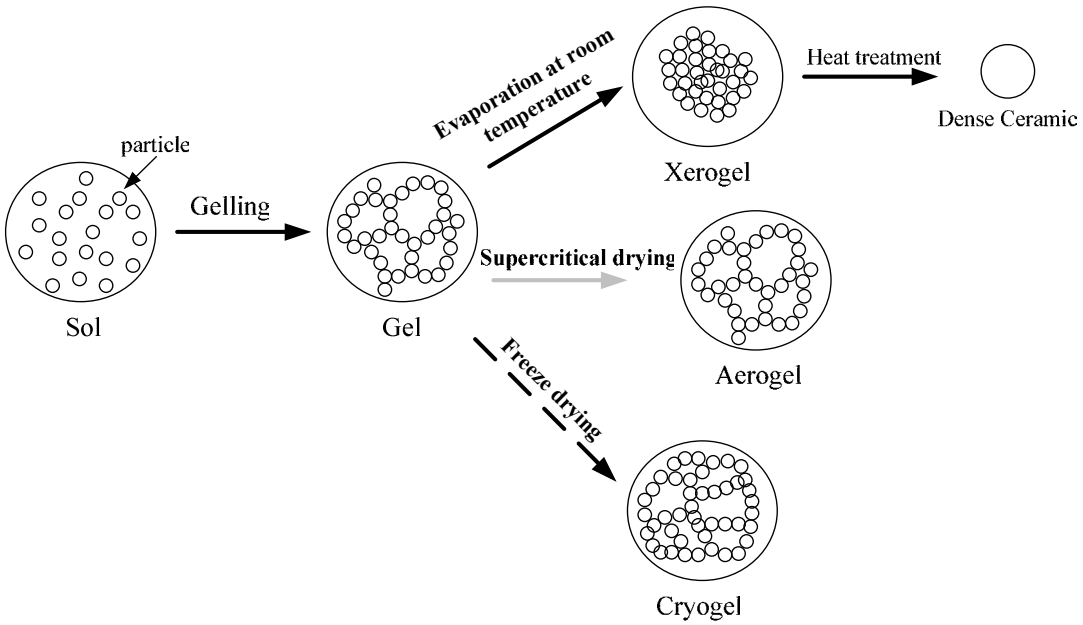

Figure 4.1 A sol is a suspension of discrete particles. When there is adhesion between particles, a gel is formed. The method of water removal from the gel leads to different structures which are termed xerogel, aerogel, and cryogel. Most gels are amorphous (non-crystalline) after drying, but become crystalline after the heat treatment.

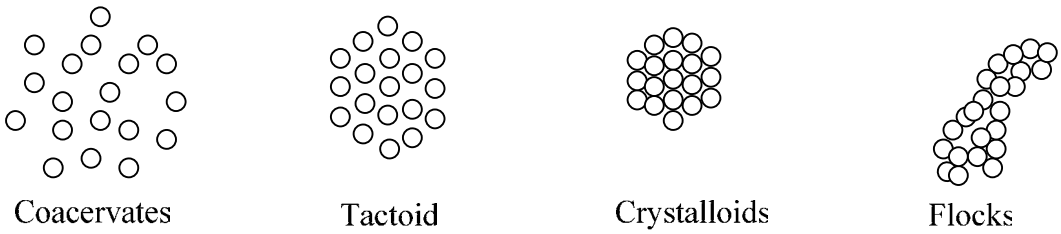

Figure 4.2 The four types of aggregated colloids (Adapted from Heller, Polymer colloids II, 1980).

4.3 Gels

A gel is an interconnected network with pores of submicrometric dimensions which are formed of condensed polymers or aggregated particles linked with one another by adhesive contact (Figure 4.1) [Hench and. West (1990), Kendall (2001), Brinker and Scherer (1990)]. A gel is a colloidal or polymeric solid containing a fluid component which has an internal network so that solid and fluid components are highly dispersed. Sols and gels are distinguished by the degree of adhesion as particles of a gel adhere strongly whereas sol particles disperse discretely [Zelinski and Uhlmann (1984), Kendall (2001)]. In diluted solution the collapse of the repulsive double layer results in the growth of a fractal aggregate, but a gel forms in a more concentrated solution [Brinker and Scherer (1990)]. The coordination (the number of adhesive points within gel particles) of a gel which can be from 2 to 12, decides its structure. For example, when the liquid is removed if the gel is strong enough it does not crack, but the gel may collapse if it is less connected [Kendall (2001), Brinker and Scherer (1990)]. In addition, the structure of a gel relies on the size and adhesive strength of particles [Brinker and Scherer (1990)]. A gel is distinguished from a paste by the deformation behaviour, and rheology, in that a gel is hard, and elastic, but a paste is somewhere between elastic and plastic [Kendall (2001)].

The strength of a gel is dependent on whether the bonds within the solid phase are permanent or reversible, which depends on the mechanism of gelation. During gelation condensed polymers or aggregated particles grow clusters, and then these clusters link together to produce a gel. The gel point is identified as the moment when the last bond is formed in the clusters. If bond formation does not stop after the gel point, however, polymers or particles continue to attach themselves, a process termed as ageing.

Ageing has been shown to be critical to the sol-gel structure. The processes of ageing after gelation are classified as polymerisation, coarsening, and phase transformation [Brinker and Scherer (1990)]. Because of continued polycondensation and reprecipitation of the gel network during ageing, the thickness of the interparticle necks increases. Therefore, the strength of the gel is increased by the ageing process [Hench and West (1990)].

In addition, shrinkage plays an important role in the structure of a gel. Shrinkage of a gel occurs as liquid is removed from the pores. Syneresis is the spontaneous shrinkage of the gel. The amount of shrinkage occurring during drying affects the strength of gel network. Drying by evaporation results in a change of capillary pressure, which brings about the shrinkage of the gel.

Sherwood divided the drying process into three stages [Hench and West (1990)]. In the first stage the reduction of volume of the gel is equal to the volume of evaporated liquid. In a large pore size (>20 nm average diameter), the first stage is a constant rate period because the evaporation rate per unit area of the drying surface is independent of time. Generally, changes of structure such as volume, weight, and density occur in the first stage. When the shrinkage stops, the first stage ends. The second stage starts when the critical point is reached. At this stage, the highest capillary pressure is created, and the gel resists further shrinkage. Consequently, cracking is likely to occur. Because of the decreased rate of evaporation, the second stage is termed the first falling rate period. In the third stage, the liquid ceases to flow to the surface, and is removed only by diffusion of its vapour. This is named the second falling rate period. The reason for cracking during the drying process is that a capillary pressure gradient is generated in the liquid phase of a

gel. The difference of pressure leads to differential shrinkage of the gel network since the exterior of the gel usually contracts faster than the interior. This causes cracking. The methods of drying influence the material structures, for example the degree of crystallinity of the gel [Hench and West (1990), Zelinski and Uhlmann (1984)].

In particulate gel, the shrinkage is controlled by the addition of electrolyte because the structure of the gel is dependent on the balance between electrostatitc repulsion, and attractive van der Waals forces [Hench and West (1990), Brinker and Scherer (1990)]. According to the drying process, the resulting gel can be xerogel, cryogel, and aerogel. Generally, most gels are amorphous, but become crystalline after heat treatment (sintering).

A gel can be categorised in various ways. Gel by Flory's definitions can be classified as being (1) lamellar gels with well-ordered lamellar structures; (2) covalent polymeric gels with covalent polymeric networks, with completely disordered structures; (3) physical polymeric gels with polymer networks formed through physical aggregation, which are also predominantly disordered; (4) particulate, or colloidal gels with particulate disordered structure (Figure 4.3) [Pierre (1997), Kendall (2001)]. Furthermore, a gel can be classified by the types of dispersed phase for instance, when the dispersed phase is water, the gel is a hydrogel (Figure 4.4) [Henisc (1970)].

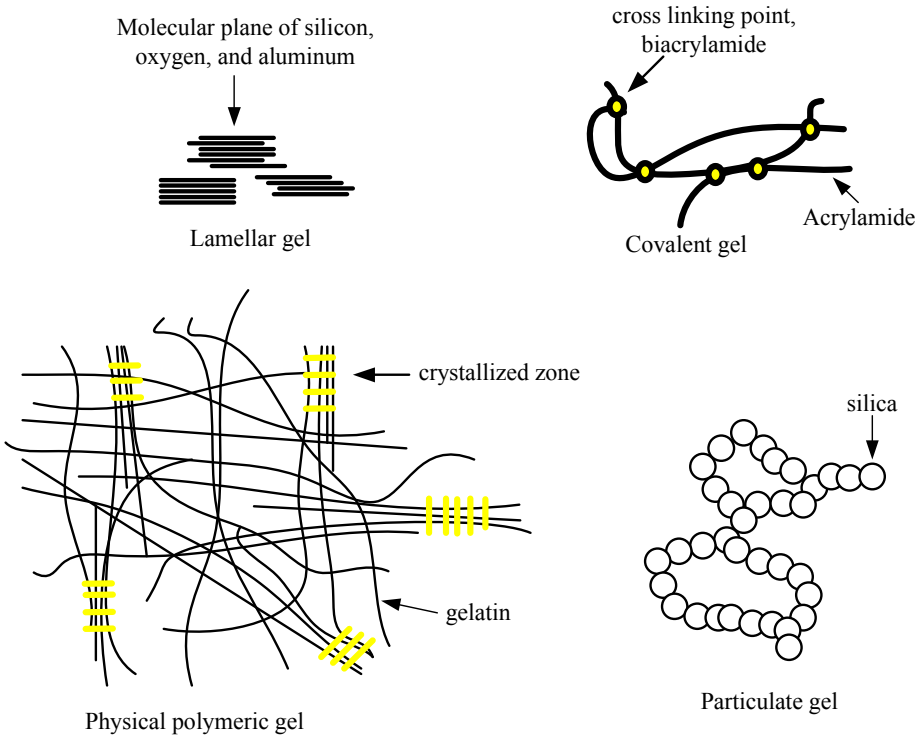

Figure 4.3 Classification of gels proposed by Flory: lamellar gel, covalent gel, polymeric gel, and particulate gel.

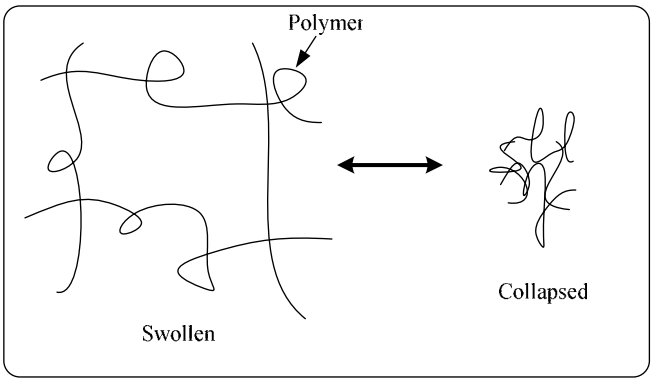

Figure 4.4 The hydrogel is swollen when the gel is in aqueous system whereas the hydrogel is collapsed when the water is removed.

There are four chemical methods to make gels which are (1) the reaction method, (2) the chemical reduction method, (3) the complex and de-complexion method, and (4) the solubility reduction method [Arora (1981)]. In the reaction method the crystals grow through a chemical reaction, for example two salt solutions are mixed together, and then the crystals precipitate as an insoluble phase [Arora (1981)]. The size of crystals of gels can be controlled by the reduction rate of crystal growth using governing the diffusion of reactive ions. The chemical reduction method, especially for the growth of metal crystals such as gold, nickel, copper, originates from the reaction method [Arora (1981)]. In the complex and de-complexion method chemical complex crystals are grown in a complex agent solution where initially the solution is homogeneously miscible, and then offers an external condition to conduct the dissociation of the formed complex. An adapted procedure for this method is to increase dilution steadily when the complex solution is diffusing through a gel [Arora (1981)]. In the solubility reduction method water soluble gels are formed where crystals are dissolved in an acid solution, and as the supersaturation of the gel medium is increased, more crystals are formed [Arora (1981)]. This method decreases the solubility of the final material by replacing gel medium with alcohol initiating the formation of crystals.

Gels can be also physically made from powders by dry compaction, smoke deposition, paste drying or phase separation followed by leaching. These physical depositions are based on a traditional method which is the plastic processing where powder mixes with a polymer solution, and is sheared strongly to break down the agglomerates. Sequentially, the powders are extruded to form samples, and the samples are heated to remove the water or organic solvent [Kendall (2001)].

4.4 Pastes

As the adhesive barrier of colloids is overcome by heating, adding salts or polymers, the coagulated colloids may form pastes. A paste is a semi-fluid material consisting of a mixture of liquid and gel which fluidises when the shear stress is high enough (Figure 4.5) [Kendall (2001)]. However, a paste can be in the form of liquid or solid, depending on the environment. The adhesion of a paste falls between a sol and a gel that is strong enough to make gelled cluster, but weak enough to move in the suspension.

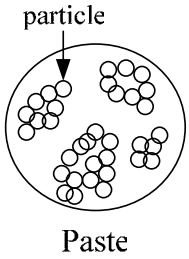

Figure 4.5 A paste is a mixture of liquid and gel characteristics with intermediate adhesion.

4.5 Sol-Gel processing in ceramics

The sol-gel process has been largely used to make bioactive glasses, and bioceramics [Hench and Jones (2005)]. The sol-gel process occurs where one or many elements are used to form a sol from which is obtained a homogeneous and amorphous gel solid by the transition from a liquid sol to a solid gel [Colomban (1989), Gupta et al. (2008)]. The resulting gel can be a dense ceramic or glass, depending on the drying process and heat treatment. These different drying conditions respectively form the gel as a xerogel, cryogel or aerogel.

A xerogel is a gel that is dried at or near ambient pressure by thermal evaporation. Therefore, the structures of xerogels are influenced by the removal of the liquid phase which can be explained by capillary forces [Vollet et al. (2004)]. The word “xerogel”

derives from the Greek xeros, meaning dry. Xerogels are generally microporous. According to IUPAC convention, micropores are smaller than 2 nm, mesopores are between 2 and 50 nm, and macropores are bigger than 50 nm [Pierre (1997)]. The surface area of xerogel ranges from 500 to 900 m^2 g^{-1}. A xerogel has less selectivity and activity in comparison with aerogels. The applications of xerogels are restricted by their mechanical properties although some studies have reported that these can be improved by surface modification [Laranjo et al. (2007), Ho et al. (2006)]. Xerogels are largely used to make dense ceramics, and are employed as catalysts, biosensors, and filters because of their high porosity and surface area [Brinker and Scherer (1990), Ho et al. (2006)].

A cryogel is a gel formed by a freeze-thawing process. The name cryogel originated from the Greek “kryos”, meaning frost or ice. A cryogel usually has pore size in the range of 5 to 100 μm, and it is a hydrophilic material [Orrego and Valencia (2009), Plieva et al. (2004)]. At present, cryogels have been largely used as a cell scaffold, to deliver immobilised molecules and as a monolithic stationary media for chromatography of cells because of their controllable porosity [Kathuria et al. (2009), Plieva et al. (2008)]. In cryogel technology, the ice crystals serve as the porogens and makes pores on melting, which controls the pore size [Kathuria et al. (2009)].

Aerogels are those prepared in an autoclave and then heated to supercritical conditions with the addition of a solvent such as water, methanol or carbon dioxide. Because an aerogel is formed in the absence of surface tension, the volume of an aerogel is almost the same as that of its precursor solution, and the density of an aerogel is as low as 0.03-0.5 g cm^{-3} [Colomban (1989)]. Aerogels comprise mostly air so they are relatively light materials with little strength, which limits their applications as biomaterials [Hench

and Wilson (1993)]. Since capillary forces are eliminated in the supercritical process, this process avoids variation of the original solid network [Vollet et al. (2004)]. Aerogels are useful for preparation of dense ceramics. In addition, the supercritical process allows the manufacture of monolithic aerogel of a volume as big as that of the autoclave. Moreover, the surface area of an aerogel ranges from 200 to 1000 m^2 g^{-1} by nitrogen adsorption measurements [Brinker and Scherer (1990)]. The advantages of aerogels are transparency, highly porosity, open cell structure, and low density. Aerogels also have the lowest thermal conductivity, refractive index, sound velocity and dielectric constant of any solids [Fricke and Tillotson (1997)].

In general, three methods are used to make sol-gel monoliths (1) gelation of a solution of colloidal powders; (2) hydrolysis, and polycondensation of alkoxide or nitrate precursors followed by supercritical drying of the gels, and (3) hydrolysis, and polycondensation of alkoxide precursors followed by ageing and drying at room temperature [Hench and West (1990)]. The preparation parameters of sol-gel processing determine the properties of the materials, including reactants, reaction temperature, the ratio of water to alkoxide, and acid or base catalyst, and the additions of drying control chemical agents [Colomban (1989)].

The advantages of sol-gel processing are high purity, homogeneity, and low temperature processing [Hench and West (1990)]. In addition, the low temperature used allows the incorporation of different kinds of inorganic, organic, and biomolecules during the formation of a gel matrix. Although sol-gel processing of inorganic ceramic and glass materials began as early as the mid-eighteenth century, applications of the sol-gel processing increased in the last two decades to include the manufacture of optical

materials, semiconductor-doped xerogels, silica for chromatography, gel matrices for hydrogen storage, and chemical sensors [Gupta and Kumar (2008)]. The first dense ceramics obtained by the sol-gel process were nuclear reactor fuels, and zirconia [Colomban (1989)].

In contrast to traditional ceramics, the ceramic sol-gels have micro and macro structures scales [Colomban (1989)]. Based on the Flory's classification, there are four types of gels [Pierre (1997)]. However, in ceramics, most ceramic gels are colloidal gels where the dense colloidal particles are linked to each other so as to make a porous three-dimensional network, and only a few are polymeric gels which have only one phase in a solution. Although Flory defined the network of the polymeric gel as having a linear polymeric nature, in fact ceramic gels do not have a well defined linear atomic structure. In addition, the particles and pores of ceramic colloidal gels are bigger than those of the polymeric gels, due to the network structure [Pierre (1997)]. Colloidal gels are made from metallic salt solutions, oxide and hydroxide sol. Polymeric gels are produced from metal alkoxides ($M(OR)_n$ where M represents of a metal for example Si, Ti, Zr, Al, B, etc. and R represents of an alkyl group through partially hydrolyzed metal alkoxides with the addition of water to form oxide networks [Zelinski and Uhlmann (1984)]. For colloidal gels, electrolytic and steric effects in the precursor solution are important for the pore structure. However, the relative rates and the extent of chemical reaction are critical for polymeric gels because the linear or weakly cross-linked structures of polymeric gels rely on the rate of hydrolysis and condensation, and the concentration of the catalyst [Pierre (1997), Zelinski and Uhlmann (1984)].

Silica gel is most commonly fabricated by sol-gel processing. Silica gels are usually composed of a solution of polysilicic or silicon alkoxide such as tetraethylorthosilicate (TEOS) or tetramethylorthosilicate (TMOS), because they can be readily hydrolysed and condensed under mild conditions [Park and Bronzino (2003)]. The silica sol-gel process traditionally includes three steps: (1) the hydrolysis of an alkoxysilane; (2) the condensation of hydrated silica to form siloxane bonding, and (3) the polycondensation by the linkage of an addition silanol group to make cyclic oligomers (Figure 4.6) [Hench and Ethridge (1982)]. However, the traditional methods of sol-gel processing include the use of low pH or high alcohol, which may destabilise biomolecules and result in the loss of bioactive function when the biomolecules are encapsulated into gel matrices [Gupta and Kumar (2008)].

The pore structures of ceramic gels are highly dependent on process parameters, such as the pH of the sol, the amount of water used for hydrolysis, the acid or base catalyst, and the type of solvent [Vollet et al. (2004)]. For example, silica aerogels catalysed by acid have smaller pores than base catalysed silica aerogels [Pierre (1997)].

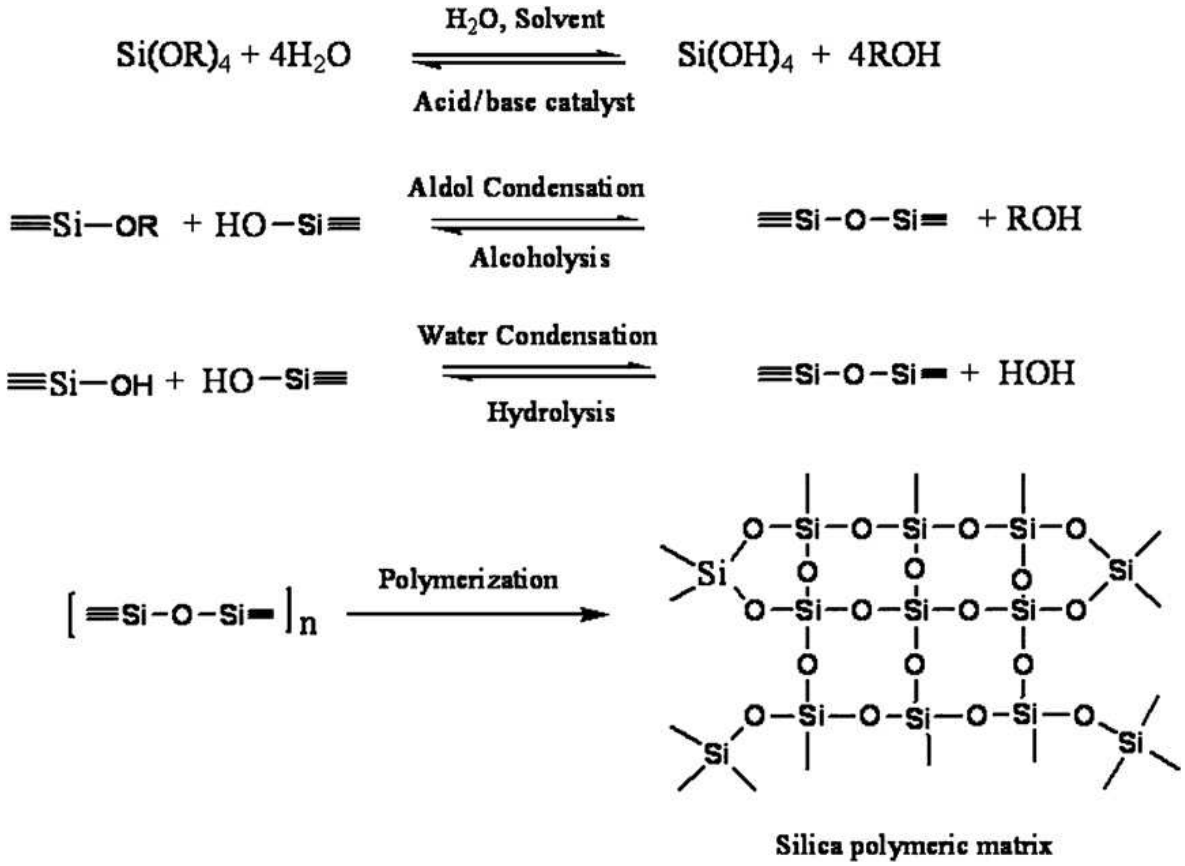

Figure 4.6 The traditional silica sol-gel process includes hydrolysis, condensation, and polycondensation. Hydrolysis results in the formation of silanol groups (Si-OH) and condensation produce siloxane bonds (Si-O-Si) with by-product such as water or alcohol. The condensation continues to occur because of the large concentration of silanol (SiOH) groups. This diagram is taken from previous work Gupta and Kumar (2008).

Chapter 5 Calcium phosphates for encapsulation

5.1 Enhancing the functionality of calcium phosphate materials

The function of calcium phosphates (CaP) used for bone replacement can be enhanced by incorporating drugs, cells, growth factors, and enzymes. The delivery of the drugs and enzymes is described next.

5.2 Encapsulation of biomolecules

It is important to maintain the activity of the biomolecules when these biomolecules are used as a medical treatment. The immobilisation methods are critical for preserving the function of the biomolecules because they provide a shell to protect the biomolecules from attack by the outer environment, and permit them to travel through the pores of the shell. The types of immobilisation are described in this section.

5.2.1 Immobilisation

Immobilisation is defined as the confinement of biomolecules (enzyme, protein) in a distinct phase that allows exchange with, but is separated from the bulk phase where substrate or inhibitor is dispersed [Trevan (1980)]. Immobilisation can be classified as adsorption, chemical covalent bonding, entrapment, and encapsulation.

Adsorption, including both physical and chemical adsorption is accomplished simply by mixing the biomolecules and support materials under mild conditions, followed by separating the unbounded molecules from the support materials by centrifugation or filtration [Bickerstaff (1987), Woodward (1985)]. The difference between physical adsorption and chemical adsorption is in the bonding [Eggins (2002)]. The bonding of physical adsorption is by van der Waals bond, hydrogen bond whereas chemical

adsorption is mediated by the covalent bond. In addition, the biomolecules are easily desorbed by varying pH, temperature, or ionic strength, due to weak bonding [Lim (1985)].

Chemical covalent bonding occurs when enzymes bind with functional groups of support materials [Chibata (1978)]. Most covalent bonds are composed of amino group, carboxyl group, hydroxyl groups, and sulphhydryl groups [Bickerstaff (1987)]. By comparison with chemical adsorption, the process in chemical covalent bonding is complicated due to the chemical reactions. In addition, the use of chemical reagents results in the reduction of the activities of biomolecules, offset by greater efficiency of delivery [Kandimalla et al. (2006)]. Entrapment is trapping biomolecules through mixing with a monomer solution and then polymerising to form a gel network in which the activity of the biomolecules may be decreased. The polymer used in the entrapment is polyacrylamide or starch gel or polypyrrole [Eggins (2002)].

Encapsulation is the incorporation of biomolecules into substrates. Encapsulation permits small molecules to permeate the structure of the materials, but it restricts the access or exit of macromolecules, proteins or enzymes [Eggins (2002)]. Unlike the other immobilisation methods, encapsulation protects the biomolecules from attack rather than providing specific sites for immobilisation [Woodward (1985)].

5.2.2 Drug delivery systems

Although CaP materials are known for their osteoconductivity, their lack of osteoinductivity necessitates the addition of osteogenic factors. In addition, the infection, resulting from trauma and surgical operation can necessitate the localised delivery of

bactericidal chemicals. CaP materials have a considerable history of being used as delivery devices, with the first being reported more than 50 years ago, and interest is still focused on the performance of therapeutic molecules encapsulated into the ceramic matrices. The release kinetics and properties of the CaP materials determines the efficacy of delivery. In this section, the kinetic mechanism of drug release is described.

The kinetics of drug release

Saltzman et al. defined controlled release as being able to engineer the release rate, release period or targeting of a specific therapeutic agent. Sustained release is maintained by mixing an active agent with excipients or binders [Saltzman (2001)]. However, burst release is unavoidable in such a delivery system, which depending on administration strategies may be regarded as negative or positive. For example, an initial burst may be the most effective way of relieving symptoms, but sustained release may result in a concentration of therapeutic molecules over the toxic level [Huang and Brazel (2001)]. Therefore, it is important to predict the kinetics of drug release, to avoid potential complications.

The kinetic mechanisms are based on either the zero order kinetics or first order kinetics. The kinetic behaviour of drug release can also be reported as physical constants [Costa and Lobo (2001)]. The zero order kinetics (Equation 5.1) can be used to describe drugs that aggregated and released slowly as in transdermal delivery or in a matrix tablet with low solubility of drugs.

$$W_0 - W_t = Kt \qquad \text{Equation 5.1}$$

Where W_0 is the initial amount of drug, W_t is the amount of drug release at time t and K is a proportional constant. Equation 5.1 can be simplified by dividing by $W_{0,}$ allowing simplification to Equation 5.2.

$$f = K_0 t \qquad \text{Equation 5.2}$$

in which f represents the fraction of drug dissolved in time t ($1-W_t/W_0$) and K_0 is the apparent dissolution rate [Costa and Lobo (2001)].

First order kinetics (Equation 5.3) has been used to describe drug dissolution or the absorption and elimination of drugs.

$$\frac{dC}{dt} = K(C_s - C) \qquad \text{Equation 5.3}$$

Where C is the concentration of the solution at time t, C_s is the solubility at the equilibrium at experience temperature, and K is the first order proportional constant [Costa and Lobo (2001)].

Empirical models have been developed for specific systems. Higuchi found that there are two models that can be used to express the release rate of incorporated drugs in which (a) the drug particles are dispersed in a homogeneous diffusion medium, and (b) the drug particles are incorporated in an essentially granular matrix and released by the penetrating solvent (Figure 5.1) [Higuchi (1963)]. The release from spherical pellets by these two models does not follow first order kinetics. Higuchi further proposed the model (Higuchi

model, Equation 5.4) assuming that a drug is loaded into a uniform solid matrix (diffusion medium) in the planar system which is based on Fick's First Law.

$$Q = \sqrt{D(2A - C_s)C_s t} \qquad \text{Equation 5.4}$$

Where Q is the amount of drug released in time t per unit exposed area, A is the drug initial concentration, C_s is the solubility of drug in the matrix and D is the diffusivity.

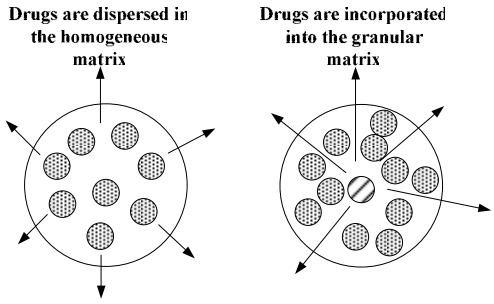

Figure 5.1 Higuchi's proposed these two models of drug release from pellets (Adapted from Higuchi 1963).

Higuchi showed that the rate of drug release is proportional to the square root of time and the rate-controlled step is the diffusion of dissolved drug through the matrix. Equation 5.4 is generally presented as the simplified formula (Equation 5.5).

$$Q = K_H t^{0.5} \qquad \text{Equation 5.5}$$

Where Q represents as the amount of drug released in time t per unit exposed area; K_H is the Higuchi dissolution constant.

Peppas's empirical model was established for the release of pharmaceutical polymeric dosages (Equation 5.6). This model is reliable only if the release occurs in a one-dimension direction with a ratio of width to length of at least 10. In addition, the release exponent varies. Peppas concluded that the release exponent, n is equal to 0.5 for a slab, following Fick's diffusion, but if the n value is between 0.5 and 1 or n=1 it does not obey Fick's diffusion. In the case of a cylinder, the release exponent n equals 0.45, following Fick's diffusion, whereas 0.89 of the release exponent is governed by the non-Fickian diffusion [Costa and Lobo (2001)].

$$f_t = \frac{M_t}{M_\infty} = at^n \qquad \text{Equation 5.6}$$

Where a is a constant of drug geometric characteristics, n is the release exponent, and f_t is the fractional release of drug and a function (M_t/M_∞) of t.

5.2.3 Enzyme storage system

Bone diseases such as hypophosphatasia result from the deficiency of tissue nonspecific alkaline phosphatase. In addition, the bioactivity of hydroxyapatite (HA) has been improved by incorporating cells, growth factors, and enzymes. In contrast to drug delivery systems, the objective of the enzyme storage system is to preserve these biomolecules inside the materials. However, encapsulation changes the catalytic behaviour of enzymes. The alteration can be determined by the affinity between enzyme and substrate. There are some kinetic mechanisms from which it is possible used to predict the catalytic behaviour of the enzyme for example, the Michaelis-Menten equation and the Lineweaver-Burk equation. The kinetic equations are detailed here.

The kinetics of enzymes

The kinetic parameters show that the relation between an enzyme and a substrate. A low Michaelis constant (K_m) indicates a strong affinity between enzyme and substrate, suggesting that only a small amount of substrate is needed whereas the high K_m indicates a weak affinity [Price and Stevens (1999)]. Michaelis firstly proposed to use mathematical analysis for enzyme kinetics [Price and Stevens (1999)]. On the assumption of one substrate reaction acted on by an enzyme, the reaction can be present as shown in Equation 5.7.

$$E+S \underset{k_{-1}}{\overset{k_1}{\rightleftharpoons}} ES$$

Equation 5.7

Here the reaction is assumed rapid and reversible between enzyme (E) and substrate (S). The forward rate constant is k_1 and reverse rate is k_{-1}. Then the enzyme complex (ES) breaks down in a slow rate of k_2 to produce product (P) as expressed by Equation 5.8.

$$ES \xrightarrow{k_2} E+P$$

Equation 5.8

As equilibrium is reached, the equilibrium constant K is defined as Equation 5.9.

$$K = \frac{[E][S]}{[ES]}$$

Equation 5.9

Micahelis, however, assumed the enzyme complex is in a steady state. The concentration of ES remains constant as the rate of ES formation equals the rate of ES breakdown which can be described as Equation 5.10.

$$k_1[E][S] = k_{-1}[ES] + k_2[ES] \qquad \text{Equation 5.10}$$

After rearrangement Equation 5.10 becomes Equation 5.11.

$$[ES] = \frac{k_1[E][S]}{k_{-1} + k_2} \qquad \text{Equation 5.11}$$

Providing the total concentration of enzyme is E_0, and substituting Equation 5.11 in the fraction of enzyme, F ($F = \frac{[ES]}{[E]+[ES]}$), then, Equation 5.11 can be expressed as the following:

$$[ES] = \frac{[E]_0[S]}{[\frac{k_{-1}+k_2}{k_1}]+[S]} \qquad \text{Equation 5.12}$$

As ν is given by $\nu = k_2[ES]$ and $V_{\max} = k_2[E]_0$, $[E]_0$ can be replaced to $\frac{V_{\max}}{k_2}$ and [ES] to $\frac{\nu}{[k_2]}$. Because of $K_m = [\frac{k_{-1}+k_2}{k_1}]$, Equation 5.12 is rewritten to the Michaelis-Menten equation (Equation 5.13).

$$\nu = \frac{V_{\max}[S]}{K_m + [S]} \qquad \text{Equation 5.13}$$

Other workers rearranged the Michaelis-Menten equation because it is difficult to decide V_{max} directly from the plot of Michaelis-Menten equation (ν against S). By rearrangement of the Michaelis-Menten equation, the kinetics can be obtained by calculating the slope of the linear graph. The Lineweaver-Burk equation (Equation 5.14) is derived from taking the reciprocals of the two sides of Equation 5.13 [Price and Stevens (1999)].

$$\frac{1}{\nu} = \frac{1}{V_m} + \frac{K_m}{V_m}\frac{1}{S} \qquad \text{Equation 5.14}$$

Where ν is the rate of product formation, V_{max} is the maximum reaction rate, K_m is Michaelis constant, and S is the concentration of substrate.

Chapter 6 Materials and Methods

Calcium phosphate gels were used in this study for the storage and release of enzymes, and drugs of therapeutic value in bone defects. In addition to standard methods that were used to characterise gels throughout, in each result chapter, there is a section to describe experimental methods, specific to each study.

6.1 Physicochemical characterisation of calcium phosphate gels

The calcium phosphate gels were routinely characterised using a range of analytical techniques, including X-ray diffraction (XRD), Fourier transform infrared spectroscopy (FTIR), dynamic vapour sorption (DVS), mercury porosimetry, helium pycnometer, laser diffraction, scanning electron microscopy (SEM), transmission electron microscopy (TEM), X-ray photoelectron spectroscopy (XRP), and X-ray fluorescence spectroscopy (XRF).

6.1.1 X-ray diffraction (XRD)

Before characterising the samples by XRD, they were ground using a pestle, and motor. Then, the sample was placed between two pieces of magic tape (3M, Berkshire, UK) on the sample holder, which was fixed in the X-ray diffractometer (D5000, Siemens-Nixdorf, Münich, Germany). XRD data were collected in the 2θ range 5-60º with a step-size of 0.02º and a step time of 0.5 s, using monochromatic CuKα radiation with a wavelength of 1.54 Å from a Ge primary beam monochromator. XRD patterns were interpreted by comparing with model patterns on the JCPD databases.

6.2 Characterisation of non-crystalline materials

Although XRD can show the crystalline structure of calcium phosphate matrices, it gives little information about compounds that are present in noncrystalline form. Analytical

equipment such as Fourier transform infrared, X-ray photoelectron spectroscopy, energy dispersive X-ray spectometry, and X-ray fluorescence spectrometers are necessary to allow characterisation of materials regardless of crystallinity. In this section, all spectrometers mentioned above are detailed.

6.2.1 Fourier transform infrared spectroscopy (FTIR)

FTIR analysis was performed using a Thermo electron corporation FTIR spectrometer. There were two methods to prepare samples in this study. Each of calcium phosphate gels was ground using a pestle and a motor. Then the specimen was placed to cover the diamond crystal cell of a smart orbit (NICOLET 380, Thermo Electron, Madison, USA) and acquired with a spatial resolution of 1.929 cm^{-1}, and 32 scans in the absorbance mode at a resolution of 4 cm^{-1} in the wavenumber range of 400-4000 cm^{-1}. The background was collected before the measurement of each specimen. The spectra were automatically corrected by the software, OMINIC 32 (Thermo Electron, Madison, USA). The other method was prepared by weighing 4 mg of powdered sample of silicon substituted calcium phosphate gels and mixing with 300 mg of potassium bromide (IR spectroscopic grade, Sigma-Adrich, Germany). The mixture was tableted into 13 mm in diameter and 100 μm in thickness using a uniaxial pressure of 30 MPa with an aluminium holder.

6.2.2 X-ray photoelectron spectroscopy (XPS)

XPS generally uses X-rays from AlKα, or MgKα which has respectively binding energies of 1200 eV, and 1486 eV. XPS can analyse to a surface depth of 1 μm to 3 nm. The results are presented as a graph of intensity (or counts per second) versus kinetic energy, E_K (or binding energy, E_B). In this study, XPS data were obtained using AlKα radiation (10kV, base pressure 1.8×10^{-8} Torr). All spectra were collected at constant pass energy of 50 eV from a sample of 13.05 mm in diameter, and 130 μm in thickness. High-resolution

spectra of the C(1s), Ca(2p), P($2p_1$), O, Si(2s) and S(2p) core levels were collected at 50 eV with calcium phosphate samples. As apatite is an insulator, the spectra were shifted to higher binding energy because of the accumulation of positive charge on the surface. The XPS spectra in this thesis were calibrated by referencing to Ca(2p) at 346.6 eV, and all peaks were shifted by a binding energy of approximately 4 to 5.

6.2.3 Energy dispersive X-ray spectroscopy (EDS)

The specimens were ground and placed on a conducting carbon tag (Agar Scientific, Essex, UK) on an aluminium stub with 20 mm diameter and 6 mm thickness (Agar Scientific, Essex, UK). As calcium phosphate gels are inherently non-conducting, the specimens cannot allow electrons generated by the incident electron beam to escape. Consequently, the quality of images was reduced due to charging of materials. This was addressed by introducing a conducting layer to diminish charging. A thin layer of carbon (Agar Scientific, Essex, UK) with 8-10 mm in thickness was deposited on each sample, requiring 3 min using a sputter coater (Polaron, TB, UK). Once the samples were sputtered with a carbon film, the image was acquired using a scanning electron microscope (FEI Philips XL30 ESEM-FEG, Oregon, USA) operated at an accelerating voltage of 10 kV, spot size between 6 and 7 and a working distance of 10 mm. The INCA system (Oxford, Bucks, UK) was used to determine the weight percentage of chemical compositions. The spectrum is shown as histograms of X-ray energy; the intensity of each peak in the histogram is increased with an increase quantity of an element being analysed

6.2.4 X-ray fluorescence spectroscopy (XRF)

The calcium, phosphorus, silicon, and sulphur content of the apatite powders in this study were determined using Rh K_α by X-ray fluorescence spectroscopy (Bruker S8 TIGER,

Coventry, U.K.). The powdered calcium phosphate gels were pelleted manually to a size of 12.8 mm diameter and 1.8 mm thickness with a die of 13 mm in diameter (Specac, Kent, England) by a hydyaulic press of 30 MPa (Graseby Specac, Kent England). Elements from beryllium (atomic number of 4) to uranium (atomic number of 92) can be analyzed. The spectrum is plotted as the fluorescent intensity versus concentration of an individual element using quantitative analysis in comparison to a standard calibration of known compositions. Generally, the fluorescence intensity corresponds positively to the concentration of elements; however, this relationship may not be linear due to the interaction of the radiation with individual elements. Fluorescence can measure samples with concentrations in the range of 0.1 to 100 %, and trace elements of per millions range [Müller (1972)].

6.3 Dynamic vapour sorption (DVS)

It is important to know the specific surface area of calcium phosphate gels as they influence the encapsulation efficiency of biomolecules. In addition, it helps us to understand the effect of different preparation methods on the calcium phosphate gels. In this work, octane was used for determination of specific surface area rather than nitrogen gas because of chemical inertness, and it allows working at ambient temperature.

6.3.1 BET analysis of specific surface area

Specific surface area can be calculated by the value of monolayer capacity, derived from a Type II isotherm, which results from the physical adsorption of gases. The monolayer capacity can be described as the amount of molecule adsorbate entirely arranging as a monolayer on the surface of 1 g of the solid. It pertains to the specific surface area of 1 g of solid and can be expressed as a simple equation (Equation 6.1).

$$A = n_m \times a_m \times L$$ Equation 6.1

where A is the specific surface area, n_m, moles of adsorbate per gram of adsorbent, a_m is the average area occupied by adsorbate in the monolayer, and L is the Avogadro constant.

Brunauer, Emmett, and Teller adapted the Langmuir equation (Equation 6.2 by simplifying assumptions to which is now known as the BET equation (Equation 6.3) [Malvern Ltd. manual. 2004].

$$\theta_1 = \frac{a_1 \kappa p}{a_1 \kappa p + z_m \nu_1 e^{-q_1 / RT}}$$ Equation 6.2

Here $\theta_1 = \frac{n}{n_m}$

Where n is moles of the adsorbed molecules on 1g of adsorbent; n_m is the monolayer capacity; p is the pressure; a_1 is the condensation coefficient; κ is a constant from kinetic theory of gases; q_1 is the isosteric heat of adsorption; z_m is the number of sites per unit area; ν_1 is the oscillation frequency of the molecule in a direction normal to the surface.

After simplifying three assumptions: Among all layers except the first layer (1) the heat of adsorption is equal to the molar heat of condensation; (2) the evaporation condenstion conditions are identical, that is $\nu_2 = \nu_3 = \ldots \nu_i$, $a_2 = a_3 = \ldots a_i$; (3) when $p = p^0$ (p^0, saturated vapour pressure), the adsorbed molecules condense to a bulk liquid on the surface of the solid, Equation 6.2 was derived to Equation 6.3 [Gregg and Sing (1982)].

$$\frac{n}{n_m} = \frac{c(p/p^0)}{(1-p/p^0)(1+\overline{c-1}p/p^0)}$$ Equation 6.3

The specific surface areas exhibited by the calcium phosphate gels were determined by applying the Brunauer Emmet Teller (BET) equation to data collected using a dynamic vapour sorption (DVS) system (Advantage II, Surface Measurement Systems, Middlesex, UK) using octane (M_w 114.23 g mol^{-1}) as the probe molecule with 64 $Å^2$ effective molecular area. The control panel for solvent was setup to open loop. The powdered specimens were loaded into the sample holder, connecting to the automatically weighing system in the microbalance module. A sample was dried out by automatically controlling the three stages in preheat method at temperature of 25 °C, and at a percentage of initial mass (dm/dt) of 0.1 %/min for each stage of 3 h. The partial pressure (PP) was then increased from 0 (start PP) to 96 (stop PP) % at 3 % increments for 30 min in time stage type, held in a stream of dry nitrogen (BOC, Birmingham, UK) at a total gas flow rate of 100 standard cubic centimetres (sccm), and post sequence of 50 sccm. The reported surface area is the average of three measurements.

6.4 Particle size characterisation

In this section, particle sizing was used to evaluate the effect of various drying regimes on the microstructure of CaP gels, and whether the surface of calcium phosphate gels were successfully modified with sulphhydryl groups. The particle size is generally measured by either image analysis, for example light microscopy, scanning electron microscopy, transmission electron microscopy or laser diffraction. In this section, relative methods of particle size measurement are outlined, including how images and data were acquired in this study.

6.4.1 Particle size measurement

The particle size of the CaP gel samples was measured by using the high performance particle sizer MS2000 (Malvern Instruments Ltd., Malvern, UK) at 25 ˚C. To maximise accuracy, it is important to consider the refractive index of the sample and the dispersed solvent into the calculation of particle size distribution that is input into standard operation procedure. The sample was prepared by dispersing 1 mg of the powdered CaP gel in 100 mL of distilled water. The refractive index of the HA was set at 1.629 [Mastersizer 2000 Malvern Ltd. (2000)]. Ultrasonic treatment (Nickel electro LTD., Somerset, England) was applied for the dispersion solution for 15 min before each measurement to avoid aggregation. 0.2 μL of suspension was transferred to a 1.6 mL disposable polystyrene cuvette (Fisher scientific, Loughborough, UK). The particle size measurement was performed in three successive steps, and each measurement lasted for 40 min.

6.4.2 Scanning electron microscopy (SEM)

SEM can image and analyse the surface of specimens by interaction between specimens and electrons. The morphology of CaP gels was observed using the SEM. The specimens were prepared using the same procedure as the EDS. However, instead of coating with carbon film, a gold film was used to analyze the image of CaP gels. A thin layer of gold with 8-10 mm in thickness was deposited on each sample, requiring for 3 min using a sputter coater (Polaron Range, SC7640). Once the samples were sputtered with a gold film, the image was acquired using a scanning electron microscope (FEI Philips XL30 ESEM-FEG, Oregon, USA) operated at accelerating voltages of 10 kV, spot size between 6 and 7 and working distance of 10 mm.

6.4.3 Transmission electron microscopy (TEM)

The size and morphology of crystals in CaP gels were evaluated using a TEM (FEI Philips TECNAI F20, FEI, The Netherlands) at accelerating voltage of 200 kV. A drop of the sample solution, prepared by dispersing the CaP gels into distilled water was placed on a 400 mesh carbon film copper grid (Agar Scientific, Essex, UK), and the liquid was allowed to evaporate.

6.4.4 Fluorescence and light microscopy

A drop of the fluorescent containing SiHA with sulphhydryl solution was placed on a glass slide (VWR International LTD., Sussex, UK). The image was taken using a fluorescent and light microscope (Carl Zeiss, Oberkochen, Germany) equipped with a 100-W mercury lamp with a LP 590 filter (Carl Zeiss, Oberkochen, Germany) as a light source, and a CCD camera (Canon PC 1049, Tapan, Japan) with 320×240 pixels processed with Powershot G5 software (Carl Zeiss, Germany). The overall magnification can be calculated by eyepieces 10×20, and objective A20PLL 400 μm (160/0.17). The reticule (Pyser-SGI limited, Kent, UK) from 1000 to 100 μm was used to evaluate the size of particles.

6.5 Porosity characterization

The strength of CaP gels is highly dependent on pore structure. Also, given that the CaP gels incorporated biomolecules, the porosity of the gels change the released rate of drugs or enzymes. Therefore, in this part, two methods and principles of porosity evaluation are detailed. One is pycnometry which was used to determine the true density of CaP gel matrices; the other measures porosity through mercury intrusion.

6.5.1 Helium pycnometry

The true density is defined as the mass of the solid divided by the volume of the solid excluding open and close pores. A gas pycnometer is commonly used to measure the true volume and density by monitoring the difference of pressure from replacement of gas by a solid. As Figure 6.1 shows, there are two chambers. A solid sample with unknown volume is placed into a sealed sample chamber with known volume$_s$. The ideal gas law, PV = nRT is applied to evaluate the unknown volume (cm^3) where P is the absolute pressure of gas (Pa), n is the number of gas molecules (moles), T is the temperature of the system (K), and R is the gas constant (8.314 J K^{-1} mol^{-1}). The initial condition can be described mathematically by Equation 6.4.

$$P_s(V_s - V_x) + P_r V_r = nRT \qquad \text{Equation 6.4}$$

where V_x is the unknown volume (cm^3), V_s is the volume of a sealed chamber, and V_r is the volume of a reference chamber. The pressure of a sample chamber is P_s (Pa), and the pressure of a reference chamber is P_r.

After the valve is opened, the condition can be described by Equation 6.5.

$$P_{sys}(V_s + V_r - V_x) = nRT \qquad \text{Equation 6.5}$$

Where P_{sys} is the pressure of the system after the valve is opened.

Following rearrangement of Equation 6.4 and Equation 6.5, they can be simplified to Equation 6.6.

$$V_x = \frac{(P_{sys}V_s + P_{sys}V_r - P_sV_s - P_rV_r)}{(P_{sys} - P_s)}$$ Equation 6.6

The accuracy of the gas pycnometer depends on the sample and analysis gas whether they are free from moisture. Helium is generally used for analysis gas because of its small atomic diameter (100 pm) [Webb (2001)].

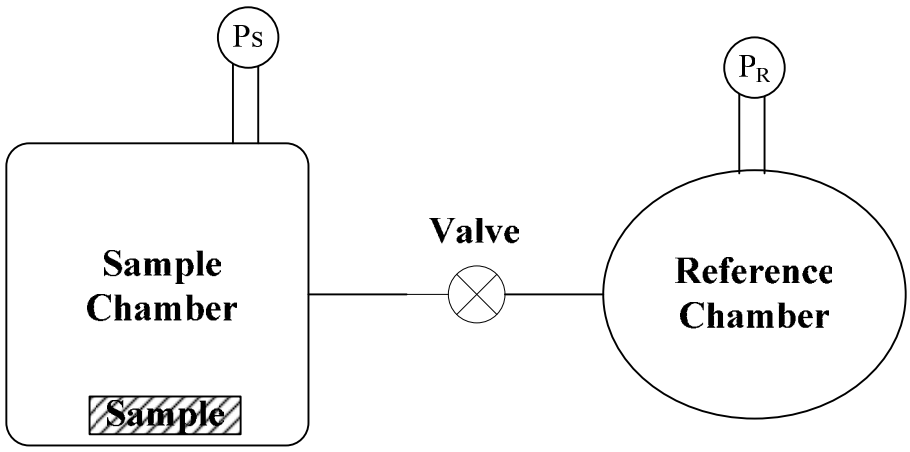

Figure 6.1 A diagram of a gas pycnometer. A sample with unknown volume is sealed in the sample chamber. The pressure of a sample chamber is measured after sealing. Then, a valve between the two chambers is opened and the pressure of the system permits to equilibrate. The volume of the unknown sample is determined by the ideal gas law, PV=nRT.

400 mg of solid samples were weighed using an electronic scale (Mettler Toledo, Switzerland). The specimen was placed into 1 cm^3 chamber of helium pycnometry ACCU-PYC II 1340 for the measurement of the density (Micromeritics, Georgia, U.S.). The purge filling pressure was at 19.5 psig at 21 °C for each cycle. The volume of the sample was determined by filling the chamber with 99.99997 % of pure helium gas (BOC, Birmingham, UK) at an equilibration rate of 0.005 psi/min. The density was the average

value of ten measurements, following ten purges, and ten cycles. Also, the average value was presented with standard deviation.

6.5.2 Relative porosity calculation

The relative density was calculated by the ratio of the apparent density (ρ_a, g cm^{-3}) to true density (ρ_t, g cm^{-3}). The apparent density was determined by measuring the mass of sample (g) divided by the volume (cm^3) as calculated from the dimensional measurement, in accordance with Equation 6.8. The relative porosity (P) is defined as follows:

$$P\% = 100 - \frac{\rho_a}{\rho_t}\% \qquad \text{Equation 6.7}$$

6.5.3 Mercury porosimetry

Mercury porosimetry is a technique developed to measure the pore size within a range of macropore. Since mercury is a non-wetting liquid with contact angle of 140°, an excess pressure is needed while liquid mercury intrudes into the pores of a solid. Washburn firstly brought the idea of using mercury intrusion to determine the pore size, and founded an equation, namely Washburn's equation (Equation 6.8) as shown in Figure 6.2.

$$r^p = -\frac{2\gamma\cos\theta}{\Delta p} \qquad \text{Equation 6.8}$$

where r^p is the radius of the pore in cylindrical shape, p^{Hg} is the pressure of mercury in the liquid phase, p^g is the pressure of mercury in the gas phase.

Equation 6.8 is a special case of the Young Laplace equation, which may be expressed as the Equation 6.9.

$$P^{Hg} - P^{g} = -\gamma(\frac{1}{r_1} + \frac{1}{r_2})$$ Equation 6.9

Since the meniscus is a segment of a sphere, $r_1 = r_2 = r^p \cos\theta$ and Δp ($p^{Hg} - p^{g} = \Delta p$) is the pressure generated from mercury intruding into a cylindrical pore of radius, r^p.

The Euqation 6.9 by replacing the above parameters is rearranged as the Washburn equation (Equation 6.8).

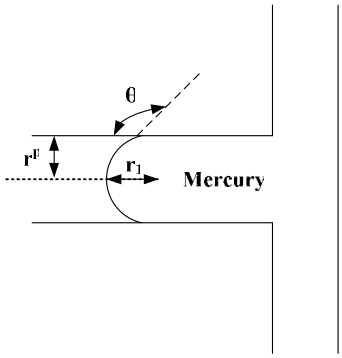

Figure 6.2 Mercury intruding into a cylindrical pore. The pore size is measured by intruding mercury into pores of solids. As the contact angle of mercury with solids is 140 ˚, an excess pressure is required to force mercury into the pores.

The mercury intrusion method is used to characterise the microporosity of CaP gels by the mercury porosimeter (AutoPore IV 9500, Micromeritics, U.S.A). The instrument measures pore from 6 nm to 360 μm in diameter in two pressurised systems: low pressure, and high pressure. The equilibration time of low pressure and high pressure is 10 s. The density of mercury at 25 °C is 13.5335 g cm^{-3} at surface tension of 485 dynes cm^{-1}. For low pressure, mercury can intrude in the pores of a material with interconnections from atmospheric pressure at 14.7 psi to 25 psi whereas for high pressure, it must be applied to penetrate through small interconnections at 30 psi to 30,000 psi. Upon different type of

penetrometers, various amounts of CaP gels between 900 mg and 400 mg were loaded into the penetrometer (920-61710-01 powder 5 mL-1.1 mL 920-61716-01 powder 3 mL-1 mL, and 920-61715-01 solid 3 mL-1 mL Micromeritics, Georgia, U.S.A). The amount of mercury used for intrusion can be examined for the total volume of pores, and bulk density. According to the bulk density, and pore volume, the skeletal density can be determined. In addition, based on the incremental intrusion (%) *versus* pore diameter curves, the distribution of pores and interconnecting pores were evaluated. Furthermore, the voids and pores in the samples can be distinguished from the graph of incremental intrusion (%) *versu*s pressure.

6.6 Surface characterization

The interaction energy of particles results from the electrical charges of surfaces on the particles. Zeta potential is usually the parameter used to characterise the charge, potential distribution across the interfacial region [Hunter (1981)].

6.6.1 Zeta potential measurement

Zeta potential measurements were performed on the Malvern instrument (Malvern, UK). The zeta potential was averaged from 10 measurements. The sample was prepared by suspending HA particles in 10 mL of distilled water and the pH of the suspension was adjusted to 7.4 by 100 mM hydrogen chloride solution.

Chapter 7 The influence of ageing on the physicochemical properties of calcium phosphate gel

7.1 Introduction

The sol-gel process has been widely used in the production of ceramic materials [Liu et al. (2001), Jillavenkatesa and Condrate Sr (1998), Hsieh et al. (2001)]. It is of interest here as it is a processing methodology that can be undertaken at room temperature. As such it can be used for the encapsulation of temperature-sensitive therapeutic molecules [Gupta and Kumar (2008)]. The physicochemical properties of gels vary, depending on parameters such as the types of precursors, pH of gel formation, and ageing processes. These variables may cause secondary phase formation, varying pore structure, and particle size.

The pore structure of calcium phosphate (CaP) matrices is most important because of its relevance to drug delivery [Teller et al. (2007)], enzyme storage [Gupta et al. (2009)], and the infiltration of bone cells [Venugopal et al. (2008)]. Generally, the sol-gel process can be divided into two steps: one is the formation of liquid sol; the other is the transformation of sol to a solid gel. Numerous studies have attempted to design porous structures from a sol. It had been shown that it is possible to increase the porosity through gel-casting using agarose [Potoczek et al. (2009)]. Some researchers have even used porogens to produce a hierarchical porous structure [Sánchez-Salcedo et al. (2008)]. In addition, Yokogawa et al. have reported that heat treatment during drying resulted in variation in particle size, and specific surface area of hydroxyapatite [Zhang and Yokogawa (2008)]. Previous work has also reported that freeze drying influences mechanical properties [Lu et al. (1998)].

In this study, various ageing regimes have been applied to process the CaP gels. The gels were each stored in different conditions for a set period of time in order to allow precipitation of secondary phases and the resulting maturation of the gel microstructure. Since it has previously been reported that adjusting conditions during the first stage of gel formation [Hench and West (1990)] has the most significant influence on microstructure, immediately following gel formation, the samples were stored at different relative humidity until no further mass change was noted. The resulting materials were characterised using XRD, XRF, EDS, helium pycnometry and mercury porosimetry.

7.2 Calcium phosphate (CaP) gel preparation

There were two different types of CaP gels used in this study, one made with and the other without carbonate ions. Barralet et al. (2002) have previously reported that the use of carbonate ions in CaP gels enables the storage of albumin for a period of 52 weeks without damage to the encapsulated proteins. Barralet et al. (2002), however, did not investigate how carbonate addition influenced the microstructure of the resulting material. Since carbonate substitution is known to have a significant influence on crystal morphology, it was anticipated that incorporating carbonate into the crystal lattice may have a significant influence on pore structure. In the present work the physicochemical properties of CaP gels made with carbonate addition, were compared with those made in the absence of carbonate. The following section details the methods used for the fabrication of the different CaP gels.

7.2.1 Hydroxyapatite (HA) preparation

To precipitate hydroxyapatite, a burette (Fisher Scientific, Loughborough, UK) was filled with 500 mL of 130 mM tri-ammonium phosphate (Rose Chemicals, London, UK). This

phosphate solution was then added at the rate of 830 μL/min to 500 mL of 210 mM calcium acetate (Sigma-Aldrich, Gillingham, UK) solution, whose pH value was adjusted to 12 by the addition of 35 % aqueous ammonia (Fisher scientific, Loughborough, UK). The resulting precipitate was washed five times with double distilled water (DDW) by a centrifuge (Jouan C422 Thermo, Madison, USA) at 4000 rpm for 10 minute. The pH of the suspension was then adjusted to pH 7.4 by the addition of 100 mM hydrochloric acid (Fisher scientific, Loughborough, UK). The suspension was filtered through Whatman No. 1 filter paper (Fisher Scientific, Loughborough) in a Büchner funnel, connected to a water aspirated vacuum pump to form a gel. A manufacturing flow diagram of the process is shown in Figure 7.1.

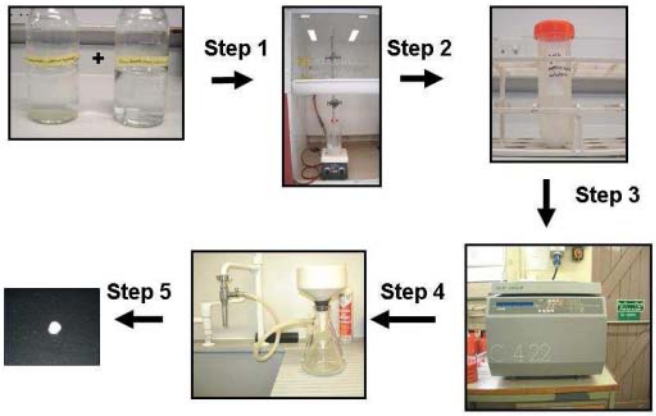

Figure 7.1 Manufacturing flow diagram for CaP gels. The tri-ammonium phosphate solution was added into the calcium acetate solution. Then, the mixture was repeatedly washed in double distilled water and centrifuged. The final suspension was filtered using the Büchner funnel, connected to a water aspirated vacuum pump.

To evaluate the influence of the ageing regime on the physicochemical properties of the precipitate the CaP was aged during the first stage of gel formation using different protocols. The ageing conditions were: 1) a relative humidity (RH) of 70 % by exposing the CaP to an ambient condition, which is open to air and the temperature is at 25 °C

(CaP xerogel); 2) an RH of 0 % by freeze drying the sample (Edwards, Sussex, England) (CaP cryogel); 3) an RH of 85 % by leaving CaP on a piece of wet cotton wool enclosed with a Büchner funnel (CaP xerogel); and 4) an RH of 100 % by storing the CaP in a sealed container above water (CaP xerogel). The details of the ageing conditions are summarised in Figure 7.2. The humidity of each condition (except 0 % RH) was quantified using a hygrometer. The time to equilibration is the sum of the time of ageing and the time of drying.

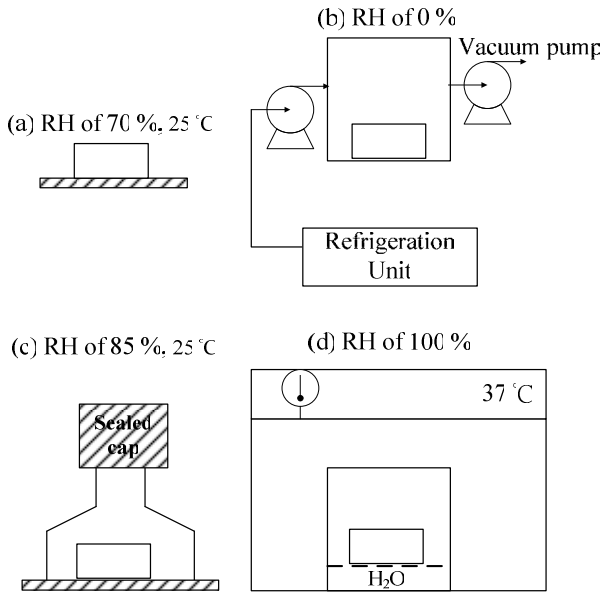

Figure 7.2 Conditions under which gels were processed during the first stage of processing. CaP gels at (a) RH of 70 %; (b) RH of 0 %; (c) RH of 85 %; (d) RH of 100 %.

7.2.2 Carbonated hydroxyapatite (CHA) preparation

The carbonate substituted hydroxyapatite (CHA) was made following the method described by Barralet et al. (2002). Briefly, 130 mM tri-ammonium orthophosphate and 320 mM sodium hydrogen carbonate (Fisher scientific, Loughborough, UK) (solution A) were poured into a 50 mL burette and dropped at 830 μL/min to 210 mM calcium acetate

(solution B), adjusted to pH 12 using 35 % aqueous ammonia. The volume ratio of solution A to solution B was 1:1. The resulting precipitate was washed five times with double distilled water by a centrifuge at 4000 rpm after which the pH of the CHA suspension was corrected to pH 7.4 using 100 mM hydrochloric acid solution. The suspension was then filtered through Whatman No. 1 filter paper in a Büchner funnel, connected to a water aspirated vacuum pump. Then, the CHA was aged using the same protocols as the HA (section 7.2.1).

7.3 Results

7.3.1 The influence of humidity on gel composition – HA

Gel crystalline component

The XRD patterns of the HA gels aged at different RH following processing all showed the presence of an apatitic phase with characteristic peaks at 26° and 32° 2θ (Figure 7.3). The relative breadth of the peaks suggested that the apatite which was formed was of low crystallinity. Except the gel aged at an RH of 0 %, crystalline impurities were formed in all samples with evidence of calcite peaks in the range 40° to 52° 2θ. At an RH of 100 %, not only calcite was present but also an impurity phase with a peak at 34° 2θ, which could have been octacalcium phosphate (OCP), which is known to form at the pH values employed in this study.

Composition regardless of crystallinity

The chemical composition was further characterised using FTIR spectroscopy. The FTIR spectra (Figure 7.4) revealed that phosphate groups of HA were present as indicated by the splitting of the ν_3 band (stretching vibrations) at 1029, and 1092cm^{-1}. In addition, the stretching vibration (ν_1 band) of the phosphate group was present at 963 cm^{-1}. The bending vibrations (ν_4) of phosphate groups were evident at 603, 563, and 470 cm^{-1}.

Changing ageing conditions did not have a significant influence on the FTIR spectra, however, there was evidence of carbonate present in the HA xerogels and HA cryogel at 872 cm^{-1}.

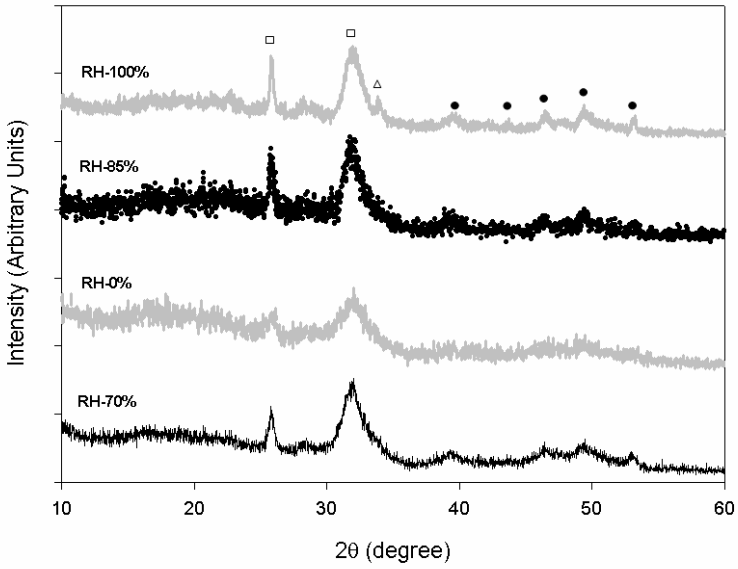

Figure 7.3 X-ray diffraction patterns of the HA gels at RHs %. The peaks of the apatite phase are labelled as (□); calcite as (●); OCP as (Δ).

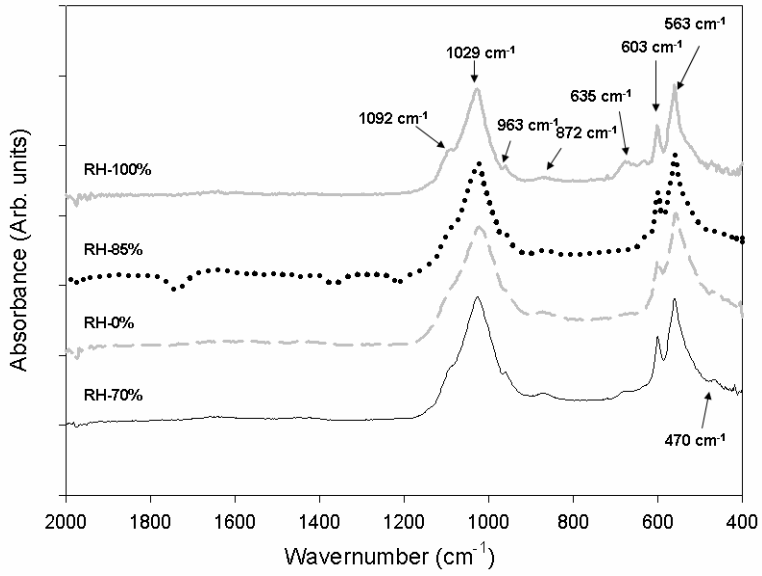

Figure 7.4 FTIR spectra of the HA gels at different RH %. The phosphate groups were present in the range 963-1092, and 470-603 cm^{-1}. Peaks indicative of CO_3^{2-} were present at 872 cm^{-1}.

To further quantify the chemical compositions of the HA gels, EDS (Table 7.1), and XRF (Table 7.2) were used to determine the Ca/P ratio of the gels. The EDS indicated, that the Ca/P ratio of the HA cryogel (1.52) and that of the HA xerogel (1.58) were less than the stoichiometric value for hydroxyapatite (1.67) but the HA xerogel at either RH of 85 % (1.99) or 100 % (1.86) by EDS was greater than might have been expected (Table 7.1). As compared with EDS, the HA cryogel (1.68) and the HA xerogel (1.65) at RH of 85 % were close to stoichiometric values (1.67) as measured by XRF (Table 7.2). Some deviation from the stoichiometric Ca/P might be expected, due to the presence of the $CaCO_3$ impurities in the samples.

Table 7.1 Elemental analysis of HA gels by the energy dispersive spectrometer (EDS) [one measurement].

Relative Humidity %	Ca weight (%)	P weight (%)	Other weight (C,O,H) (%)	Ca/P mole ratio
0	35.8	18.3	45.9	1.52
70	37.7	18.5	43.8	1.58
85	39.3	19.7	41.0	1.99
100	35.5	19.1	45.4	1.86

Table 7.2 Elemental analysis of HA gels using the X-ray fluorescence (XRF) [one measurement].

Relative Humidity %	Ca weight (%)	P weight (%)	Other weight (C,O,H) (%)	Ca/P mole ratio
0	35.0	16.0	49.0	1.68
70	31.1	15.2	53.7	1.58
85	34.7	16.3	49.0	1.65
100	43.6	17.0	39.4	1.99

7.3.2 The effect of ageing conditions on gel microstructure - HA

As the RH % was increased, the true density of HA gel generally increased from 2.50 ± 0.01 g cm^{-3} at an RH of 0 % to 2.74 ± 0.01 g cm^{-3}, except at an RH of 85 % (Table 7.3). Interestingly, the true densities exhibited by the HA gels were approximately 79 %-86 % theoretic density of HA (3.156 g cm^{-3}), suggesting the presence of a low-density amorphous calcium phosphate phase. The relationship between specific surface area and ageing conditions is shown in Figure 7.5. The higher the RH in which the sample was aged, the higher the specific surface area of HA gels, which is commensurate with the longer period of time allowed for reprecipitation to occur. At an RH of 0 %, the specific surface area was 62 $m^2 g^{-1}$. With an increase in RH from 0 to 100 %, there was almost a two fold increase in specific surface area to 109 $m^2 g^{-1}$.

Table 7.3 The effect of relative humidity on the physicochemical properties exhibited by HA gels: true density, relative porosity, and mean particle size.

Relative Humidity (%)	True Density (g cm^{-3})	Relative Porosity[a] (%)	Mean Particle Size (nm)	Time to equilibration (h)
0	2.50 ± 0.01	-	369.4 ± 11.0	24
70	2.62 ± 0.01	41 ± 5	565 .0 ± 21.9	96
85	2.57 ± 0.01	30 ± 5	585.0 ± 4.4	792
100	2.74 ± 0.01	36 ± 4	595.4 ± 91.2	768

[a]: The calculation of relative porosity is detailed in section 6.5.2.

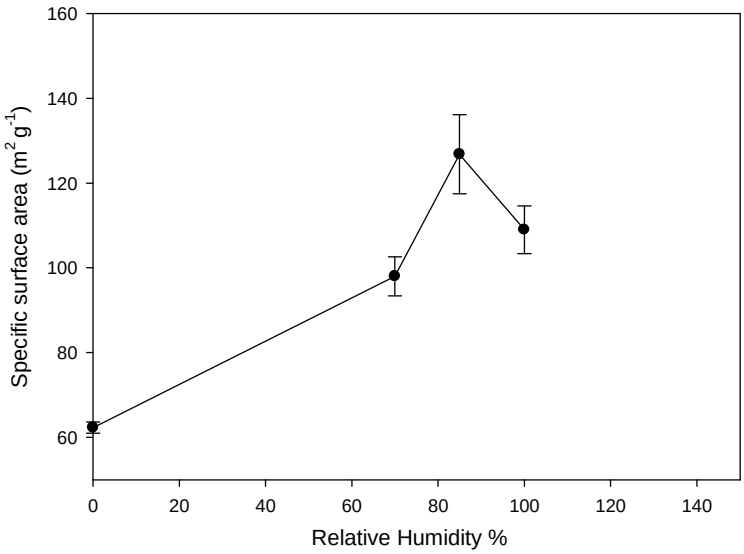

Figure 7.5 The relationship between ageing condition and the specific surface area exhibited by the HA gels. As the relative humidity of storage was increased, so was the specific surface area exhibited by the gel.

The particles of HA gels were easily aggregated. Therefore, the particle size of HA gels as determined using the particle sizer was larger than the actual crystals. An increase in RH resulted in an increase in the particle size of the sol (Table 7.3). The mean particle size of HA xerogels was from 565 to 595 nm in the range of RH % at 70 to 100 whereas the mean particle size of the HA cryogel at the RH of 0 % decreased to 369 nm. The particles were homogeneously distributed in the HA gels (mono modal distribution), other than the HA xerogel at RH of 70 % which exhibited a bimodal distribution (modal values of 50 nm and 800 nm) (Figure 7.6 (a)-(d)).

Crystal size was also determined by examining a sample using TEM. TEM images indicated that varying the ageing conditions resulted in a significant change in crystal morphology and size (Figure 7.7 (a)-(d)). In the case of the gel aged at 70 % RH, the crystals were acicular and approximately of length 70 nm and width 5 nm and distributed

evenly throughout the sample (Figure 7.7 (a)). At an RH of 0 %, the crystals comprising the gel were considerably shorter and broader than those aged at 70 % RH exhibiting approximately a length of 50 nm and a width of 20 nm (Figure 7.7 (b)). Although the HA xerogel at an RH of 85 % exhibited crystals of similar length to the HA xerogel aged at an RH of 70 %, the crystals were of a rod shape and approximately of width 10 nm (Figure 7.7 (c)). The crystals of HA xerogel at an RH of 100 % were rod shaped and about 80 nm in length and 3 nm in width (Figure 7.7 (d)). The influence of ageing conditions on the morphology of the HA crystals may provide an explanation for the large variation in specific surface area (Figure 7.5) when the samples were formed using different ageing conditions.

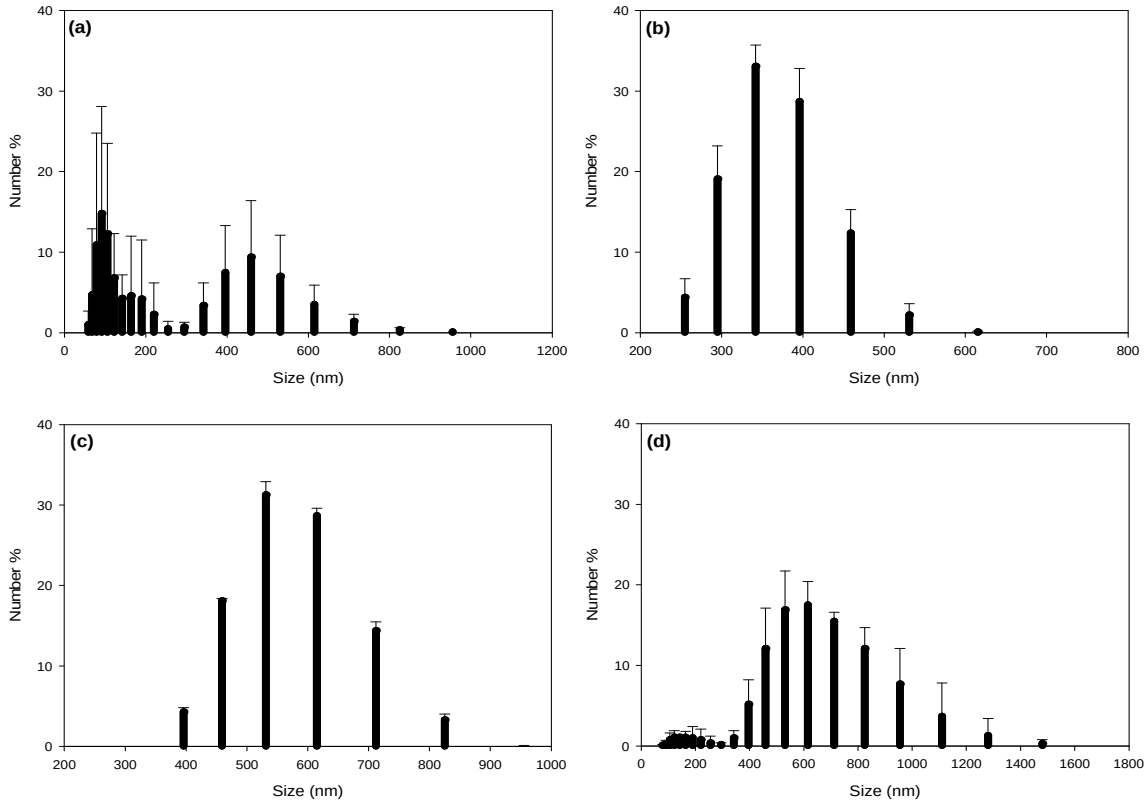

Figure 7.6 The influence of RHs on particle size distributions at (a) 70 % (HA xerogel); (b) 0 % (HA cryogel); (c) 85 % (HA xerogel); (d) 100 % (HA xerogel). The mean particle size of HA xerogel (ab. 565 nm) was larger than the size of the HA cryogels (ab. 369 nm).

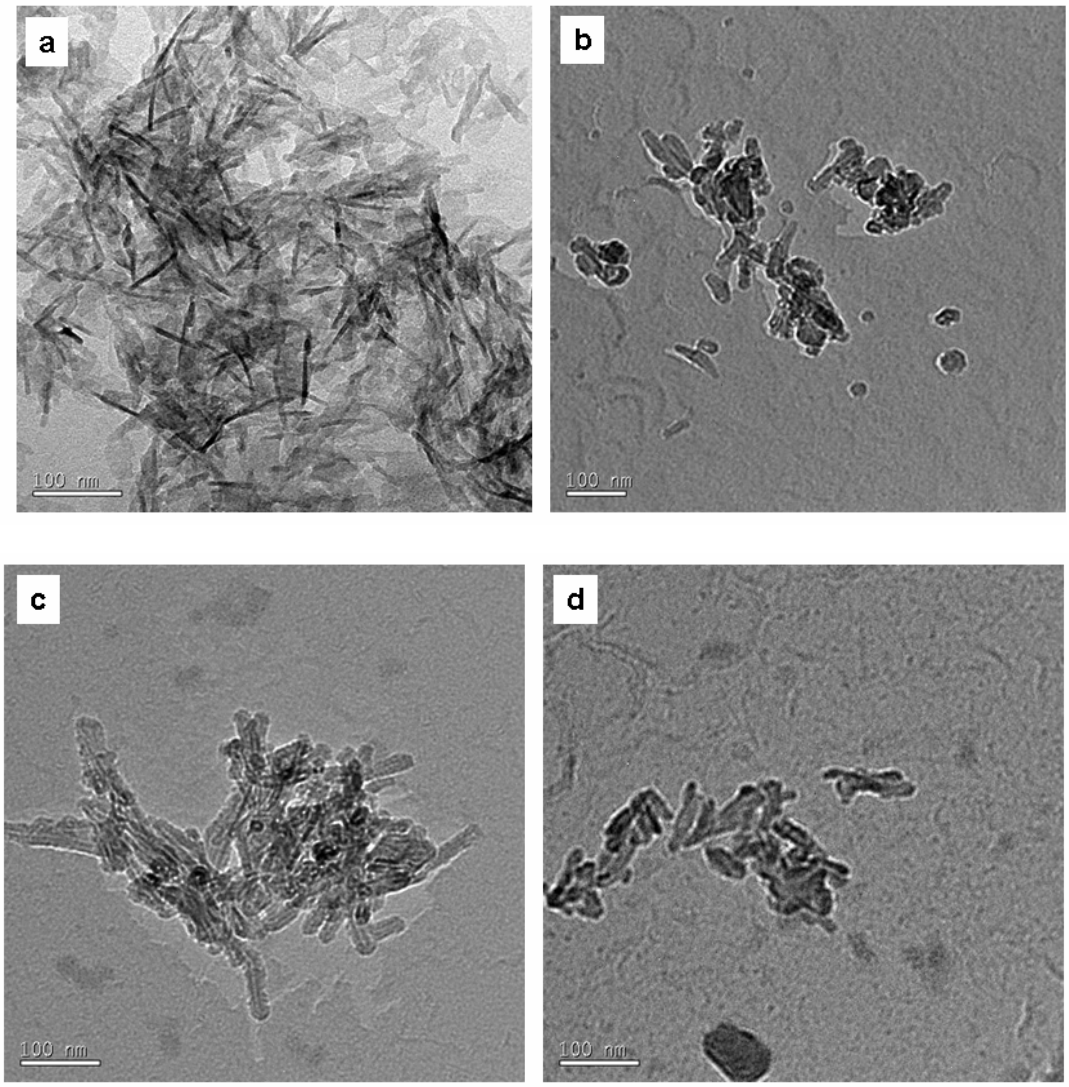

Figure 7.7 The effect of RHs on the morphologies of crystals precipitated at (a) 70 % (HA xerogel); (b) 0 % (HA cryogel); (c) 85 % (HA xerogel); (d) 100 % (HA xerogel). The crystals were in rod shape with various sizes.

7.3.3 The influence of ageing on pore structure - HA

The porosity exhibited by the HA gels was influenced by the ageing conditions that were employed and the relative porosities exhibited by the gels ranged from 30 to 41 % (Table 7.3). The variation in values, however, was well within the variability of the

measurements, as indicated by relatively high standard deviations. It is worth noting that due to excessive shrinkage in the freeze dried samples, it was impossible to accurately determine the porosity from geometrical measurements. One interesting observation was that the porosity determined from the geometrical measurements was considerably less than that measured by means of mercury porosimetry (57 to 70%; Table 7.4 (a)).

The pore size distribution as determined using mercury porosimetry showed that each of the gel samples contained a relative large proportion of pores of diameter >10 – 100 μm (Figures 7.8). In the case of the sample that was freeze dried, there was also evidence of pores of approximately 11 nm and 60 nm in diameter. When the gels were stored at 70 % RH, pores of around 11 nm in diameter were no longer apparent in the structure, although a similar population of pores of diameter around 60 nm were evident in the samples. In the samples aged at 85 % RH, the smallest pores apparent in the sample again increased in size to >100 nm. Interestingly, when aged at 100 % RH, although no pores of 60-500 nm were present, there was a population of pores of diameter 5-10 nm. The formation of these pores is further evidence for reprecipitation in the gel structure.

Table 7.4 Characterisation of pore structure of HA gels (a) total pore volume, skeletal density, and bulk density; (b) porosity, median pore diameter, and total pore area at different relative humidity % of ageing methods.

(a) Relative Humidity %	Porosity (%)	Skeletal Density (g cm $^{-3}$)	Bulk Density (g cm^{-3})
0	69.88 ± 5.60	2.48 ± 0.35	0.74 ± 0.19
70	57.59 ± 2.94	2.18 ± 0.25	0.92 ± 0.04
85	56.85 ± 3.65	2.08 ± 0.20	0.90 ± 0.16
100	63.74 ± 6.62	2.73 ± 0.45	1.01 ± 0.35
(b) Relative Humidity %	**Total Intrusion Volume (cm^3 g^{-1})**	**Median Pore Diameter (nm)**	**Total Pore Area (m^2 g^{-1})**
0	0.94 ± 0.51	32.90 ± 10.75	93.11 ± 7.54
70	0.62 ± 0.01	19.05 ± 9.26	26.39 ± 5.63
85	0.64 ± 0.16	16.41 ± 6.07	22.25 ± 20.00
100	0.69 ± 0.30	11.75 ± 0.35	123.18 ± 39.18

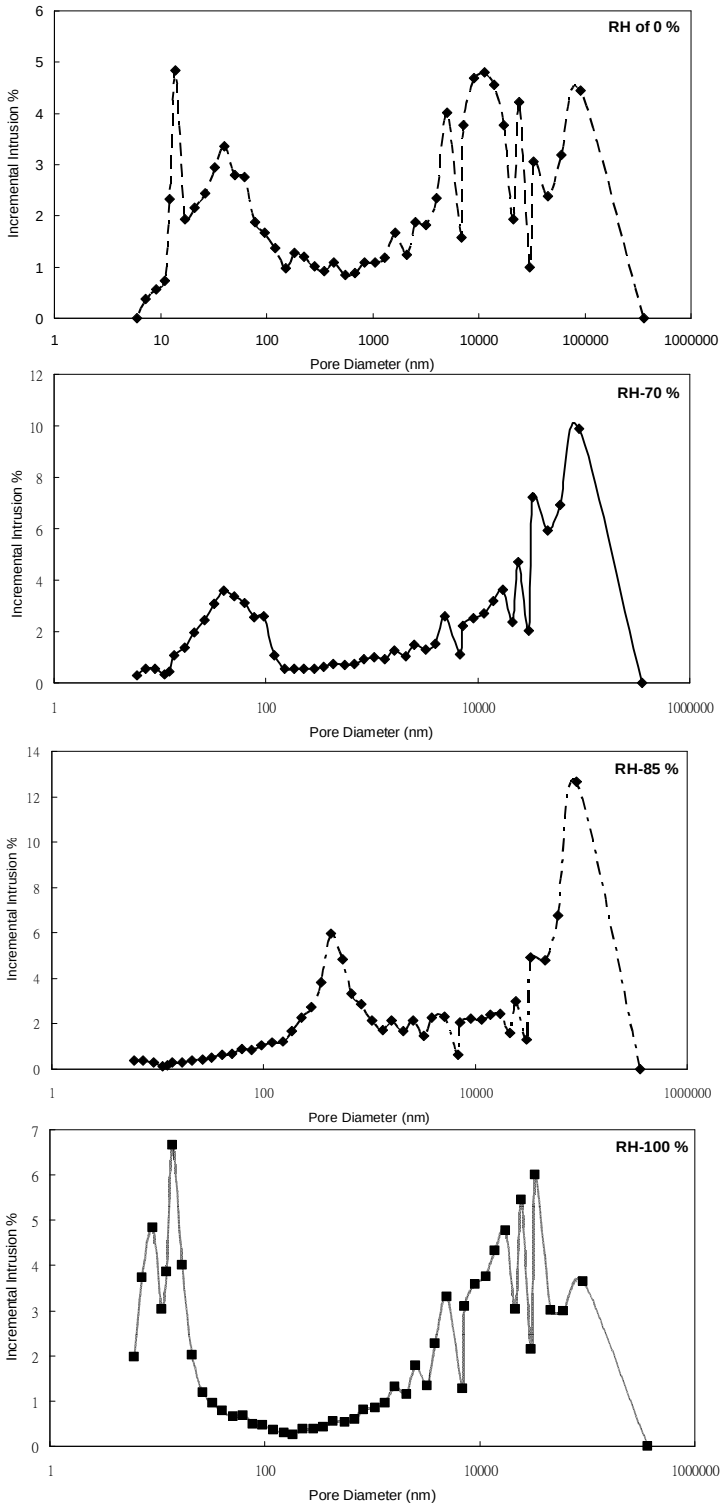

Figure 7.8 Mercury Intrusion curve of the HA gels at RH of 0 %; RH of 70 %; RH of 85 %; RH of 100 %. The larger voids were distributed from 300 to 360 μm, and the interstitial pores were in the ranged of 9 nm to 100 nm.

7.3.4 The influence of humidity on gel composition - CHA

Gel crystalline component

As might be expected, the XRD patterns collected from the samples made using solutions containing carbonate ions showed peaks indicative of a poorly crystalline apatite phase (Figure 7.9). In addition to apatitic peaks, the diffraction pattern of the CHA exhibited peaks that were indicative of the presence of calcite at 29º 2θ and 37º to 50º 2θ, as might be expected given the large excess of carbonate ions in the reaction medium. Interestingly, however, the calcite phase was not present at RHs of 0 % and 100 %. Further investigation of carbonated groups in the CHA gels was carried out through the FTIR analysis.

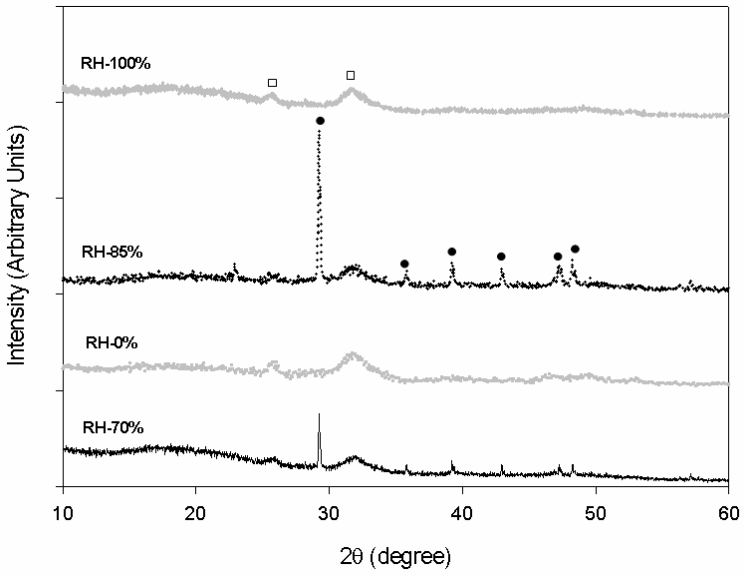

Figure 7.9 X-ray diffraction patterns of CHA gels at RH of 0, 70, 85, and 100 %. The peaks of apatite phase at 26º and 32º 2θ are labelled as square (□); calcites at 29º, and 37º to 50º 2θ as (●).

Composition regardless of crystallinity

The carbonate band of ν_2 vibrations from carbonate of the CHA was evident at 875 cm^{-1} (Figure 7.10). In addition, other distinctive peaks for carbonate could be seen at 1409 and 1486 cm^{-1}, which were indicative of the ν_3 vibrations. The phosphate (PO_4^{-3}) of the

apatites were in the ranges of 560-605 and 950-1100 cm^{-1}. The predominant phosphate peaks at 1023 cm^{-1} were due to ν_3 vibrations. A small peak at 960 cm^{-1} resulted from ν_1 vibrations of phosphate. There were also broad split phosphate peaks indicative of ν_2 vibrations and ν_4 vibrations at 561 and 603 cm^{-1} when the gels were formed at RHs of 85 and 100 %. In contrast, when the RH was either 0 or 70 %, the phosphate peak of ν_4 vibrations was diminished. These spectra of the CHA were in agreement with the XRD patterns. These spectra showed that the CHA formed was the B-type CHA since the peak at 873 cm^{-1} was not present, corresponding to an earlier study [Lee et al. (2006)]. However, there was no distinct evidence to show either the increase of carbonate groups or the decrease of phosphate groups with the humidity.

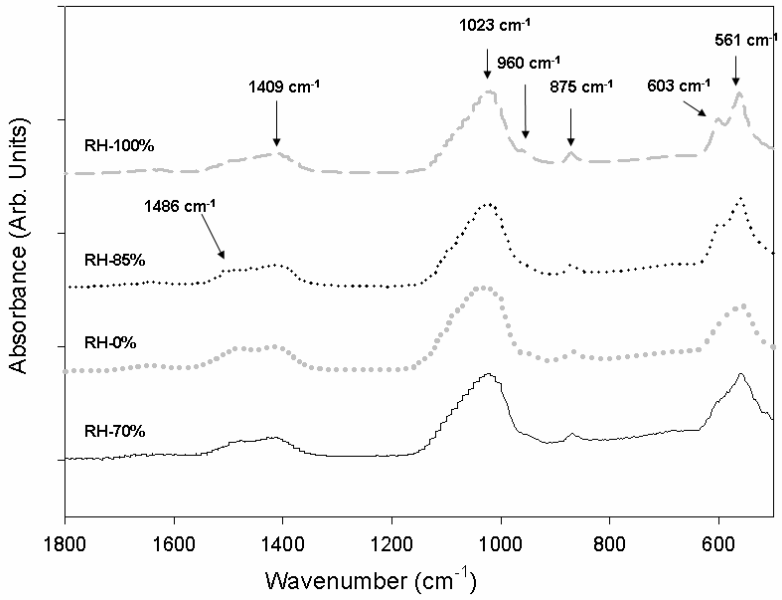

Figure 7.10 FTIR spectra of CHA gels at different RHs % of ageing regimes. The carbonate groups exhibited peaks at 875, 1409, and 1486 cm^{-1}, resulting from different vibration modes. In addition, the phosphate groups mainly present approximately at 1023 cm^{-1}, and 561 cm^{-1}. The position of carbonate groups suggested that the precipitate was a B-type substituted CHA.

EDS and XRF were used to quantify the Ca to P ratio of CHA gels after the addition of carbonate. Both results indicated that CHA gels were calcium rich HA as the Ca/P ratio is over 1.67 (Table 7.5, and Table 7.6). However, there was no positive relationship between RH % and Ca/P ratio. After heating the CHA xerogels formed at an RH of 70 % to 1300°C, the weight loss of carbonate and water was 21.7 wt% and 12.5 wt%, respectively which meant the remaining contained 65.8 % of CaPs. The entire combined amount of calcium and phosphate were between 55.4 wt% and 64.3 wt% according to the EDS, and XRF, corresponding to 65.8 %. The excessively high Ca/P ratios exhibited by the gels are suggestive of the formation of a large proportion of a calcium-rich phase, such as calcium carbonate, in the gel matrix.

Table 7.5 Elemental analysis of CHA gels by the energy dispersive spectrometer (EDS) [one measurement]. (Carbonate was neglected because of the carbonated coating)

Relative Humidity %	Ca weight (%)	P weight (%)	Other weight (C,O,H) (%)	Ca/P mole ratio
0	23.8	11.9	64.3	1.99
70	38.9	6.5	54.6	4.66
85	20.0	11.1	68.9	1.81
100	40.1	15.5	44.4	2.59

Table 7.6 Elemental analysis of CHA gels by X-ray fluorescence (XRF) [one measurement].

Relative Humidity %	Ca weight (%)	P weight (%)	Other weight (C,O,H) (%)	Ca/P mole ratio
0	44.5	10.9	44.6	3.16
70	41.4	10.7	47.9	2.99
85	36.0	15.6	48.4	1.81
100	41.2	10.3	48.5	3.08

7.3.5 The influence of humidity on gel microstructure - CHA

The true density was 74-83 % of the theoretical density of HA (3.156 g cm^{-3}). The value of the CHA cryogel was slightly different from the HA cryogels produced in this work. As Table 7.7 (a) indicates, the true density of CHA cryogel (2.35 g cm^{-3}) was lower than the HA cryogel (2.50 g cm^{-3}). The true density of the CHA xerogel at an RH of 100 % (2.43 g cm^{-3}) was also less than the true density of the HA xerogel at the same RH %. There was no difference in the true densities of the CHA xerogels at the RH of 70 % and 85 % as compared to the HA xerogels at those RHs. The true densities of the CHA xerogels at the RH of 70 % and 85 % were respectively 2.63 and 2.51 g cm^{-3} (Table 7.7 (a)).

In contrast to that of the HA gels, the specific surface area of CHA gels did not increase with an increasing in ageing period. The specific surface area of CHA xerogels at RH of 70 % and 85 % was 42 and 43 m^2 g^{-1}, respectively which was considerably smaller than the HA xerogels at the same RH (98-126 m^2 g^{-1}) (Figure 7.5). However, the CHA xerogel at RH of 100 % (276.9 m^2 g^{-1}) was twice as much as the HA xerogel at RH of 100 % (109 m^2 g^{-1}). As the specific surface areas of the CHA gels were decreased, the particle sizes

were increased. On the other hand, the particle size of CHA xerogels at RH of 100 % decreased while its specific surface area was raised (Table 7.7 (b)).

Table 7.7 The effect of carbonate on the physicochemical characterisation of HA gels: (a) true density, and relative porosity; (b) specific surface area, and mean particle size.

(a) Relative Humidity (%)	True Density (g cm^{-3})	Relative Porosity %	Time to equilibration (h)
0	2.35 ± 0.01	-	24
70	2.63 ± 0.01	47 ± 4	96
85	2.51 ± 0.01	30 ± 6	192
100	2.43 ± 0.01	50 ± 11	1008

(b) Relative Humidity (%)	Mean Particle Size (nm)	Specific surface area (m^2g^{-1})	Time to equilibration (h)
0	536.3 ± 124.4	48.3 ± 4.6	24
70	961.0 ± 7.0	42.3 ± 1.6	96
85	669.1 ± 18.6	43.1 ± 9.7	192
100	312.1 ± 98.7	276.9 ± 33.7	1008

The mean particle size of the CHA gels was larger than the HA gels (Table 7.3 and Table 7.7 (b)). The mean particle size of the CHA xerogel at an RH of 70 % was 961 nm where 42.1 % of particles were dispersed between 712 and 955 nm (Figure 7.11 (a)). As an RH was increased to 85 %, 53.5 % of particles were dispersed in the range of 400 nm to 900 nm (Figure 7.11 (c)), and the mean particle size of the HA xerogel at RH of 85 % was reduced to 669 nm. When the RH was 100 %, the particle size of the CHA xerogel with mean size of 312 nm was largely distributed (97 %) between 200 and 400 nm as Figure 7.11 (d) shows. However, the particles of CHA cryogels with mean size of 536 nm were

bimodal distribution in which 17.7 % of particles distributed around 459 nm, and 12.3 % around 122 nm (Figure 7.11 (b)).

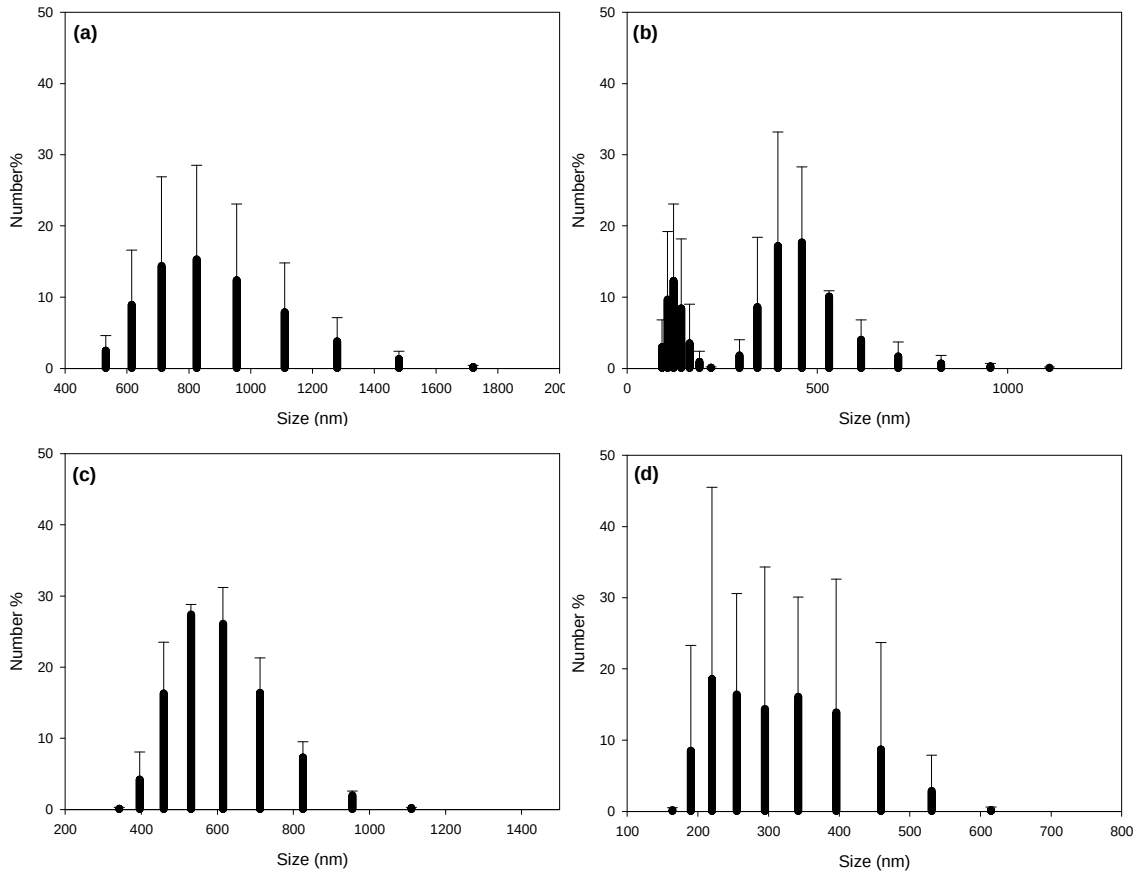

Figure 7.11 The effect of carbonate substitution on the particle size distribution of HA gels (CHA) at RH of (a) 70 %; (b) 0 %; (c) 85 %; (d) 100 %.

Figure 7.12 shows that the crystals of the CHA gels were in various rod shapes with a small size approximately from 14 nm in length and 50 Å in thickness to a large size from 50 nm in length and 42 nm in thickness. In comparison with HA gels, as expected, the addition of the carbonate resulted in a distinct reduction of the crystal size. The CHA xerogel at an RH of 70 % was around 50 nm in length and 10 nm in thickness (Figure 7.12 (a)). As the RH was increased to 85 %, the sizes of crystals were approximately

from 20 to 50 nm in length and 1 to 3 nm in thickness as the Figure 7.12 (c). When RH was 100 %, the crystals of the CHA xerogels were grown to four times in thickness as much as the CHA xerogels at RH of 70 % (Figure 7.12 (d)). After reducing to RH of 0 %, the CHA cryogel exhibited rod-like crystals of around 70 nm in length and 1 nm in thickness (Figure 12 (b)).

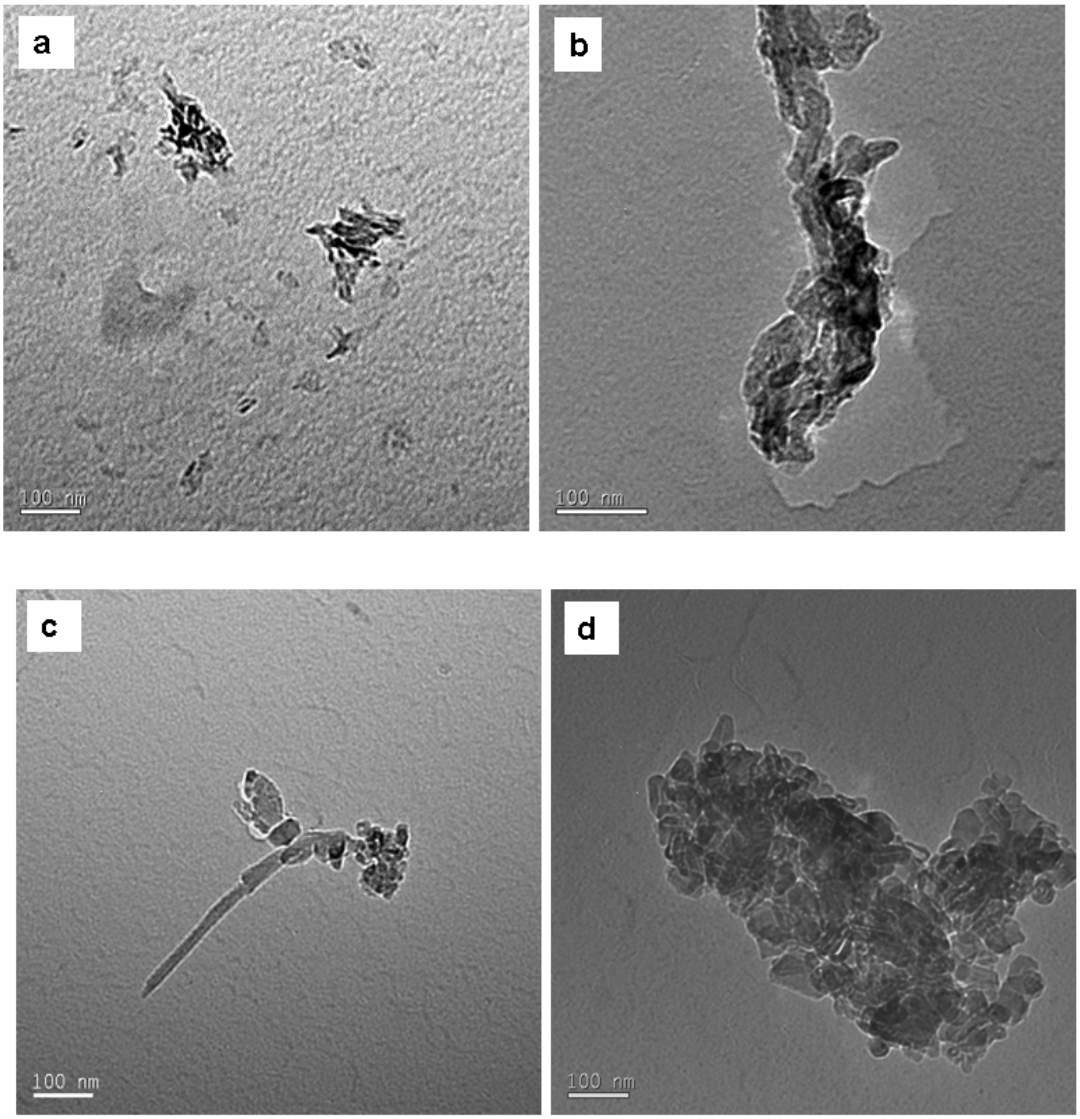

Figure 7.12 TEM micrographs of carbonate substituted HA gels (CHA gels) at RH of (a) 70 %; (b) 0 %; (c) 85 %; (d) 100 %.

7.3.6 The effect of carbonate on the porosity-CHA

The relative porosity of the CHA xerogels varied from 30 to 50 %, which was a slight increase when compared with that of the HA gels (30 to 41 %).The relative porosity of the CHA gels was reduced from 47 % to 30 %, at RHs of 70 % and 85 %, respectively (Table 7.7 (a)).

By comparison, the porosity of CHA xerogels (42 to 54 %) at RHs in the range of 70 to 100 % was lower than that of the HA gels (56 to 63 %). However, the porosity of the CHA cryogel (81 %) was higher than the HA cryogel (70 %). The porosity was decreased with the increasing RH % as illustrated in Table 7.8 (a)-(b). The larger voids of the CHA gels were ranged between 10 and 1000 μm, but the interstitial pores were primarily at the range of 10 and 100 nm except the RH of 85 % (Figure 7.13).

Unlike the HA gels, the median pore diameter of the CHA gels were decreased with the increasing RH. Interestingly, the median pore diameter of the CHA xerogel (27.5 nm) at RH of 70 % was nearly 1.5 times as much as the HA xerogels (19.0 nm). However, there was no difference in median pore diameters at other RHs after the addition of carbonate in the HA gels. In addition, it did not cause the high porosity of the CHA xerogel at RH of 100 %, in comparison to the HA xerogel without carbonate.

Table 7.8 The influence of carbonate on the pore structures of HA gels: (a) porosity, skeletal density, and bulk density; (b) total intrusion volume, median pore diameter, and total pore area.

(a) Relative Humidity %	Porosity (%)	Skeletal Density (g cm $^{-3}$)	Bulk Density (g cm^{-3})
0	81.37 ± 6.63	2.15 ± 0.03	0.40 ± 0.14
70	54.01 ± 19.00	1.59 ±1.07	0.63 ± 0.19
85	50.05 ± 6.66	1.93 ± 0.01	0.96 ± 0.13
100	42.74 ± 17.17	2.01 ± 0.04	1.15 ±0.35

(b) Relative Humidity %	Total Intrusion Volume (cm^3 g^{-1})	Median Pore Diameter (nm)	Total Pore Area (m^2 g^{-1})
0	2.20 ± 0.92	36.15 ± 19.73	66.05 ± 1.72
70	0.85 ± 0.05	27.45 ±0.92	37.56 ± 1.30
85	0.53 ± 0.14	17.15 ± 13.36	7.89 ± 1.49
100	0.42 ± 0.27	10.30 ± 1.13	59.48 ± 25.78

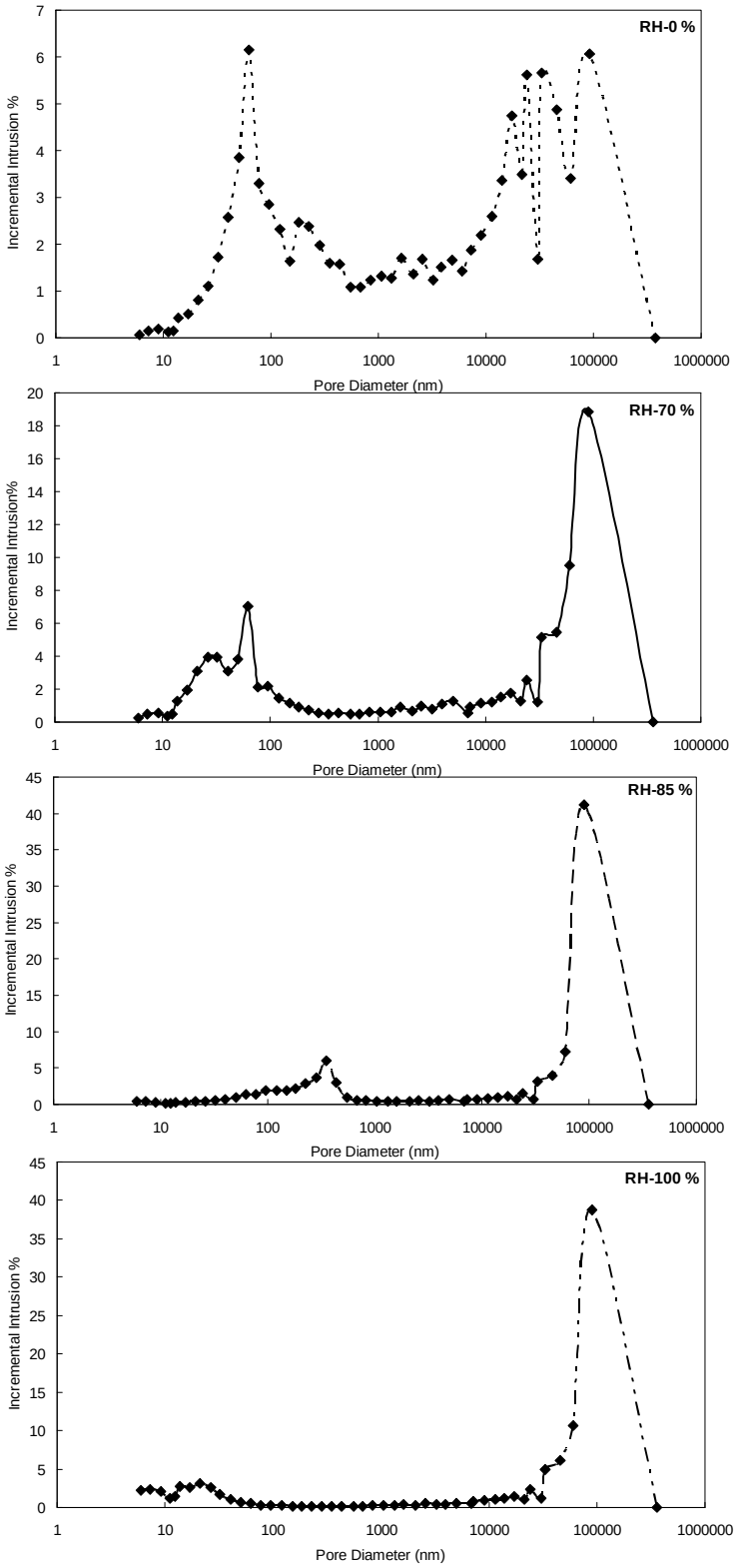

Figure 7.13 Mercury Intrusion curve of the CHA gels at RH of 0 %; RH of 70 %; RH of 85 %; RH of 100 %.

7.4 Discussion

7.4.1 The effect of ageing on the formation of the CaP gels

The physicochemical properties exhibited by CaP gel were strongly related to sol-gel processing conditions. The drying process is particularly an important step for gels formed from the liquid sol (shrinkage) as it has been demonstrated that the pore structure of the gel is heavly dependent upon capillary pressure generated during the drying stage. Also, during drying, a continuous increase in capillary pressure forces the particles to rearrange, and dissolution-reprecipitation phenomena may occur within the gel. This dissolution-reprecipitation can result in the formation of impurity phases or can form necks between the particles, enhancing mechanical integrity [Brinker and Scherer (1990)]. In the study, the various RHs were used to control the duration of the first stage of drying process. The generated capillary pressure of gels from the drying process was decreased as the duration of the first stage increased. Different RHs in drying regimes were designed to control the extent of these phenomena: capillary pressure forces and dissolution-reprecipitation, during processing.

By placing the gels into different RH environments, the period of ageing time available for dissolution-precipitation reactions to occur and the rate of evaporation were adjusted. In the first falling rate period (second stage) of drying process where shrinkage stops, the gel matrices can be hetergeneous because the liquid containing solutes (e.g., phosphates) evaporate at the surface causing the precipitation of a different phase [Brinker and Scherer (1990)]. The RH decides how long the dissolution-reprecipitation can occur and the rate of evaporation of liquid during the ageing process. Despite the significant change in processing, the XRD patterns of the CaP gels showed that an apatitic phase was formed in all conditions. This suggests that the different RHs in the drying regimes did

not interfere with the formation of the apatite, although impurity phases of OCP and calcite were detected in some cases. The presence of peaks indicative of calcite in the 'non-carbonate' containing gels may be attributed to the surface adsorption of carbonate to calcium phosphate phase. This is in agreement with the FTIR spectra, which showed the presence of phosphate groups of apatitic phases and a trace amount of carbonate. Although there was no calcite present at an RH of 0 % in the XRD patterns, the absorption of carbonate groups were displayed in FTIR analysis, implying the presence of amorphous calcite in HA gels, or the adsorption of carbonate onto the surface of the samples post-processing. In addition, small quantity of OCP appeared in the HA xerogel when aged at an RH of 100 %. The formation of trace amount of OCP in CaP gels at high RH might result from OCP being thermodynamically more stable than HA. Moreover, the solubility of OCP is higher than HA and is a metastable phase formed during the precipitation of a range of biominerals. OCP, therefore, is often present as a transient intermediate during precipitation from aqueous solutions [Dorozhkin (2007)]. As expected, the CaP gels were poorly crystalline, and were formed from submicrometer crystals more akin to those found in the body than with sintered ceramic monoliths.

Previous studies have reported that the ageing is responsible for the formation of pure apatite [Liu et al. (2001), Liu et al. (2002), Hsieh et al. (2001)], but have not evaluated the influence of changing process conditions. This is of significant importance since the the interaction between calcium and phosphate ions during processing determines composition and therefore gels of different Ca/P ratios may be formed. The EDS and XRF results (Table 7.1 and Table 7.2) showed different Ca/P ratios of the HA gels formed at various RH %, implying that chemical compositions are related to the RH %, which was not apparent from XRD. This may suggest the formation of X-ray amorphous

impurity phases, the presence of which was also suggested by the lower true density of the ceramic than would be expected for apatite. Theoretically, the calcium deficient HA would be formed in this study as the pH of sol mixture at 7.4 is below 9. However, it was found that only HA xerogels produced at RH of 70 % were calcium deficient HA as shown by the measured Ca/P ratio (1.58). It must be noted, however, that the formation of calcium rich phases such as $CaCO_3$ within the ceramic matrix could increase the Ca/P of the HA gel to higher than would be representative of the apatite phase within the gel.

7.4.2 The effect of ageing on the microstructure of HA gels

The true density of HA gels (2.5 to 2.7 g cm^{-3}) is considerably lower than the calculated density for stoichiometric HA (3.16 g cm^{-3}). This suggests that an amorphous calcium phosphate phase is present, as suggested by the large background apparent on the XRD pattern. The pore structure is also responsible for the low true density of the HA gels. As a new bonding was continuously formed during shrinkage in the drying process, the pore volume, and surface area of gels vary [Brinker and Scherer (1990)]. It has demonstrated that the shrinkage leads to the changes of the relative porosity, specific surface area, and particle size produced by the different drying behaviours (Table 7.3). While it is unlikely that any of the pore structure was not permeated by the helium gas, any hermetically closed porosity would have led to the measured values for true density being lower than expected.

Given that the volume of the HA gels following shrinkage (~12 to 18 %) was the same for each RH %, the shrinkage rate is considerably increased while the RH % is low. Because the RH % is low, the equilibration is reached more quickly. The stiffness of the network depends on the amount of shrinkage occurring during the drying process, as the

growth of necks improves the strength of the gel network [Brinker and Scherer (1990)]. In addition, the generated capillary pressure at lower RH is higher than that at high RH. At high RH %, the capillary pressure produced when water is expelled from the gel network is less than at low RH %. The low capillary pressure may result in the formation of a dense and strong gel network, and the precipitation of a secondary phase within the pore structure. This may explain why as the RH % was increased, the relative porosity of the HA gels was reduced (Table 7.3). Also, the true densities of HA gels (Table 7.3) were lower than the theoretical density of HA.

7.4.3 A comparison of porosity as determined by calculation and measured by mercury porosimetry

The results of mercury intrusion porosimetry would suggest that a network of interconnected pores was present within the CaP gel matrix. The presence of such a pore network in CaP gels has previously been demonstrated to improve bone in growth [Omae et al. (2006)]. The relative porosity as determined from geometrical measurements and the true density of the samples was not in accordance with the porosity by mercury porosimetry (Table 7.3 and Table 7.4 (a)). This disparity in values may be due to the presence of closed pores in the CaP gels. The total porosity by mercury porosimetry was evaluated by the skeletal density, and bulk density (Table 7.4 (a)). Unlike helium, mercury cannot intrude pores with small volume. Unless, there were no closed pores in the HA gels, the skeletal density would be in accordance with the true density. However, the skeletal density was slightly lower than the true density, suggesting that the HA gels may have blind pores. Therefore, the open porosity determined by mercury porosimetry was greater than that determined from geometrical measurements and the true density of the samples.

The proportion of porosity closed to penetration by mercury can be evaluated by subtracting the skeletal volume from the true volume, and then dividing by the true volume. There were 16 % and 19 % of closed pores present in HA xerogel at RH of 70 %, and 85 % respectively. In addition, irregular aggregation of CaP gel particles as shown in the TEM images (Figure 7.7) contributes to the accuracy of the skeletal volume. The irregular aggregation of CaP gel particles may contribute to the large voids between particles in the HA gels. Figure 7.8 shows that mercury intruded the ceramic structure even at the low pressure, which suggested the presence of large voids.

Excluding the reasons mentioned above, the difference of porosity produced by the different RH might also result from the pore size and numbers of pores. The HA gels tend to have small median pore as the RH % is increased, again likely because of reprecipitation of a secondary phase within the pore structure. Because of the large pore diameter of the HA cryogel (32.9 nm), the porosity (70 %) is increased. Although the pore diameter of the HA xerogel (11.7 nm) at RH of 100 % was less than half of that of the HA cryogel, the greater number of pores existing results in the high porosity (64 %, Table 7.4 (a)), and the increased intrusion volume (0.69 g^{-1}mL), compared with the other two drying regimes (Table 7.4 (b)). It is also a possibility that in some samples, pores were present that were below the detection limits of the instrument.

The TEM images (Figure 7.7 (a)-(d)) revealed irregularly shaped crystals, which may be responsible for a deviation between the real pore diameter and the calculated value by mercury porosimetry. Since the Washburn's equation is based on the assumption of spherical particles and cylindrical pores, this might cause the reduced accuracy of evaluation of the pore size of these irregular crystals, which explains why the specific

surface area measured by DVS (Figure 7.5) is not directly comparable with the total pore area measured by mercury porosimetry (Table 7.4 (b)). In addition, the total pore area did not increase with the reducing median pore diameter, which resulted from heterogeneous aggregation of particles and the subsequent pore structures.

7.4.4 The effect of carbonate on the formation of HA gels

After the addition of carbonate ions in addition to the apatitic phase, some of CHA gels also exhibited peaks in the XRD pattern indicative of calcite (Figure 7.9). In some samples there was no crystalline calcite present (0 and 100 % RH) but adsorption peaks were present on the FTIR spectra (Figure 7.10) that were indicative of the presence of carbonate groups, which may suggest that an X-ray amorphous calcite phase was present.

The alteration of compositions with ageing condition was shown by the massive fluctuation in Ca/P ratios. As expected, the incorporation of carbonate ions resulted in the increasing of Ca/P ratio (Table 7.5 and Table 7.6). However, there was no positive relation between the RH % and Ca/P ratio. The extremely high Ca/P by EDS of the CHA xerogel at RH of 70 % may be as a result of heterogeneity within the ceramic matrix and the formation of as much as 19.40 wt% of calcite (as determined from the stoichiometric equation) in the gel matrix. The addition of carbonate ions to the precipitation may also explain the changes in the true density exhibited by the gel. As the density of calcite is 2.71 g cm^{-3}, it might cause the reduction of the true densities.

The total intrusion volume of the CHA gels at RH of 100 % between 10 and 100 nm was not as much as that of the HA gels (Figure 7.13), suggesting that the porosity of the CHA xerogel at RH of 100 % was attributed to large voids. The larger pore size of the CHA

gels compared with the HA gels may be explained by the comparatively large size of calcite crystals reducing the efficacy of crystal packing. The presence of closed pore volume can be evaluated by the difference of the skeletal density and the true density. The result showed that 39.54 % of the pores present in the CHA xerogel at RH of 70 % were closed. As the RH was increased, the closed pore volumes were reduced, excluding the CHA cryogel. There were 23.1 % and 17.28 % of closed pores, respective of RH of 85 % and 100 %. However, at RH of 0 %, the volume of closed pores was reduced to 8.5 %.

Carbonate substitution results in reduction in the crystal size of the apatite when compared with HA gels, corresponding to a previous study [Barralet et al. (1998)]. The small size and irregular shape of the crystals causes loose aggregatation of particles, resulting in both increasing particle size and volume of closed pores (Table 7.7 (a)-(b), and Table 7.8). As the TEM images showed, the crystals of the CHA xerogel at RH of 70 % were the smallest and less irregular among all drying regimes, which imply strong adhesion between crystals. It has been demonstrated that the RH of the drying process of gels results in different chemical compositions. In addition, the calcium phosphate gels exhibited distinguished pore structures at certain RHs.

7.5 Conclusion

The effect of ageing on the physicochemical properties of calcium phosphate gels has been demonstrated. The various chemical compositions were dependent on RHs. The micro porous structures of CaP gels variously created by controlling the RH of drying procedures were significantly increased with respect to specific surface area, particle size, and open porosity. The differences in composition and microstructure can be attributed to

the formation of secondary phases such as calcite and the dissolution-reprecipitation reactions which can occur during ageing. It has shown that, to some extent, it is possible to control the pore size exhibited by CaP gels, simply by controlling process conditions

Chapter 8 Comparing the efficacy of calcium phosphate based matrices for the release of vancomycin hydrochloride

8.1 Introduction

Bone related infections such as osteomyelitis, which causes a loss of blood supply to the infected bone and spreads to adjacent tissues, are complications associated with open fractures and the placement of implants. Methiciline-resistant *Staphylococcus aureus* (MRSA) are the most refractory pathogens capable of causing such infections, and it is a major challenge to prevent infection during the surgical procedure. The treatment of osteomyelitis typically requires the removal of the injured tissue; however, bacteria are not thoroughly eradicated by debridement, and so the systemic administration of an antibiotic may also be required [Riggs et al. (1992)]. Vancomycin hydrochloride (VH) is an antibiotic that is specifically used against *Staphylococcus aureus* (*S. aureus*) in the treatment of bone related infections. In order to achieve the desired antibacterial effect, it is necessary to supply a relatively high dose for example, 500 mg to 5 g [Shinto et al. (1992), Korkusuz et al. (1993), Baker et al. (1988)], which can lead to both nephro- and ototoxicity [Saito et al. (2002), Carvalho Vila et al. (2007)]. A number of researchers have investigated the use of synthetic materials to allow the localised administration of VH to avoid systemic toxicity, which are capable of maintaining a bactericidal dose locally without systemic exposure. A local drug delivery system is advantageous because it is thought to decrease the systemic toxicity and side effects of parenteral antibiotics and it may also improve efficacy by delivering higher drug concentrations to infected bone [Radin (1997), Radin (2001)].

Poly(methyl methacrylate) (PMMA) beads or cements have been investigated widely for the localised delivery of VH [Vecsei and Barquet (1981), Habraken et al. (2007)], however, as they are non-resorbable following implantation, a second surgery is required to remove the beads following treatment. Furthermore, the highly exothermic polymerisation reaction of the PMMA cements has been shown to diminish the bactericidal efficacy of VH following an implantation [Gautier et al. (2000a)]. As a result, workers have focused on the development of degradable materials such as plaster of Paris [Dahner and Funderburk (1987)], fibrin [Zilch and Lambiris (1986)], poly (lactic acid) [Kanellakopoulou et al. (2000)], and hydroxyapatite (HA) [Saito et al. (2002), Habraken et al. (2007), Palazzo et al. (2005)]. The successful application of which would negate the need for a second procedure. Calcium phosphate (CaP) based materials such as HA, β-tricalcium phosphate (β-TCP), biphasic calcium phosphate, and dicalcium phosphate dehydrate-brushite in particular, have shown promise in their ability to locally deliver a therapeutic dose of bactericidal drugs [Radin et al. (1997), Palazzo et al. (2005), Xu et al. (2007), Kim et al. (2005), Stigter et al. (2004), Gbureck et al. (2008)].

Due to their compositional similarity to the mineral component of bone, CaP based ceramics have been used widely for the replacement of hard tissues [Barralet et al. (2002), Komlev et al. (2002)]. The first embodiment of HA used as a hard tissue replacement was supplied as a sintered ceramic monolith [Monroe et al. (1971)]. Although well tolerated following implantation in the body and able to form a bond with both hard and soft tissues, the monolithic nature of the graft replacement meant that preoperative knowledge of the defect was required prior to surgery, which limited clinical application. This major limitation led to the development of a range of technologies intended to widen clinical application by solving problems associated with manipulation.

Currently, CaP based bone graft replacements are supplied as granules [Komlev et al. (2002), Seshima et al. (2006)], carvable blocks [Shinto et al. (1992), Saito et al. (2002), Itokazu et al. (1998)], composites [Korkusuz et al. (1993), Tampieri et al. (2001), Suchanek and Yoshimura (1998)] and cement materials [Joosten et al. (2005), Gbureck et al. (2005a), Gbureck et al. (2007), Hamanishi et al. (1996)]. CaP cements (CPCs) have received significant attention as they are plastic following the combination of the powder and liquid components and can either be moulded to the irregular defects frequently encountered in orthopaedic and craniofacial surgery or can be applied in a minimally invasive manner using a hypodermic needle [Gbureck et al. (2005b)]. In addition, the majority of cement setting reactions proceed with only a minor exothermic and can proceed in ambient conditions, meaning that temperature sensitive molecules such as growth factors and some drugs can be incorporated into the cement matrix without the risk of thermal degradation.

As a result, some studies have reported the delivery of bone morphogenic proteins [Gammill and Sive (2000)], VEGF [Lode et al. (2007)] and nanomicelles [Itaka et al. (2007)] from hardened cement matrices with significant success. Furthermore, a number of research groups have investigated the local delivery of antibacterial drugs such as vancomycin from CPCs for the prophylactic treatment of implant related infections. Although there is little change in the temperature of CPCs during setting, there can be significant fluctuations in the pH of the setting cement slurries, which it is hypothesised, can have a marked influence on the eventual potency of drugs such as vancomycin.

In this study, the effect of pH on the release properties of a tetracalcium phosphate (TTCP)/dicalcium phosphate anhydrate (DCPA) cement system, the pH of which can

reach values of ~10 during setting, and a carbonated substituted HA (CHA) xerogel, which can also be processed at room temperature but with little or no fluctuation in pH were investigated. The release mechanisms of these calcium phosphate based materials were explored using the Higuchi and Peppas models and the efficacy of the released drug was determined using the broth dilution method.

8.2 Drug release *in vitro* study

8.2.1 Encapsulation of vancomycin chloride release

The CHA xerogel was manufactured in accordance with the method of CHA xerogel formed at an RH of 70 %, described in the section 7.2.

HA cements were made by mixing equimolar quantities of TTCP and DCPA (Merck, Germany). TTCP was prepared by sintering an equimolar mixture of DCPA (Mallinckrodt-Baker, Griesheim, Germany) and calcium carbonate (Mallinckrodt-Baker, Griesheim, Germany) at 1500 °C for 18 h followed by quenching in air. The cake was crushed with a pestle and mortar so that it would pass through a 355 μm sieve. The powder was milled in agate jars in a dry state to a median particle size of 10-15 μm. DCPA was ground in ethanol for 24 h to a median particle size of 1-2 μm. The cement was mixed to a powder to liquid ratio of 3.5 g cm^{-3}.

Vancomycin hydrochloride, VH (Sigma-Aldrich, Louis, USA) was mixed with the CHA xerogel, and HA cement in the ratio 200 mg gel to 1 mg VH. The mixture of CHA xerogel with VH was then homogenised within a nitrile mixing vessel, which subsequently resulted in the formation of a sol containing 0.5 wt% VH. After the VH had been loaded into the samples, cylindrical samples with final dimensions of approximately

diameter 6 mm and height 10 mm were fabricated using a 5 mL syringe. The samples were then dried in ambient conditions. The cement sample was then formed into cylindrical samples of around diameter 6 mm and height 12 mm in a PTFE split mould. The cement samples were then allowed to harden for a period of 24 h in ambient conditions before further study.

CaP based materials loaded with and without VH were immersed in 15 mL of 100 mM tris-buffered saline (pH 7.4) (Fisher Scientific, Loughborough, UK). All samples were placed on a horizontally rotating shaker at 90 rpm in the 37 ˚C environment. At each set time point (0.5, 1, 2, 4, 7, 24, 48, 72, 96, 120, 144, and 168h) 7 mL of eluent was withdrawn from VH-containing CHA xerogel/HA cement and control CHA xerogel/HA cement. The eluent was then stored at -4 ˚C before VH content was determined. After each withdrawal, the elution medium was refilled with 7 mL of tris-buffered saline.

8.2.2 Vancomycin hydrochloride release *in vitro* study

VH release was monitored by measuring the absorbance of the elution medium at 280 nm using a UV-visible spectrophotometer. VH concentration was determined from the average of three absorbance readings using a corresponding calibration curve (0.05-0.2 mg/mL), expressed in terms of mg of VH per mL of tris-buffered saline. To minimise any potential interference from the calcium and phosphate ions in solution, corresponding control CaP based materials at each time point were used to baseline the data. After the elution period, each sample was dissolved in 20 mL of 3 wt% ethylenediaminetetraacetatic acid tetrasodium salt hydrate (Na_4-EDTA) (Sigma-Aldrich, Gillingham UK) to release any residual VH within the CaP based materials. The

concentration of the resulting solution was calculated by the calibration curve based on a VH- Na_4-EDTA solution.

8.2.3 Microbiological activity assay

Agar diffusion

The effectiveness of the VH loaded HA cements and CHA xerogels was measured by agar diffusion. *S. aureus* (0.9×10^6 cells/mL) was grown in tryptone soya broth (OXOID, Hampshire, England) and cultured on nutrient agar (OXOID, Hampshire, England) with ~ 0.2 g of each sample placed in the centre of the agar plate. The zones of bacterial inhibition were recorded and compared with the inhibition zones of cements and gels without VH.

Broth dilution

The antibacterial activity of VH released from the CaP based materials was analysed by the broth dilution method, using which the minimum inhibitory concentration (MIC) of VH is 1 μg mL^{-1} [Dion et al. (2005)] determined by recording the drug concentration that inhibited visible growth of *S. aureus* (ATCC 29523, NCIMB, Aberdeen, UK). A bacterial culture was prepared prior to conducting the assays by introducing Müeller-Hinton broth (OXOID, Hampshire, England) with *S. aureus*, and allowing the bacteria to proliferate overnight in an incubator at 37 ˚C. Then 4 mL of Müeller-Hinton broth with *S. aureus* was withdrawn into 10 mL of Müeller-Hinton broth, corresponding to approximately 1×10^6 CFU/mL. A VH-containing sample was added into the Müeller-Hinton broth with *S. aureus* at a 1:1 ratio. A bijou containing 500 μL of Müeller-Hinton broth with *S. aureus* served as a positive control and a negative control was prepared only with 500 μL of Müeller-Hinton broth. All samples were incubated at 37 ˚C for 16-24 h. Antibacterial activity was determined by the lack of turbidity of the sample. Antibacterial activity

assays were conducted for both control samples and CaP based materials loaded VH samples at each time point (see page 131).

8.3 Result

8.3.1 Physicochemical properties of calcium phosphate materials

After setting, the TTCP/DCPA cement was shown to form a matrix that consisted predominantly of HA with some un-reacted TTCP (Figure 8.1). The broad peaks at 32º 2θ were indicative of the presence of a poorly crystalline apatitic phase. The diffraction pattern for brushite cement exhibited peaks distinctive of brushite (~20º, 23º, 29º, 30º, 33º, 35º, 37º, 39º 2θ) with a small quantity of unreacted β-TCP (Figure 8.1). As expected, the diffraction pattern for the CHA xerogel exhibited an even broader and less defined peak of apatite at ~32º 2θ (Figure 8.2). In addition to the broad peak which indicated the presence of apatite, the diffraction pattern for the CHA xerogel exhibited calcite peaks at 29º, 36º and 39º 2θ which suggested the calcite was formed in the xerogel matrix.

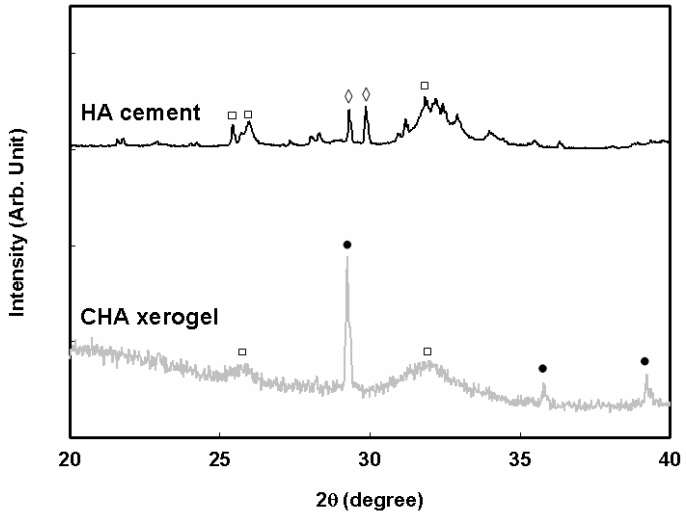

Figure 8.1 X-ray diffraction patterns of the HA cement indicated that some TTCP remained unreacted (28˚ and 29˚ 2θ), and presence of apatite at ~32˚ 2θ. The CHA xerogel showed that there exhibited apatite (at ~ 32˚), and calcite (at 29-39˚). The peaks marked on the patterns indicated the presence of □: apatite, ●: calcite. ◊: TTCP.

The presence of carbonate ions in the CHA xerogel was further demonstrated by FTIR analysis (Figure 8.2), which exhibited peaks at 870 and 1412 cm^{-1} attributable to the ν2 and ν3 vibrations of the carbonate molecule. The carbonate peak at 1650 cm^{-1} resulted from the surface adsorption rather than the substitution. Prior to elution, the spectra for the CHA xerogel contained peaks that were indicative of the presence of PO_4^{3-} groups (562, 673 and 1016 cm^{-1}). The hydroxyl group of the CHA xerogel was present at 600 cm^{-1}. The intensity of the CHA xerogel after the elution period remained relatively unchanged. In the case of the HA cement, the HPO_4^{2-} peak at 603 cm^{-1} was shown to increase in intensity after the elution period whereas the remainder of the spectra remained relatively unchanged, suggesting no compositional transformation. (Figure 8.2). Although the VH was expected to show at 1700 to 1380 cm^{-1} [Radin and Ducheyne (2007)], the presence of carbonate was predominant in the similar range (Figure 8.3). Therefore, no peak indicative of VH was appeared. Encapsulation of VH in the CHA xerogel did not influence the chemical compositions of CHA.

The specific surface areas exhibited by the HA cement, and CHA xerogel were markedly different. The HA cement exhibited a specific surface area of 17 ± 3 $m^2 g^{-1}$, whereas the CHA xerogel exhibited a specific surface area of 42 ± 2 $m^2 g^{-1}$ (Table 8.1).

Table 8.1 The physical properties exhibited by the calcium phosphate based matrices.

Sample	Relative porosity (%)	Specific surface area ($m^2 g^{-1}$)	Modal pore diameter (nm)
HA cement	43 ± 2	17 ± 3	580 [Barralet et al.2002]
CHA xerogel	55 ± 5	42 ± 2	9 [Barralet et al.1996]]

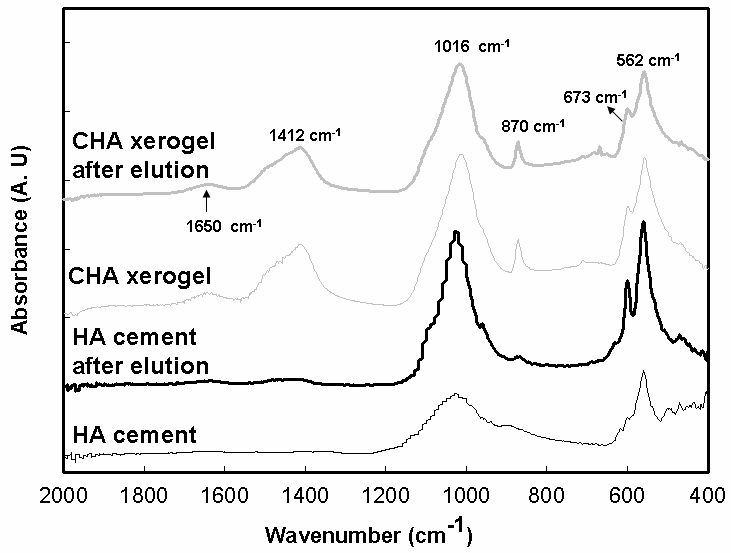

Figure 8.2 FTIR spectra of the CHA xerogel and HA cement. The presence of carbonate of the CHA xerogel was indicated by peaks at approximately 1412 cm^{-1}. The spectra of all calcium phosphate based materials indicated that the presence of phosphate groups at the range of 1070-1140 cm^{-1}. In addition, the peak at 870 cm^{-1} of the CHA xerogel was indicative of the presence of carbonate groups.

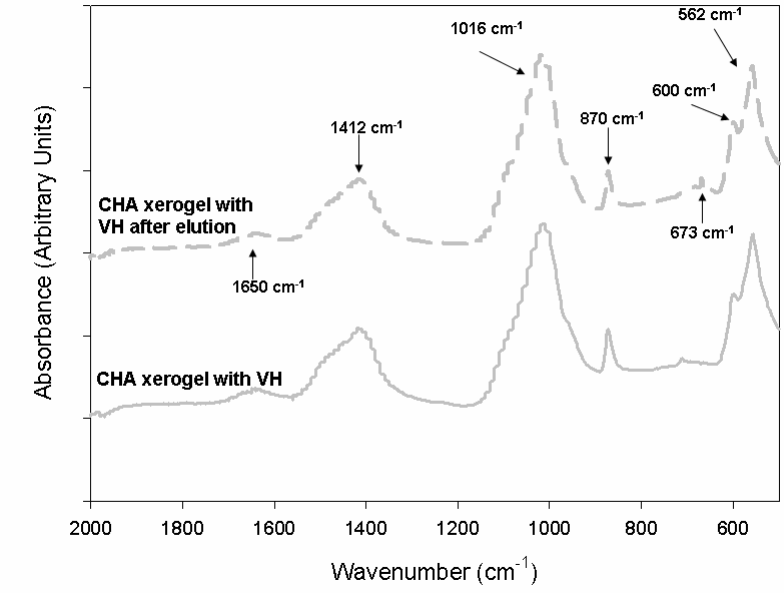

Figure 8.3 FTIR spectra of the CHA xerogel with VH. The presence of VH has not changed the chemical composition of CHA.

The HA cement exhibited a relative porosity of 43 ± 2 %, and the CHA xerogel exhibited a higher relative porosity of 55 ± 5 % (Table 8.1). Although the porosities of both HA based matrices were similar, according to literature values, the modal pore diameter of the HA cement (580 nm) was much higher than the CHA xerogel (9 nm).

The HA cement exhibited a total porosity of 39 % less than the total porosity of CHA xerogel (67 %) as listed in the Table 8.2. Figure 8.4 showed that the pore size distribution of the CHA xerogel ranged between 12 nm and 95 nm. By comparison, the pores of the HA cement were distributed in the broader range of 11 nm to 1 μm (Figure 8.4). The skeletal density of HA cement (2.76 g cm^{-3}) was 87.3 % of theoretical value (3.16 g cm^{-3}). After loading the VH, the main pore size distribution remained in the same range as the CHA xerogel without VH (Figure 8.4), but minor pores were distributed at 1 μm. In addition, the porosity of the CHA xerogel with VH was obviously reduced to 57 % (Table 8.2). For the HA cement, there was a slightly change of pore size distribution, and porosity. The porosity was reduced to 36 % after loading the VH into the HA cement (Table 8.2). Moreover, both HA based matrices had similar median pore diameter (26.8 nm for CHA xerogel, 26.4 nm for HA cement), and both median pore diameter were reduced half after loading VH (Table 8.2).

The morphology of the CHA xerogel and HA cement was featureless although it indicated that the particles of CHA xerogel and HA cement were aggregated (Figure 8.5 (a)-(b)).

Table 8.2 Porosity of the calcium phosphate based matrices with/without VH by mercury intrusion [one measurement].

Samples	Total Intrusion Volume ($cm^3\ g^{-1}$)	Median Pore Diameter (nm)	Skeletal Density ($g\ cm^{-3}$)	Porosity (%)
CHA xerogel	0.88	26.8	2.34	67
CHA xerogel with VH	0.57	14.5	2.33	57
HA cement	0.27	26.4	2.76	39
HA cement with VH	0.21	16.1	2.66	36

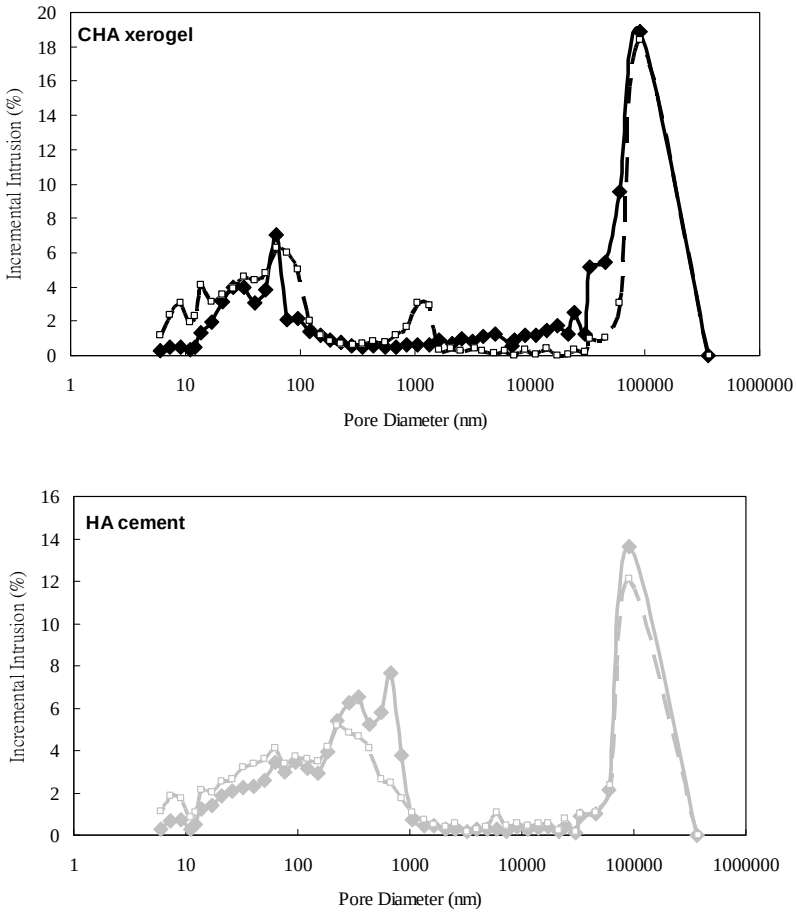

Figure 8.4 Mercury Intrusion curve of the CHA xerogel (black line with dot) and the CHA xerogel with VH (black line with hollow dot); the HA cement (grey line with dot) and HA cement with VH (grey line with hollow dot).

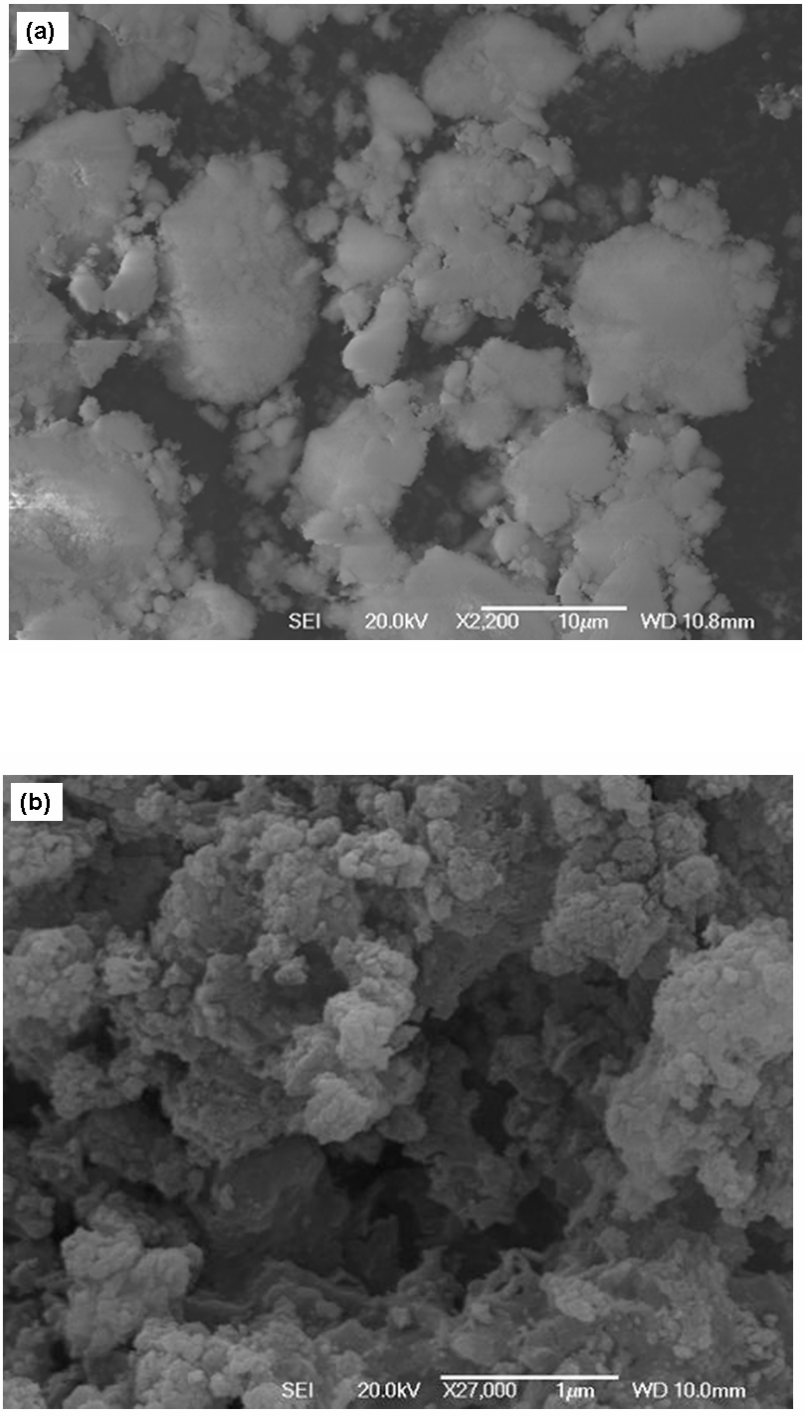

Figure 8.5 The SEM images of (a) CHA xerogel; (b) HA cement.

8.3.2 Efficacy of vancomycin release *in vitro* study

The significant difference in pore size distributions of these calcium phosphate based materials were expected to result in distinct release profiles, with the CHA xerogel releasing VH at a slower rate than the HA cements. Over the first 24 h, however, VH was released more rapidly from the CHA xerogel than from the HA cement matrix (Figure 8.6). Indeed, between 24 and 96 h of ageing, the VH was released significantly ($p<0.05$) more slowly from the HA cement than the CHA xerogel. After 48 h, the VH release from the CHA xerogel achieved a constant release rate. At the end of elution, there were 82 % of VH released from the CHA xerogel. 76 % of VH was released from the HA cement.

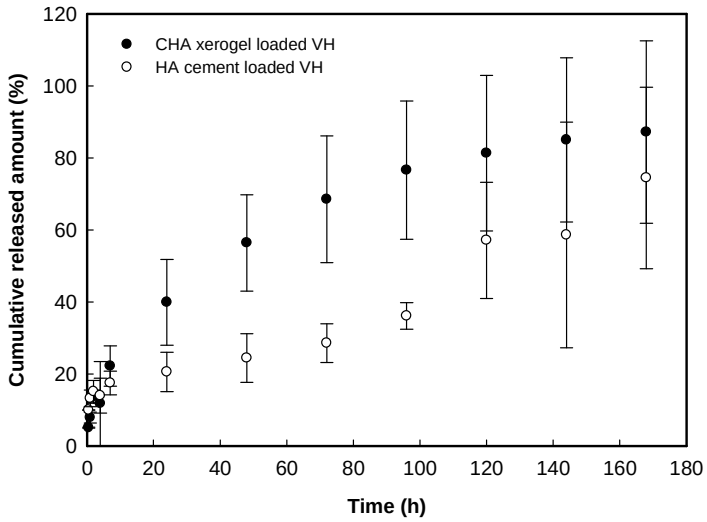

Figure 8.6 VH was released more rapidly from the CHA xerogel than the HA cement within 24 h. The cumulative release of VH (%) of the CHA xerogel was higher than that of VH of the HA cement after 168 h elution.

8.3.3 Evaluation of vancomycin release kinetics

The VH release kinetics were analysed using the Higuchi and Peppas models since the Higuchi model can adequately described the release of water soluble/low solubility drug incorporated in semi-solid/solid matrices. Following appraisal of the release profiles, Peppas derived n values (release exponent) for different diffusion conditions and shapes of drug were also determined. The VH release from the CHA xerogel suggested that the

drug release followed Fick's law (Table 8.3). The release of VH from the HA cement, demonstrated a poor fit with both the Peppas and Higuchi models, suggesting either that the VH released from the HA cement followed more than one diffusion mechanism or heterogeneity within the ceramic matrix.

Table 8.3 The release kinetics of VH of calcium phosphate based matrices by Higuchi and Peppas models. M [%]: cumulative released amount, K_H: release constant, a: release constant, b: release exponent.

Matrices	Higuchi model $M=K_H \times t^{0.5}$		Peppas model $M=a \times t^b$		
	K_H	r^2	a	b	r^2
CHA xerogel	7.39	0.98	9.78	0.44	0.98
HA cement	4.77	0.85	3.94	0.54	0.85

8.3.4 Microbiological activity of vancomycin

Figure 8.7 (a)-(d) shows the sizes of the inhibition zones formed around each matrix when the CHA xerogel and the HA cement with/without VH were placed onto a culture of *S. aureus*. HA cement showed its inhibition zone (2.67 ± 0.72 mm) was as much as the CHA xerogel (2.78 ± 1.13 mm), meaning there was sufficient active VH inside these matrices to inhibit the growth of bacteria. By comparison, the CHA xerogel without VH showed no bactericidal effect. However, interestingly, the HA cement control has formed the inhibition zone around 6.67 ± 0.54 mm (Table 8.4).

Table 8.4 Comparison of the inhibition zone of CHA xerogel and HA cement with/without VH.

Delivery Matrix		Inhibition Zone (mm)
CHA xerogel	Control	0
	VH	2.78 ± 1.13
HA cement	Control	6.67 ± 0.54
	VH	2.67 ± 0.72

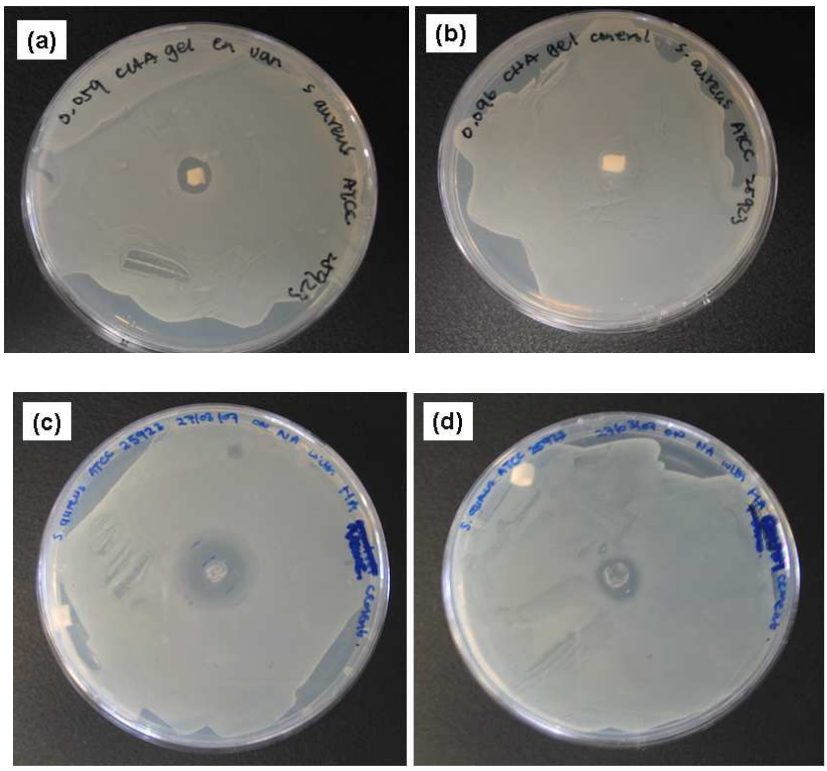

Figure 8.7 The image of inhibition zone of (a) CHA xerogel control and (b) CHA xerogel encapsulated VH; (c) HA cement and (d) HA cement encapsulated VH.

In the case of the CHA xerogel, the sufficient VH was released to inhibit bacterial growth until 72 h elution (Figure 8.8). Therefore, the release VH from the CHA xerogel in *S. aureus* was shown a transparent solution (Figure 8.9). Sufficient VH was also released for 168 h from the HA cement following immersion (Figure 8.8). Surprisingly, however, the release VH from the HA cement was opaque (Figure 8.9). The VH released from the HA cement did not inhibit bacterial growth at any point during the elution period (Table 8.5), explaining the cloudy broth solution with the release VH from the HA cement. To further verify the assumption of the effect of pH on the microbiological activity of VH, the pH variation of the HA cement during setting was monitored with time (Figure 8.10). These results showed that the HA cement exhibited a basic pH value peaking at pH 9.4 after 5 min.

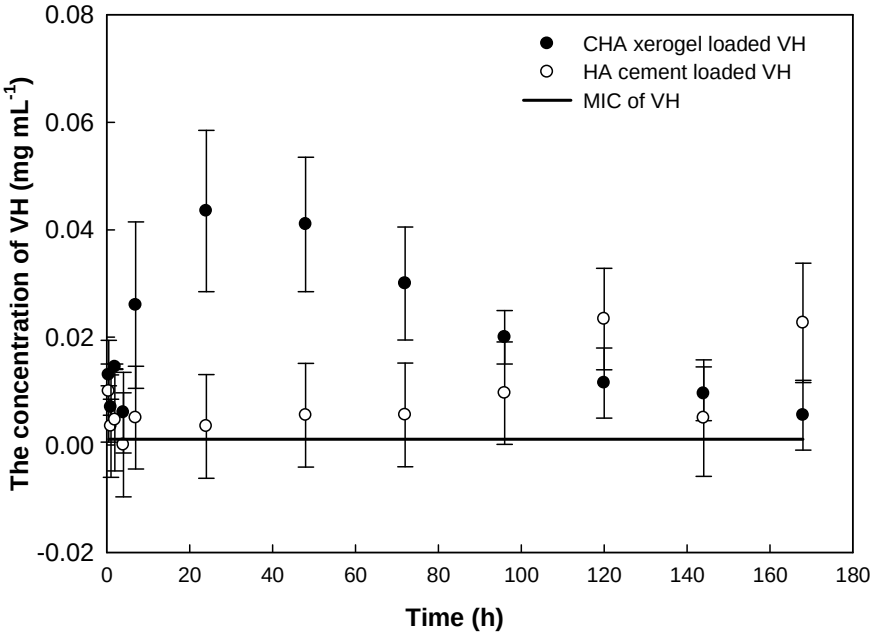

Figure 8.8 Concentrations of the eluent following different periods of ageing. Also, included in the figure is a line representing the minimum inhibitory concentration (MIC) required to inhibit the growth of *S. aureus*..

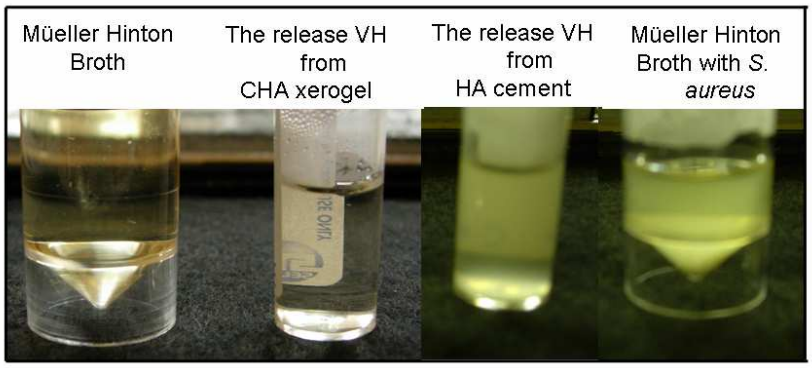

Figure 8.9 The release VH from the CHA xerogel in *S. aureus* was as clear as the Müeller Hinton broth, but the release VH from the HA cement in *S. aureus* was opaque, like the broth with *S. aureus*.

Table 8.5 Summary of the results obtained from the antimicrobial assays performed using the VH elution from each calcium phosphate based matrices.

Sample	VH (mg cm^{-3}) of Day 1	VH (mg cm^{-3}) of Day 2	VH (mg cm^{-3}) of Day 3	VH (mg cm^{-3}) of Day 4	VH (mg cm^{-3}) of Day 5
CHA xerogel (control)	0	0	0	0	0
	+	+	+	+	+
CHA xerogel loaded VH	0.04±0.02	0.04±0.01	0.03±0.01	0.02±0.00	0.01±0.00
	-	-	-	-	-
HA cement (control)	0	0	0	0	0
	+	+	+	+	+
HA cement loaded VH	3.43e-3	5.51e-3	5.59e-3	9.23e-3	0.02±0.00
	+	+	+	+	+

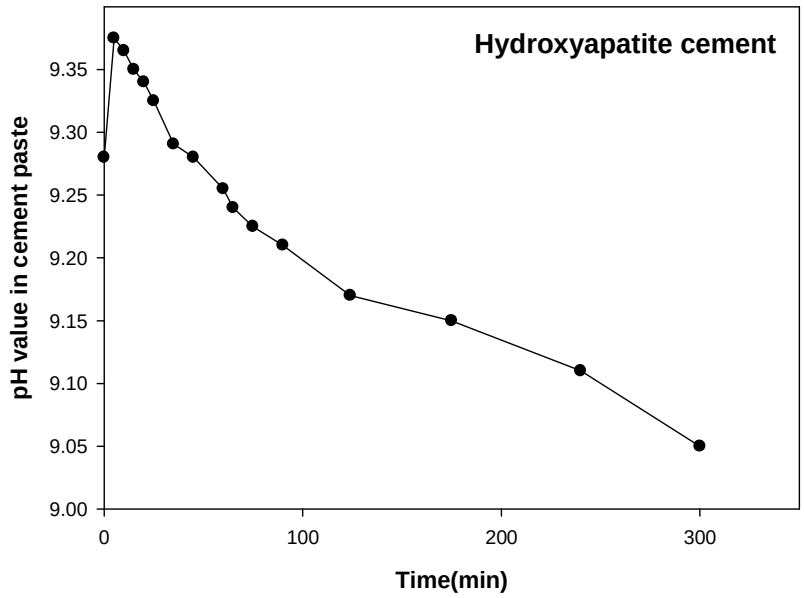

Figure 8.10 The pH variation in the HA cement during setting. The pH of cement paste with time was shown that the cement matrix exhibited a basic pH value peaking at pH 9.4 after 5 min.

8.4 Discussion

8.4.1 The effect of calcium phosphate matrices on the delivery antibiotics

CaP based ceramics and composites have been investigated widely in the delivery of prophylactic doses of drugs following implantation. The majority of studies have investigated the incorporation of active molecules into ceramics following manufacture, since high temperatures are likely to have a derogatory effect on the activity of the release drug. In these systems, CaP matrices are typically impregnated with the drug by soaking the granules in a solution of the drug (in the presence and absence of a vacuum) and by dynamic compaction and isostatic compression [Gautier et al. (2000b), Itokazu et al. (1998), Obadia et al. (2003), Gautier et al. (2001),]. Using these mechanisms, most studies have demonstrated the successful delivery of gentamycin, bisphosphonates, polymyxin B, and VH [Komlev et al. (2002), Seshima et al. (2006), Obadia et al. (2003),

Gautier et al. (2000b), Stallmann et al. (2006), Kimakhe et al. (1999)] *in vitro* and *in vivo*. Clinically, antibiotic loaded HA blocks have been shown to be successful for the delivery of gentamicin sulphate/VH in the clinical treatment of implanted-associated chronic osteomyelitis in an animal model [Shinto et al. (1992), Korkusuz et al. (1993)]. Although some studies has successfully demonstrated with the adsorption of active molecules into preformed CaP matrices, in the most part the drugs were absorbed onto the surface of the implants, meaning that the drug release was rapid and difficult to control. CaP cements have the significant advantage of setting at ambient temperatures, which means that active molecules can be incorporated into the matrices during manufacture; as a result of the distribution of active molecules throughout the cement matrix is homogeneous.

8.4.2 The effect of pH on the function of vancomycin

This study, however, has demonstrated that although the VH can be released by a HA cement matrix, the released VH exhibited no bactericidal properties. The ineffectiveness of the VH against *S. aureus* can be attributed to pH fluctuations during the cement setting. The pH of the cement was shown to have a peak at pH 9.4 (Figure 8.10). The pharmaceutical literature [Antipas et al. (1994)] has demonstrated that at such high pH values, the asparagine residues of VH become deamidated, which diminishes its potency against *S. aureus*. Deamidation changes the conformation of VH, which in turn influences the ability of VH to complex N-acetylmuramic acid (NAM) and N-acetylglucosamine (NAG), which are essential components of gram positive bacterial cell walls [Reynolds (1989)]. To achieve optimum activity, the VH must form a cyclic imide intermediate. The formation of such an intermediate is favoured at lower pH values. At high pH values the structure of the polypeptide becomes less compact and as consequence the distance

between reacting atoms increases and therefore the cyclic imide intermediate is thermodynamically less likely to form.

8.4.3 Kinetics of released vancomycin

Interestingly, in this study, it has been found that the release of VH from the HA cement followed neither the Higuchi or Peppas model and therefore the matrix does not conform to the underlying assumptions of these models. This may result from there being so little water in the HA cement paste while VH was added. The trace amount of water in the HA cement paste might affect the even distribution of VH, and reduce the dissolution of VH. It is hypothesised therefore that the ceramic matrix was not homogeneous or that two distinct forms of the drug of different solubility were present. Indeed, the HA based cement contained un-reacted and basic TTCP particles which would have caused a distinct rise in pH in their immediate vicinity causing the formation of the less soluble free VH base. The presence of such basic regions within the cement matrix may explain why the rate of release followed neither model.

8.4.4 The bactericidal effect of calcium phosphate matrices

Although some studies have shown that similar CaP based cement formulations can exhibit an antimicrobial effect surrounding the cements following an implantation [Korkusuz et al. (1993), Gbureck et al. (2005a)], it is possible that the basic pH values surrounding the implant themselves inhibited bacterial growth [Gbureck et al. (2005c)] rather than the release of an active dose of the antibiotic. Indeed, it has previously been demonstrated that without VH, HA cements comprising TTCP and DCPA exhibited an inhibition zone in a culture of *S. aureus* higher than when the same material was loaded with VH [Jiang et al. (2008)]. This effect also has been exploited in the development of antibacterial cement formulations by the incorporation of potassium substitutions into the

cement precursors. The bactericidal effect of the cement was attributed to a local pH increase alone [Gbureck et al. (2005c)].

8.4.5 The effect of microstructures on the release kinetics

In addition to calcium phosphate cements, bioceramic gels can also be processed at room temperature and consequently they have been investigated for the delivery of heat sensitive molecules. They typically exhibit a higher specific surface area than cements, meaning that a larger quantity of drug molecules per unit mass can be adsorbed onto the CHA xerogels (42.3 m^2 g^{-1}, Table 7.7 (b)) than the HA cements (17.4 m^2 g^{-1}). Calcium polyphosphate gels, for example, have been shown to deliver VH over a period of 144 h *in vitro* [Dion et al. (2005)]. This study has demonstrated that VH could be continuously released from the CHA xerogels for 168 h (Figure 8.6). Radin et al. have evaluated the use of silica based gels in the release of a range of biologically active molecules, including drugs, growth factors and proteins. They have demonstrated that it is possible to control the release of macromolecules of >10 kDa and have concluded that the pore size of molecules of silica sol-gels are contributed to the release kinetics of a dextran with various molecular weights [Radin et al. (2008)].

In this work, the CHA xerogels was used to release VH as the particle sizes of CHA xerogels (9 nm) [Barralet et al. (1996)] are smaller than HA cements (580 nm) [Barralet et al. (2002)]. Nevertheless, the data suggest that the small pore size of the ceramic matrix does not have a marked influence on VH release. This might be attributed to the spherical size of VH (5 nm^2), the aggregation of VH by forming dimer, and the weak bonding exists between CHA xerogel and VH [Loll et al. (2000)]. In addtion, the porosity of CaP matrices plays an important role in the release of VH as the release rate of VH

was increased with the increasing porosity (Table 8.1). The VH was released faster from the CHA xerogel than the HA cement due to 67 % of the porosity inside the CHA xerogel (Table 8.2).

8.5 Conclusion

In this study it has been demonstrated that sufficient VH can be delivered from the CaP bioceramic matrices at sufficient concentrations to exceed the MIC for *S. aureus* for 168 h. The pH in the ceramic matrix during processing is a very important consideration in the effectiveness of the released drug against the bacteria. In the basic cement formulation (pH 9.4), the VH that was delivered was ineffective against *S. aureus* and this was thought to be due to deamidation of the asparagine residues in the drug during the setting. The findings of this study illustrate the importance of evaluating the antibacterial efficacy of drugs loaded into material for *in vivo* drug release, rather than simply monitoring release.

Chapter 9 Calcium phosphate cryogels for enzyme encapsulation

9.1 Introduction

The sol-gel process has been used for the encapsulation of biomolecules in biosensors, and to produce carriers for the delivery of therapeutic molecules in reparative medicine [Jin and Brennan (2002)]. Silica gels, for example, have been successfully used for the encapsulation of horseradish peroxidase (HRP). They are, however, traditionally made using the tetraethyl orthosilicate (TEOS) or tetramethoxy silane (TMOS), which have been shown to be toxic and can reduce enzyme activity [Kadnikova and Kostić (2002), Radin et al. (2001)]. Consequently, rather than using TEOS or TMOS, some researchers have used sodium silicate precursors. Although this may have solved issues related to the toxicity of the sol-gel, loading efficiency was shown to be low [Bhatia et al. (2002), Masahiro et al. (2007)]. Efforts have also been made to enhance enzyme activity by the addition of polymers, dendrimers and sugars into the matrix of silica sol-gels with limited success [Lin et al. (2007), Wang et al. (2007), Miller et al. (2006), Kitsugi et al. (1995)].

Although silica based materials have been shown to be tolerated *in vivo*, the use of toxic reactants and the dissimilarity of the composition to that of hard tissue, means that they could not form a significant bond with hard tissues [Kitsugi et al. (1995)]. In comparison, calcium phosphate (CaP) based ceramic materials have been used as hard tissue replacements and prosthesis coatings for several decades [Appleford et al. (2009)]. Since they share a similar composition to the mineral component of bone, they are well tolerated in the body and form a little understood bond with both hard and soft tissues [Kitsugi et al. (1993)]. Traditionally, CaP based ceramics were made by a high

temperature process, which precluded the incorporation of temperature sensitive therapeutic proteins during manufacture. The subsequent development of CaP based cement (CPC) materials [Brown and Chow (1983)], which set in ambient conditions, allowed the delivery of proteins such as bone morphogenic protein [Ruhé et al. (2004)] and transforming growth factor β [Kroese-Deutmana et al. (2005)].

Although CPCs have been successfully used as a carrier of therapeutic compounds [Otsuka et al. (1994), Bohner et al. (1997)], the macroporous structure (10-100 μm) of the hardened product has restricted their use for the encapsulation of enzymes. By forming hydroxyapatite (HA) using a precipitation reaction, it is possible to manipulate process conditions to form a CaP based sol-gel [Barralet et al. (2002)]. In common with the cement hardening reaction, these sol-gel materials are formed in ambient conditions and with relatively little pH fluctuation. What gives them an important advantage over CPCs is that by controlling the rate of removal of the liquid phase, it is possible to exercise some form of control over pore size, thus enabling control over release rate. Previous work [Barralet et al. (2002)] has shown that apatite based gels can store proteins such as albumin for a period of 52 weeks *in vitro* with little undesired release from the matrix.

Alkaline phosphatase (ALP) is one enzyme that has been encapsulated in glass, ceramic and polymeric matrices, as well as being immobilised on the surface of metallic implants [Nishioka et al. (2006), Beortsen and van den Bos (1992)]. ALP has been investigated widely as it has been implicated with the mineralisation of newly forming bone [Hessle et al. (2002)]. Indeed, tissue non-specific ALP (TNAP) is found on the surface of osteoblast membranes and is present in high concentrations in the matrix vesicles excreted from

these cells during the mineralisation process [Bernhardt et al. (2008)]. Recent work has shown that ALP functions by removing pyrophosphate ions, potent inhibitors of HA crystal formation, which creates localised supersaturation with respect HA and crystal deposition [Anderson et al. (2004)]. ALP has previously been encapsulated in TMOS based silica gels, although the activity of the encapsulated ALP was shown to be relatively low [Braun et al. (1990)]. Other studies have shown that encapsulation of ALP in silica based sol-gels could preserve activity, even during storage in acidic environments [Frenkel-Mullerad and Avnir (2005)]. In previous studies, relatively low ALP activity has been proposed to be as a result of poor mass transport through the mesoporous gel systems, low loading efficiencies and enzyme desorption. Attempts have been made to address the mass transport problem, through the incorporation of bimodal pore size sol-gel (2-3 nm/10-40 nm) [Wang and Caruso (2005)].

Here, the use of a CaP based cryogel material for the encapsulation of ALP was evaluated. The activity of the ALP was monitored over a period of 14 days and compared with the activity of HRP, a model enzyme often used for evaluating the efficacy of encapsulation. The influence of protein incorporation into the CaP matrix during fabrication on the composition and pore structures of the gel material were investigated. In addition, Michaelis-Menten equation and Lineweaver-Burk equation were used for comparison of the kinetic data in the enzyme storage experiment.

9.2. Horseradish Peroxidase/ Alkaline phosphatase storage

9.2.1 Encapsulation of Horseradish Peroxidase/ Alkaline phosphatase

The carbonate substituted hydroxyapatite (CHA) cryogel was formed at an RH of 0 % the same as the method described in the section 7.2 in Chapter 7.

For HRP encapsulation, HRP (169 units/mg, Sigma, Germany) was mixed with the CHA cryogel in the ratio 800 mg CHA cryogels: 2 mg HRP. The mixture was then homogenised within a nitrile mixing vessel resulting in CHA cryogels containing 0.25 wt % HRP. After the HRP had been loaded into the samples, the gels were then dried in a freeze drier. For ALP encapsulation 1.46 units/mg of ALP (Fluka, Gillingham, UK) were mixed with CHA cryogel in the ratio 97 g CHA cryogels: 3 g ALP. The mixture was then homogenised for 15 min in a nitrile mixing vessel the resulting apatite slurry containing 3 wt % ALP was filtered using a water aspirated vacuum pump before freeze drying.

9.2.2 Efficacy of Horseradish Peroxidase/ Alkaline phosphatase *in vitro* storage

The amount of protein released from the CHA cryogel with ALP/HRP was determined using the BCA assay. According to the amount of reduction of the Cu^{2+} to Cu^{+} by protein, the protein can be quantified by monitoring the cuprous cation, using UV-Vis spectrophotometer at 562 nm [Sigma Ltd. (2001)]. The calibration curve consisted of a known concentration of bovine serum albumin (BSA) between 0-1000 µg/mL. The blank was made of a phosphate buffer with no enzyme. 100 µL of a sample/blank was mixed with 2 mL of the BCA working reagent. Then, the solution was incubated in the 37 ˚C incubator for 30 min. CHA cryogel loaded with HRP (n=3) were immersed in 10 mL of 100 mM KH_2PO_4 buffer (pH 6) over a week, and control CHA cryogel were immersed in an identical process. All samples were placed in a horizontally rotating shaker at 90 rpm in a 37 ˚C environment. At selected time points between 0.5 h, and 216 h observations were made by collecting all released medium and refreshing the buffer after each withdrawal from the CHA cryogel with HRP. Then the absorbance of the ABTS [2,2'-azino-di-(3-ethylbenzthiazoline-6-sulphonic acid)] cation at 414 nm and the activity of

HRP were measured. CHA cryogel loaded with ALP (n=3) were immersed in 5 ml of 100 mM tris-HCL buffer (pH 7.4) over a week, and control CHA cryogel were immersed in an identical process. At the end of immersing, each sample was dissolved in 20 mL of 3 wt% ethylenediaminetetraacetatic acid tetrasodium salt hydrate (Na_4-EDTA) to dissolve any residual HRP within the CHA cryogel.

9.2.3 Activity of Horseradish Peroxidase/ Alkaline phosphatase

The activity of HRP was measured based on the oxidation of 30 μM ABTS catalysed by 2 mg HRP loaded into CHA cryogel in the presence of 9.79 μM H_2O_2 to the ABTS cation. The interconversion of ABTS (λmax=340 nm) to its radical cation (λmax=414 nm) was monitored using a UV-Vis spectrophotometer as a function of time. The formation of ABTS cation indicated the HRP activity by the appearance of a green coloured solution. The control experiment was performed using an equal concentration of HRP in the 100 mM pH 6 phosphate buffer solutions under the same conditions.

The activity of ALP was determined by measuring release of phosphate ions from pyrophosphate solutions [Xu et al. (1991)]. 5 mL of each pyrophosphate concentration ranging from 0-20 mM was added to 5 mL of 1U/mL ALP and then mixed. 160 μL of the pyrophosphate/ALP solution was sampled every 2 minutes during the reaction. Then, 330 μL of 5 % trichloroacetic acid and 5 mM copper sulphate (Fisher scientific, Loughborough, UK) was added, following by the introduction of the colour reagents, containing 500 μL of 5 % iron sulphate and 1 % ammonium molybdate (Acros Organics, Loughborough, UK), and each sample was measured at 690 nm. All phosphate, pyrophosphate and ALP solutions were made in a 100 mM tris-HCL buffer. Possible

interference by phosphate release from the matrix was accounted for by measuring the phosphate concentration of the eluent in the absence of ALP.

9.2.4 Determination of kinetic parameters

HRP undergoes a two substrate reaction (Reduced ABTS + H_2O_2 → Oxidized ABTS + $2H_2O$). In this study, it was assumed that 10 nM of HRP catalyses one substrate reaction (ABTS) varied from 5.37 µM to 50 µM by fixing the constant concentration of 9.79 µM of the other substrate, H_2O_2.

9.3 Results

9.3.1 The effect of encapsulated enzymes on the chemical structures of CHA cryogels

After freeze drying, the resulting CHA cryogels were shown to consist of a combination of apatite, as evidenced by a characteristic peak at 26˚, and 32˚ 2θ (Figure 9.1), and calcite with peaks at 23˚, 29˚, 39˚, 47˚, 49˚, and 53˚ 2θ. The broadness of the peaks indicative of apatite suggested the formation of a poorly crystalline phase. The incorporation of either ALP or HRP into the CHA cryogels had no effect on the crystalline composition of the material (Figure 9.1).

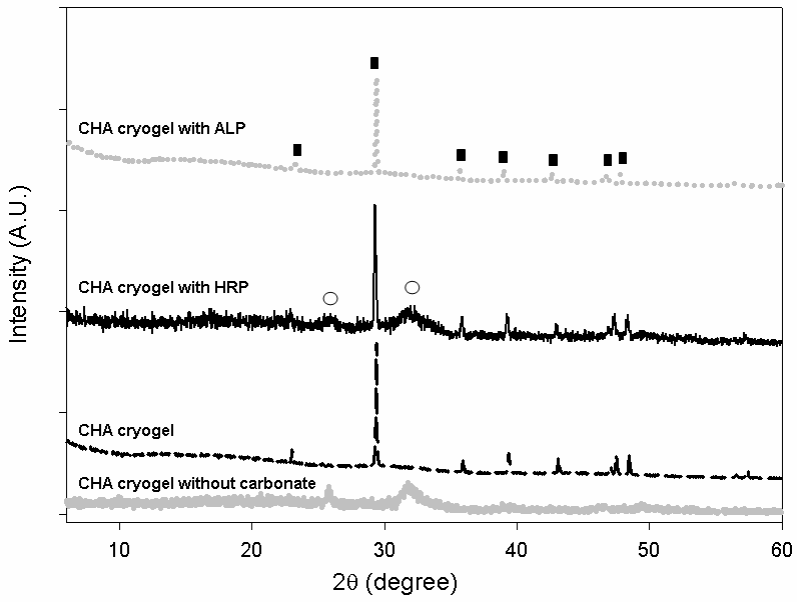

Figure 9.1 X-ray diffraction patterns showing the influence of ALP or HRP addition on the crystalline compositions of the CHA cryogels and the addition of carbonate. The open circle (○) labels as apatite; the square (■) labels as calcite.

FTIR spectra of the samples further confirmed that the incorporation of ALP or HRP into the ceramic matrix did not affect the composition of the material. Peaks present at 863, 1415, and 1479 cm^{-1} were indicative of the ν2 and ν3 vibrations of carbonate ions. The presence of these vibrations could indicate either the presence of carbonate substitution of the apatite lattice or simply the presence of $CaCO_3$ in the sample. As expected, there were also peaks present at 561 and 1031 cm^{-1}, which were indicative of PO_4^{3-} vibrations (Figure 9.2).

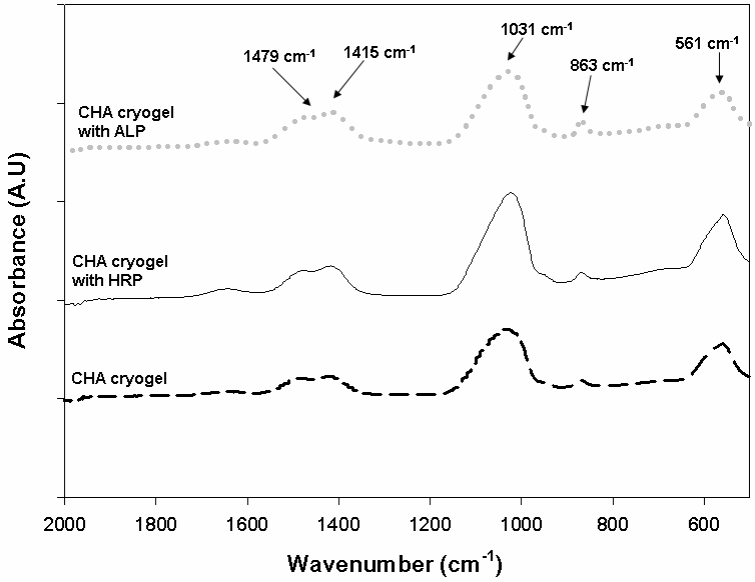

Figure 9.2 FTIR spectra of the CHA cryogels, with and without the addition of ALP or HRP. The addition of either enzyme to the material during processing had little or no influence on the final composition of the material.

9.3.2 The effect of encapsulated enzymes on the microstructures of apatite cryogels

Although the addition of ALP and HRP to the CHA cryogels had little influence on the true density of the material (Table 9.1), each true density was significantly lower (2.3 to 2.6 g cm^{-3}) than would be expected for calcite (2.71 g cm^{-3}) or apatite (3.16 g cm^{-3}). This may suggest the presence of an X-ray amorphous phase of lower true density than either of these minerals. The incorporation of the enzymes into the CHA cryogels resulted in a slight difference in the specific surface area exhibited by the gel material. The control material exhibited a specific surface area of 48.33 ± 4.60 m^2 g^{-1}, whereas the CHA cryogel formed in the presence of HRP exhibited a specific surface area of 53.12 ± 1.48 m^2 g^{-1} (Table 9.1), the specific surface area of the CHA cryogel containing ALP was lower than either of other materials (42.62 ± 1.55 m^2g^{-1}); although this difference could be attributed to variations between different batches of the materials.

Table 9.1 The true density, specific surface areas and particle sizes exhibited by the apatite from which the CHA cryogel was formed following precipitation in the absence of enzymes, in the presence of HRP and in the presence of ALP.

Sample	True Density ($g\ cm^{-3}$)	Specific surface area ($m^2\ g^{-1}$)	Mean Particle Size (nm)
CHA cryogel	2.35 ±0.02	48.33 ± 4.60	536 ± 124
CHA cryogel with HRP	2.53 ±0.03	53.12 ± 1.48	618 ± 17
CHA cryogel with ALP	2.59 ± 0.19	42.62 ± 1.55	436 ± 97

The crystallite size was shown to be significantly smaller than the particle size of the precipitate, which consisted of blade-like crystals of approximately 100-150 nm in length and 20-30 nm in width (Figure 9.3A). Examination of the surface of the CHA cryogel illustrated the presence of very few surface features as may be expected for a mesoporous cryogel material (Figure 9.3B).

The incorporation of the enzymes into the CHA cryogel matrix also resulted in a reduction in the total porosity of the final material from 81 ± 6 % for the control CHA cryogel to 37 ± 28 % for the CHA cryogel containing HRP (Table 9.2), but a slight increase in the case of the ALP loaded material (88 ± 2 %). The reduction in the porosity that was exhibited by the CHA cryogel was accompanied by a reduction in the median pore diameter exhibited by the material from 36 ± 20 nm, in the case of the control material, to 11 ± 1 nm following the addition of HRP to the material during processing (Table 9.2). The high standard deviation of the median pore diameter of the CHA cryogel (36 ± 20 nm) might result from the irregularly geometric structure of cryogels. However, the pores were mainly distributed in the range of 10 to 100 nm, which has not changed after the incorporation of ALP (Figure 9.4). In the case of HRP, numbers of pores with

size between 70 and 20 nm were increased, in comparison to the blank CHA cryogel (Figure 9.4). The addition of ALP to the CHA cryogel resulted in an increase in the median pore diameter of the material to 56 ± 21 nm. The particle size of the CHA cryogel with and without enzymes was in the order of 400-600 nm in all processing conditions (Table 9.1). Interestingly, the CHA cryogel after loading these two enzymes had increased its size for encapsulation of HRP, but decreased for incorporation of ALP. As the total intrusion volume of mercury increased, the porosity of CHA cryogel with/without enzymes also was increased (Table 9.2).

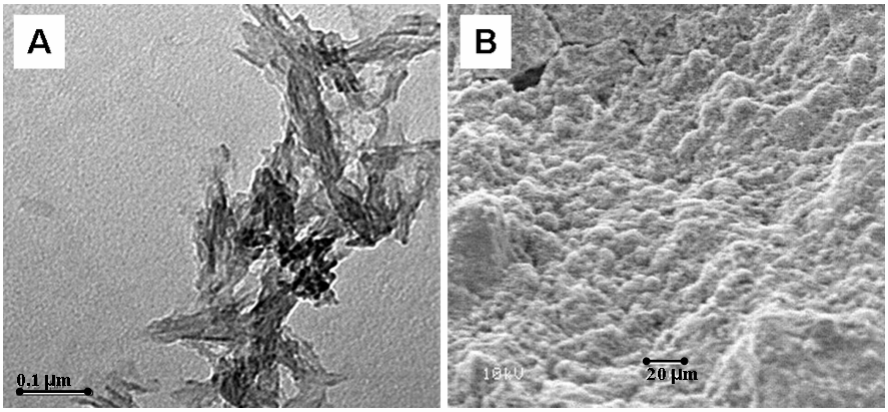

Figure 9.3 Electron micrographs showing A. the morphology of apatite crystallites dispersed in water prior to gel formation and B. the surface of a CHA cryogel following processing.

Table 9.2 The influence of protein addition on the microstructure of the CHA cryogels, including the total intrusion volume, porosity, and median pore diameter.

Sample	Total Intrusion Volume ($cm^3\ g^{-1}$)	Porosity (%)	Median Pore Diameter (nm)
CHA cryogel	2.20 ± 0.93	81 ± 6	36.2 ± 19.7
CHA cryogel with HRP	0.40 ± 0.16	37 ± 28	11.3 ± 0.8
CHA cryogel with ALP	3.13 ± 0.39	88 ± 2	55.7 ± 20.5

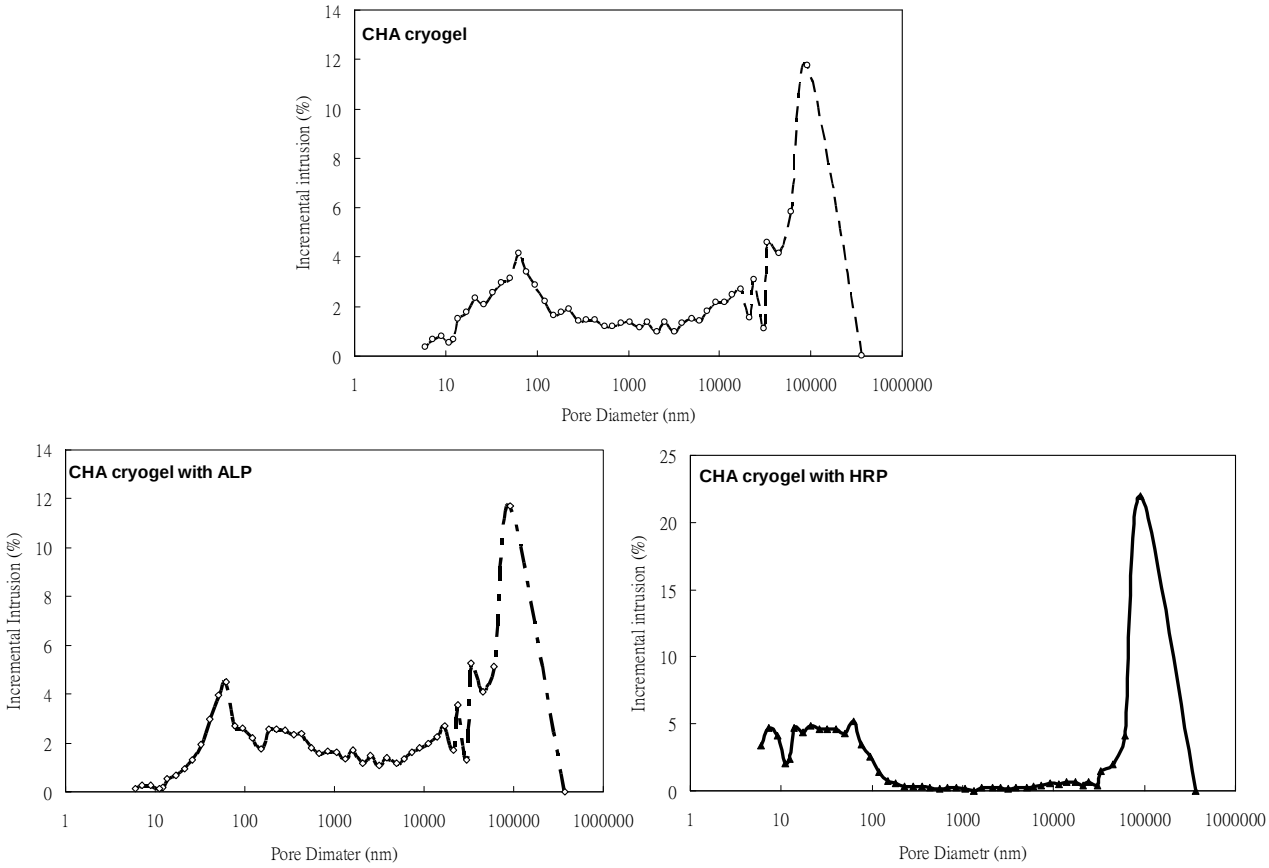

Figure 9.4 Mercury intrusion of the CHA cryogel with/without enzymes. The pores of the CHA cryogel matrix were distributed in the range of 10 to 100 nm. The pore distribution of the CHA cryogel has not been changed after incorporation of ALP. However, there was a slightly alteration of the CHA cryogel with HRP.

9.3.3 Storage efficacy of Horseradish Peroxidase/ Alkaline phosphatase *in vitro* study

Once immersed in the elution medium, there was a burst release of HRP with 36 wt% of the enzyme released from the ceramic matrix within one day (Figure 9.5). After one day of ageing, the rate of release from the matrix slowed so that over a period of eight days of ageing only a further 8 wt% of the HRP was released into solution. In contrast, there was only a small release of ALP during the first day of ageing (10 wt%), with only 15 wt% of the ALP being released over a period of 10 days in solution (Figure 9.5).

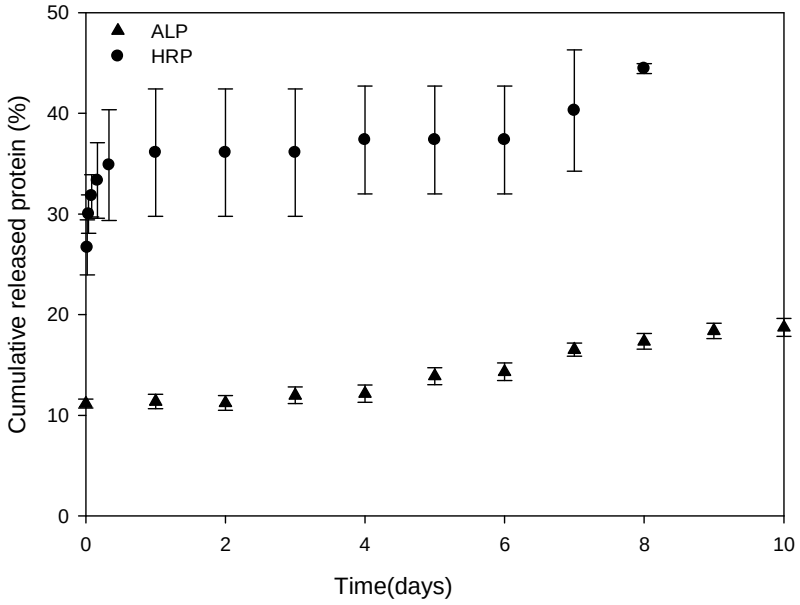

Figure 9.5 The release of ALP or HRP from the CHA cryogel over a period of ten days of ageing. There was an initial burst release of HRP from the matrix, followed by a plateau, whereas in the case of the ALP, after the first day of ageing, there was little further release from the gel matrix.

The activities of the encapsulated enzymes were evaluated over a period of 14 days of ageing. In the case of the HRP, activity was expressed in terms of the rate of $ABTS^+$ production per minute. When free in solution, the rate of conversion of the ABTS to $ABTS^+$ varied little and after 14 days of ageing, the HRP exhibited a rate of $ABTS^+$ production of 1.2 μM/min (Figure 9.6). The production of $ABTS^+$ catalysed by the encapsulated HRP was reduced initially from 0.8 to 0.1 μM/min after 2 days as shown in the Figure 9.6. This reduction corresponded with the rapid release of the surface bound enzyme. After this time point, the $ABTS^+$ was produced at the rate of 0.22 μM/min. To investigate whether this reduction in activity could be attributed to mass transport limitations imposed by the presence of the gel, following 14 days of ageing the gel was crushed and the HRP released by dissolving the CHA cryogel into Na_4-EDTA, and

quantified by the BCA assay. After release from the gel, the rate of $ABTS^{+}$ production increased to 0.8 μM/min.

The activity of ALP was assessed by the hydrolysis of pyrophosphate ions and was expressed as μM/min (Figure 9.6). The rate of phosphate production was higher at all time points for the encapsulated ALP than for the ALP that was free in solution. In the case of the free ALP, the rate of phosphate production could not be measured following 6 days of ageing. In comparison, phosphate production could be measured for a period of 12 days following encapsulation. All reported data were zeroed against the amount of phosphate eluted into the ageing medium in the absence of the ALP.

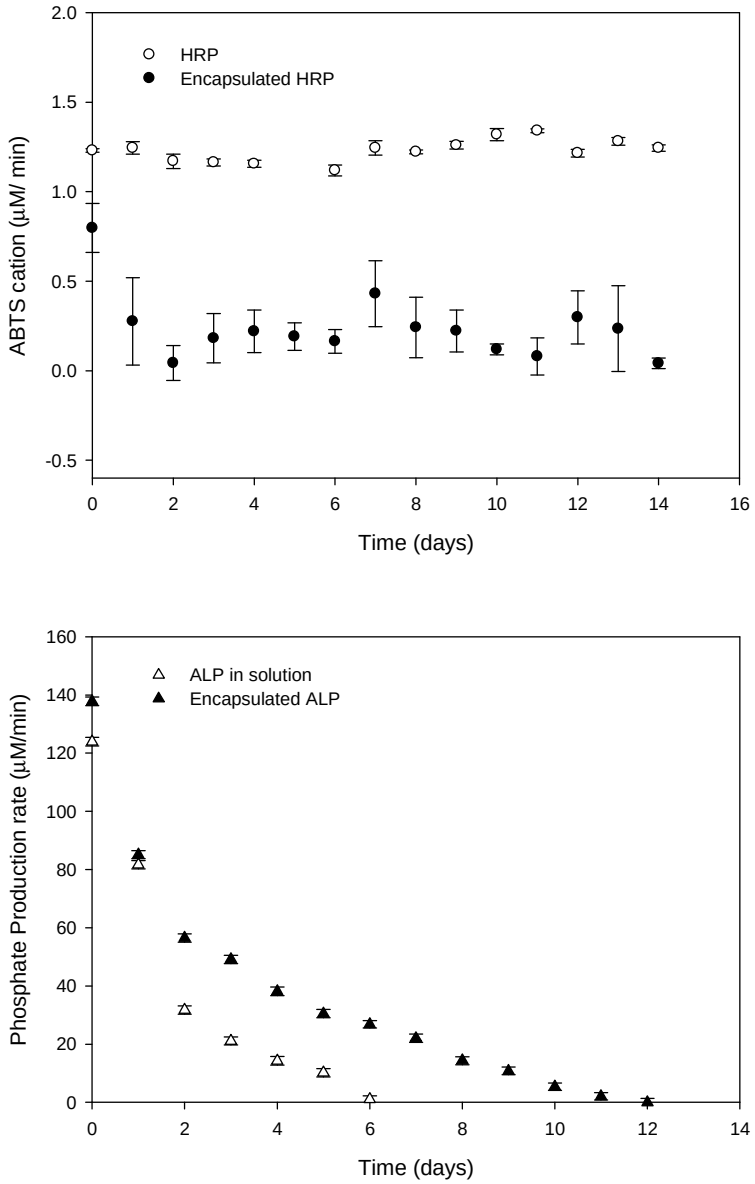

Figure 9.6 The activity of HRP expressed as the rate of production of $ABTS^+$ with time. HRP was free in solution and encapsulated within the CHA cryogel matrix. The pyrophosphatase activity of the encapsulated and un-encapsulated ALP was measured over a period of twelve days of ageing. Encapsulation significantly reduced the rate of $ABTS^+$ production, when compared with the HRP free in solution but encapsulation was shown not to have a detrimental influence on the rate of phosphate production and also seemed to prolong the period of time during which the activity of the enzyme was measurable.

9.3.4 The kinetic behaviour of free enzymes and encapsulated enzymes

The K_m of free HRP was respectively 15.32 μM for the Michaelis-Menten equation and 8.48 μM for the Lineweaver-Burk equation. The V_m of free HRP (0.58 μM/min) by the Michaelis-Menten equation was 1.3 times as much as the V_m of the Lineweaver-Burk equation (0.45 μM/min) (Table 9.3). Compared with the HRP, the release of ALP fitted the Michaelis-Menten equation and the Lineweaver-Burk equation according to the R^2 (0.98). The affinity of enzyme to substrate can be evaluated by the value of K_m, as the higher K_m the lower affinity whereas the lower K_m the higher affinity. The kinetic parameters of HRP encapsulated into apatite cryogels did not fit either of the kinetic equations as Table 9.4 indicates, R^2 being very low.

Table 9.3 The kinetic parameters of free HRP/ALP in the buffer solution.

Enzyme	Michaelis-Menten			Lineweaver-Burk		
	K_m	V_m	R^2	K_m	V_m	R^2
HRP[a]	15.32	0.58	0.86	8.48	0.45	0.89
ALP[b]	2.32	0.12	0.98	3.22	0.14	0.98

a: The unit of Km is μM and of Vm is μM/min. b: The unit of Km is mM and of Vm is mM/min.

Table 9.4 The kinetic parameters of encapsulated HRP in the buffer solution. The unit of K_m is μM and of V_m is μM/min.

Enzyme	Michaelis-Menten			Lineweaver-Burk		
	K_m	V_m	R^2	K_m	V_m	R^2
CHA cryogel with HRP	12.79	2.58	0.17	7.49	1.58	0.31

9.4 Discussion

9.4.1 Encapsulation of Alkaline phosphatase in sol-gel bioceramics

The first successful encapsulation of a functional enzyme was reported by Braun et al. [Braun et al. (1990)]. The potential for this system to act as a molecular biosensor was well recognised and consequently there have since been numerous reports of silica gels being used to entrap enzymes such as HRP and ALP, as well as a host of other proteins [Kadnikova and Kostić (2002), Frenkel-Mullerad and Avnir (2005), Nicoll et al. (1997)]. While silica gels have numerous advantages over other encapsulation technologies, such as their chemical inertness and ease of synthesis in ambient conditions, the use of TMOS/TEOS in their fabrication leads to the formation of methanol or ethanol, which can compromise enzyme activity. Indeed, previous work has shown that when incorporated into CHA layers on 45S5 bioactive glasses, the enzymes exhibited comparatively low activities and when encapsulated within silica gel layers, activity was completely lost [Lobel and Hench (1998)].

Since they are well tolerated *in vivo* and can form an intimate bond with both hard and soft tissues, CaP based ceramics such as HA, β-TCP, and biphasic calcium phosphate are widely used for the replacement of hard tissues. Numerous researchers have investigated the efficacy of these materials for the delivery of therapeutic molecules such as vancomycin, ibuprofen-lysine and indomethacin [Palazzo et al. (2005), Xu et al. (2007), Gbureck et al. (2008)]. Few studies, however, have investigated the ability of HA to encapsulate enzymes.

There has recently been significant interest surrounding the immobilisation of ALP onto polymeric materials [Filmon et al. (2002)]. This work has been inspired by the increased

understanding of the role of ALP in bone formation. ALP is found throughout the body in five different isoenzymes (intestinal, kidney, placental, tissue non-specific, germ cell). TNAP is present in high concentrations on the surface of the cells responsible for depositing new bone matrix (osteoblasts) and in the matrix vesicles from which apatite crystals are deposited [Hessle et al. (2002)]. Its function in bone mineralisation is to remove an inhibitor to HA precipitation ($P_2O_7^{4-}$) to form PO_4^{3-} resulting in localised supersaturation and therefore precipitation [Osathanon et al. (2009)]. It has also recently been shown that TNAP can act on amorphous calcium polyphosphate particles [Omelon et al. (2004)], which have been found in newly mineralising tissue and are thought to provide 'phosphate reservoirs' to enable new bone formation. By locally increasing ALP concentration in an implant, therefore, it may be possible to reduce the local $P_2O_7^{4-}$ to PO_4^{3-} ratio and thereby stimulate new bone deposition. This effect has been shown to be effective *in vitro* by enhancing the extent of mineralisation in osteoblast cultures [Osathanon et al. (2009)].

9.4.2 The effect of porous structures on the storage of ALP/HRP

While some success has been noted, surface immobilisation of ALP can result in the interference of enzyme function through interaction with the plethora of other proteins and enzymes found in the body [Boyan et al. (1996)]. The mesoporous apatite gel reported here enables immobilisation and subsequent protection from other macromolecules.

The encapsulation of both proteins within the CHA cryogel seemed to have an influence on the microstructure of the gel. While the incorporation of HRP into the CHA cryogel matrix reduced the median pore diameter of the matrix by half, the addition of ALP

during processing increased the median pore diameter to 55.7 nm (Table 9.2). This change in microstructure could most likely be attributed to the incorporation of a significantly higher mass of ALP into the CHA cryogel than HRP, due to the lower activity of the ALP when compared with the HRP. The fluctuations in the specific surface area exhibited by the CHA cryogel could also be attributed to the use of relatively high masses of ALP. Importantly, although the ALP altered the pore size distributions exhibited by the material, this did not detrimentally affect the ability of the CHA cryogel to store the enzyme. The addition of both proteins to the CHA cryogel during processing did not seem to influence the chemistry of the material. Interestingly, however, the true densities exhibited by the gels were considerably lower than one might expect for gels consisting predominantly of apatite (ρ=3.16 g cm^{-3}) and $CaCO_3$ (ρ=2.71 g cm^{-3}) (Table 9.1). This may suggest the presence of an amorphous phase that was undetectable by X-ray diffraction. It is possible that a metastable calcium phosphate phase of relatively low density such as brushite (ρ=2.32 g cm^{-3}) was formed in the matrix during processing.

Over the period of study, the CHA cryogel was shown to retain 85 wt% of the loaded ALP (Figure 9.5), which was comparable with the reported loading efficiency of gels loaded using non-surfactant template sol-gel processes [Wei et al. (2000)]. Furthermore, encapsulation of the ALP enhanced the stability of the enzyme when compared with that left free in solution. While the CHA cryogel encapsulated and preserved the activity of the ALP, such success was not demonstrated for encapsulation of the HRP (Figures 9.5 and 9.6). In comparison, the CHA cryogel encapsulated the HRP with a relatively low efficacy (66 wt%) and the activity of the encapsulated enzyme was significantly diminished when compared with that stored free in solution. Up to one day after encapsulation, the activity of the HRP was considerably higher than at any additional

time-point. The relatively high activity at this point could be attributed to surface adsorbed HRP and the HRP that was released in a burst from the matrix on the first day. After this point, the activity of the enzyme was considerably reduced. The most likely reason for the reduction in activity on encapsulation could be poor mass transport through the mesoporous pore network in the cryogel, hindering the access of the substrate to the enzyme's active site [Bhatia et al. (2002), Silva et al. (2007), Jain et al. (1998)]. This hypothesis was confirmed by the increase in $ABTS^{+}$ production once released from the ceramic matrix at the end of the study.

The activity of the ALP may not have been influenced by the mesoporous pore network since the substrate of the reaction, the pyrophosphate anion (Mr=174 g/mole), is significantly smaller than ABTS (Mr=514.62 g/mole). Furthermore, the pyrophosphate anion [Fleisch.and Bisaz (1962)] is well known to have a high affinity to CaP salts and therefore is likely to exhibit more rapid perfusion of the CHA cryogel and to attach strongly to the surface of the apatite. Charge may also have played a role in preventing mass transport of the $ABTS^{+}$ through the CaP based matrix. The positive charge exhibited by the surface of the CaP may have prevented permeation of the transport of the $ABTS^{+}$ through the matrix. Indeed, electrostatic repulsion has previously been shown to have a significant influence on the catalytic efficacy of HRP [Kadnikova and Kostić (2002)]. Besides the material itself, the pH and other ions of the buffer solution play an important part in the electrostatic repulsion. Therefore, this might contribute to the unsteady state kinetics of free HRP. As a result of unsteady state, the free HRP may not follow either of the kinetic equations (Table 9.3). After the incorporation of HRP, the pore structure of the cryogel has been changed, suggesting the complicated diffusion behaviour. This results in the poor fitting of the kinetic equations (Table 9.4).

9.5 Conclusion

This study reports the successful encapsulation of ALP within a CaP based gel matrix. The CHA cryogel immobilised 85 wt% of the ALP for the duration of the experiment and preserved enzyme activity when compared with the ALP that was free in solution. Evaluation of the CHA cryogel structure demonstrated that the material consisted in the most part of apatite and calcium carbonate with the presence of a comparatively low density phase that was undetectable using X-ray diffraction.

Chapter 10 Surface modification of calcium phosphate gels using sulphhydryl groups

10.1 Introduction

Calcium phosphate composites have been used widely as implant materials due to the non-toxicity of their ionic components and the intimate bond that they are able to form a range of bonds with hard and soft tissue. More recently, calcium phosphate particles have also been used in the transfection of cell for gene therapy [Kovtun et al. (2009), Maitra (2005)]. With an increasing understanding of the interaction between CaP materials and biological systems there is an interest in modifying the surface chemistry of these materials to change biological interaction or prevent the agglomeration of CaP particles in solutions. The attachment of biomolecules such as protein to the surface of the CaP materials is of particular interest. Recently, the biological properties of calcium phosphate bone cement following modification with heparin have been improved [Lode et al. (2008)]. Reactive thiol groups have been used to attach polymers to implant surfaces for enhanced biological integration of bone implants [Lee et al. (2007)]. One way of attaching proteins to the surface of CaP materials is through the creation of disulphide bridges between thiol groups of the surfaces and the cysteine residuals of the proteins [Wright et al. (2006)].

Due to the lack of functional groups of hydroxyapatite (HA), a chemical reaction is used to derive amino groups or sulphhydryl groups on the surface of the HA. It has been reported that HA can be functionalised by a reaction of the OH group of HA with carboxyl containing SH chemicals [Lee et al. (2007)]. However, conclusive evidence of the presence of SH groups on the surface of modified HA has been scarce. The most common modification uses silanisation [Duan and Wang (2006)]. Amongst many

organosilanes, the amino-terminated, and the thiol-terminated are of particular interest. Previous work has demonstrated that the adhesion of osteoblast is increased when HA is functionalised with 3-aminopropyltriethoxysilane [Nelson et al. (2006)]. Although much attention has been given to the use of mercaptopropyltriethoxysilane (MPTS) for the surface modification of silicon oxide [Nakamura and Ishimura (2007)], there is scarcely any research on the surface modification of HA with MPTS.

The main objective of this work has been to develop a technique for the surface modification of calcium phosphate gels. Two thiol-containing chemicals were used to modify the surface features of calcium phosphate gels and their efficiency was evaluated.

10.2 Surface modification of calcium phosphate gels

To enhance the bonding power of calcium phosphate gels, their surfaces were modified by introducing thiol groups. As sulphhydryl groups are important in biological systems, sulphhydryl-containing chemicals were selected to functionalise the surfaces. Two chemicals were chosen in this study: mercaptopropionic acid, and mercaptopropyl silane.

10.2.1 Preparation of silicon substituted hydroxyapatite (SiHA)

The method of silicon substituted hydroxyapatite preparation was adapted from previous work [Palard et al. (2008)]. 100 mL of 130 mM triammonium phosphate containing 43 mM silicon tetra-acetate (Sigma-Aldrich, Gillingham, UK) was poured into a 100 mL burette, and added at the rate of 830 μL min^{-1} to a 100 mL of 210 mM calcium acetate solution with pH 12. The pH value of the 210 mM calcium acetate solution was adjusted by the addition of 35 % aqueous ammonia. After the addition of the triammonium and silicon tetraacetate solution, the mixture was washed five times with double distilled

water (DDW) by a centrifuge at 4000 rpm for 10 minute. The suspension was then adjusted to pH 7.4 by the addition of 100 mM hydrochloric acid solution, and then filtered through Whatman No. 1 filter paper in a Büchner funnel, connected to a water aspirated vacuum pump. The SiHA xerogel was dried at room temperature as shown in Figure 7.1.

10.2.2 Surface modification of hydroxyapatite with 3-mercaptopropionic acid

The surface modification method was adapted from Lee et al. (2007). 130 mM triammonium phosphate and 47 mM 3-mercaptopropionic acid (MPA) (Sigma-Aldrich, Gillingham, UK) was added to a 210 mM calcium acetate solution with pH 12 at equal volume. The resulting HA xerogels modified with thiol groups were washed five times with double distilled water (DDW) by a centrifuge. The pH of the suspension was then adjusted to pH 7.4 by the addition of 100 mM hydrochloric acid solution. The suspension was filtered through Whatman No. 1 filter paper in a Büchner funnel. Then, the HA xerogels with sulphhydryl groups were dried at the room temperature. The reaction mechanism of MPA is shown in Fgure 10.1 A.

10.2.3 Surface modification of silicon substituted hydroxyapatite with 3-mercatopropyl trimethoxysilane

1 g of SiHA xerogel formed as described in section 10.2.1 with 100 mL of 43 mM 3-mercatopropyl trimethoxysilane (MPTS) in ethanol (Fisher scientific, Loughborough, UK) was placed in an Atmos Bag (Sigma-Aldrich, Gillingham, UK) and was given 1 h at room temperature to react. The precipitate was washed firstly with ethanol and then four times with double distilled water. The suspension was filtered through Whatman No. 1 filter paper in a Büchner funnel to form SiHA xerogels, containing thiol groups, and then

dried at room temperature. The modification of SiHA xerogels with MPTS is expressed as the reaction mechanism shown in Figure 10.1 B.

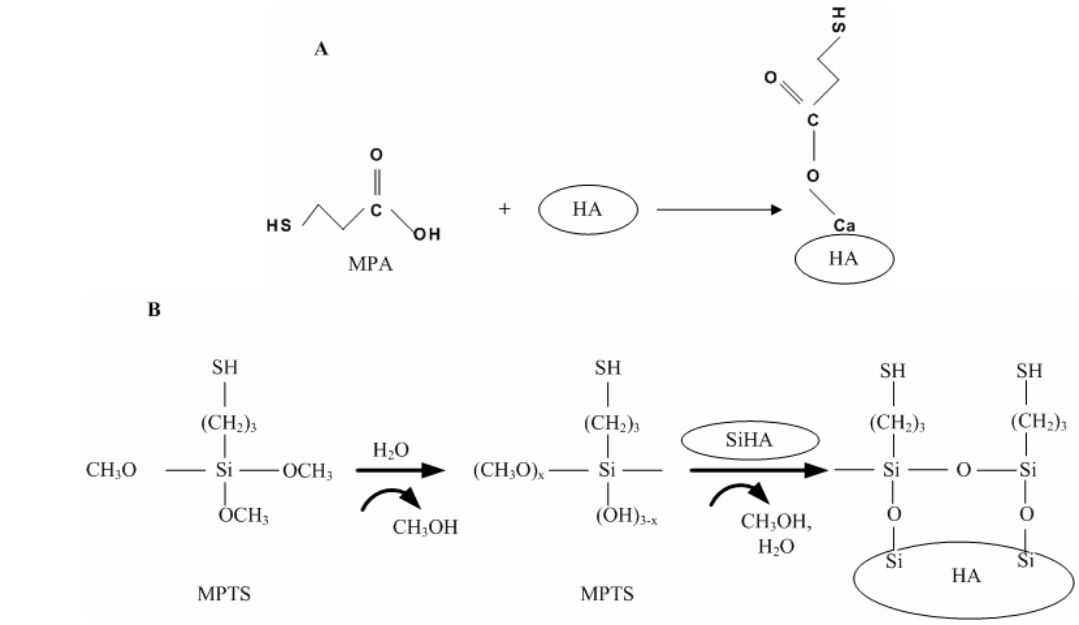

Figure 10.1 The scheme of A. the modification of SiHA xerogels with MPA; B. modification of SiHA xerogels with MPTS. MPTS is hydrolysed following the attachment to SiHA xerogels.

10.2.4 Preparation of fluorescence staining surface modified SiHA xerogels with sulphhydryl particles

SiHA sulphhydryl modified gel particles were tagged fluorescently using a maleimide reaction, which was adapted from the method described by Nakamura and Ishimura (2007). 33 mg of SiHA xerogel with sulphhydryl was added to 10 μL of 2.3 mM fluorescein-5-maleimide (Invitrogen, Paisley, UK) solution for 2 h at room temperature with 500 rpm mixing rate. After 2 h, the mixture was centrifuged to remove the remaining reagents, using a 2 mL Eppendorf centrifuge (Fisher Scientific, Loughborough, UK). The xerogels were washed with ethanol and distilled water until the fluorescein was not observed under the fluorescence microscopy. The control SiHA xerogels were prepared under the same conditions to investigate whether there was a reaction between the SiHA xerogels and the fluorescein.

10.2.5 Quantification of sulphhydryl groups on CaP surfaces

The sulphhydryl groups on the HA/SiHA xerogels were quantified using Ellman's reagent. 10 mg of HA with sulphhydryl groups was put into 780 µL of phosphate buffer saline with a pH of 7.4. Then 15 µL of DTNB reagent (0.4 %w/v) was added to this suspension [Lee et al. (2007)]. This mixture was incubated for 15 min at room temperature at 3000 rpm of mixing. The supernatant was obtained using centrifuge at 4000 rpm for 15 min and analysed by UV-Vis spectroscopy at 412 nm. The sulphhydryl groups attached on the surface of the HA/SiHA xerogels were calculated on the basis of the molar extinction coefficient (14150 $M^{-1}cm^{-1}$), and the known equation shown as Equation 10.1.

$$n = a \times N \times [d \times \frac{4}{3} \pi r^3] \qquad \text{Equation 10.1}$$

where n is amount of sulphhydryl per crystal, a is the mol of SH on HA/SiHA per g, d is the density of HA/SiHA (3.15 g cm^{-3}), r is the radius of the HA/SiHA on the assumption of sphere HA/SiHA xerogel particles, and N is Avogadro's number (6.022×10^{23} mol^{-1}).

10.3 Results

10.3.1 Characterisation of HA with thiol groups

The apatitic phases of HA xerogels with MPA occurred at 26˚, and 32˚ 2θ. In addition, there was a trace amount of calcite shown in the range of 40˚ to 52˚ 2θ in HA xerogels modified with MPA (Figure 10.2). As compared to those of the unmodified HA xerogels, the crystalline phase and structure of HA xerogels with MPA remained unchanged. In addition, the broad peaks indicated that the apatite phase was poorly crystallne.

Modification with MPA can be assessed through the C=O bonding at ~1700 cm^{-1}, and C-H bonding between 2850 and 3000 cm^{-1} using FTIR analysis. The FTIR spectra (Figure 10.3) showed phosphate absorption of HA xerogels in the ranges 870 cm^{-1} to 1030 cm^{-1}, and 570 to 607 cm^{-1}. There were peaks at 1644, and 3280 cm^{-1} in unmodified HA xerogels and modified HA xerogels. However, the intensity of peaks at 1644, and 3280 cm^{-1}, respectively, were slightly increased in the HA xerogels modified with MPA as compared with the unmodified HA xerogels.

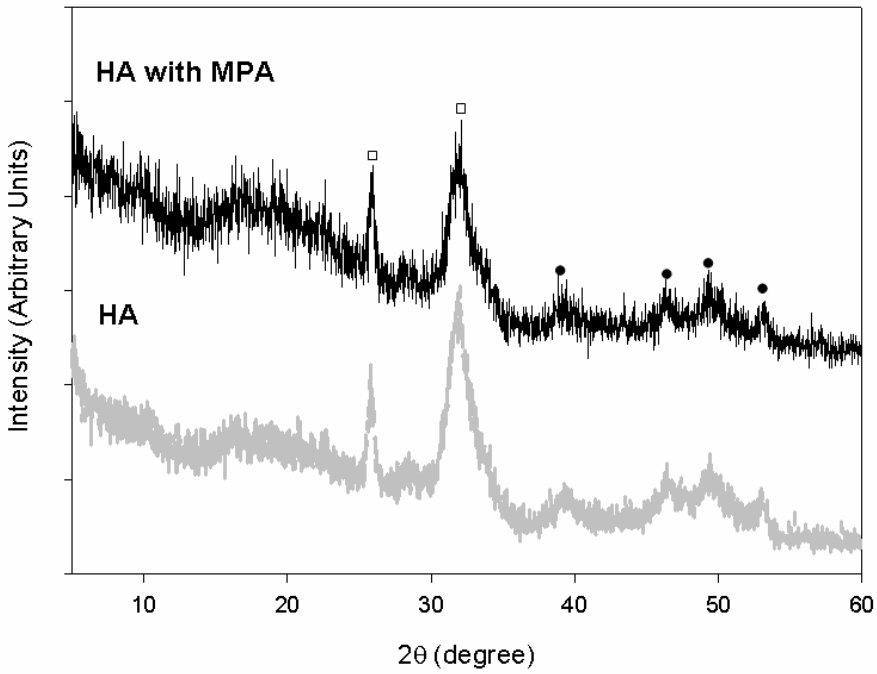

Figure 10.2 XRD patterns of the HA xerogels and the modified HA xerogels with MPA. The peaks of apatite phase were present at 26˚, and 32˚ 2θ labelled as square (□); a few calcites were shown at 40˚ to 52˚ 2θ labelled as circles (●).

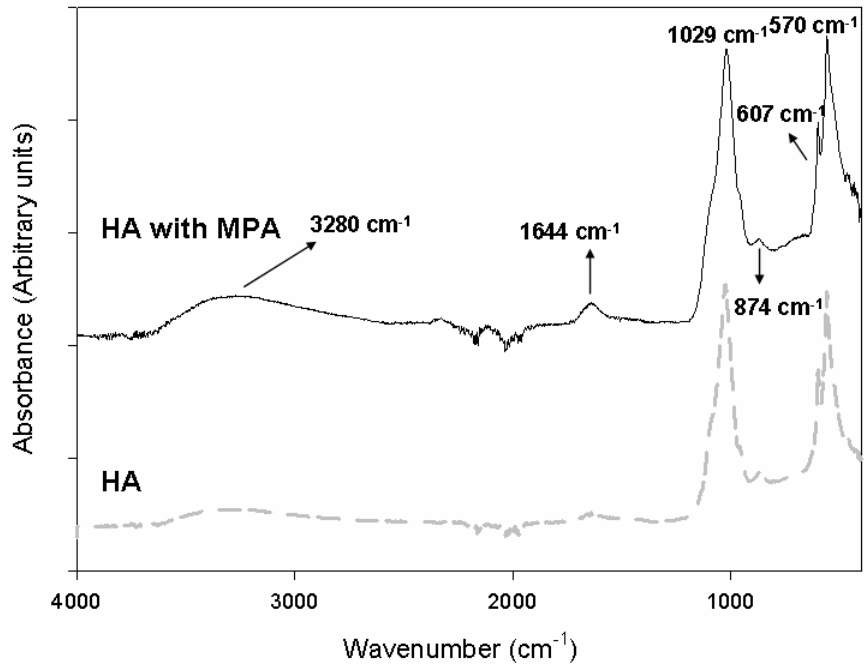

Figure 10.3 FTIR spectra of the unmodified HA xerogels and the HA xerogels modified with MPA. Phosphate groups (870 to 1030 cm^{-1}, and 550 to 610 cm^{-1}) were predominantly present in the both of the HA xerogel matrices. In addition, there were trace of carbonate from surface absorption (874 cm^{-1}), and moisture in the both of the HA xerogel matrices (3280 cm^{-1}).

To verify the presence of the sulphur atoms on the surface of the precipitate, XPS analysis was carried out. The XPS spectra (Figure 10.4) showed a calcium (2s) peak at 437.8 eV, phosphate peak (2p3) at 130.1 eV and an oxygen peak at 530.5 eV in both of the HA xerogel without, and with modification. In addition, the calcium peaks at 347.1 eV resulted from the Ca-O bonding of calcite which corresponds to the result of XRD pattern. In comparison with the HA xerogels, the HA xerogels with MPA showed carbonate peaks from C=O of MPA at 287 eV rather than C1s (285 eV). However, there was no S2p peak of the S-H bond at the binding energy of 163.3 eV of the HA xerogels with MPA.

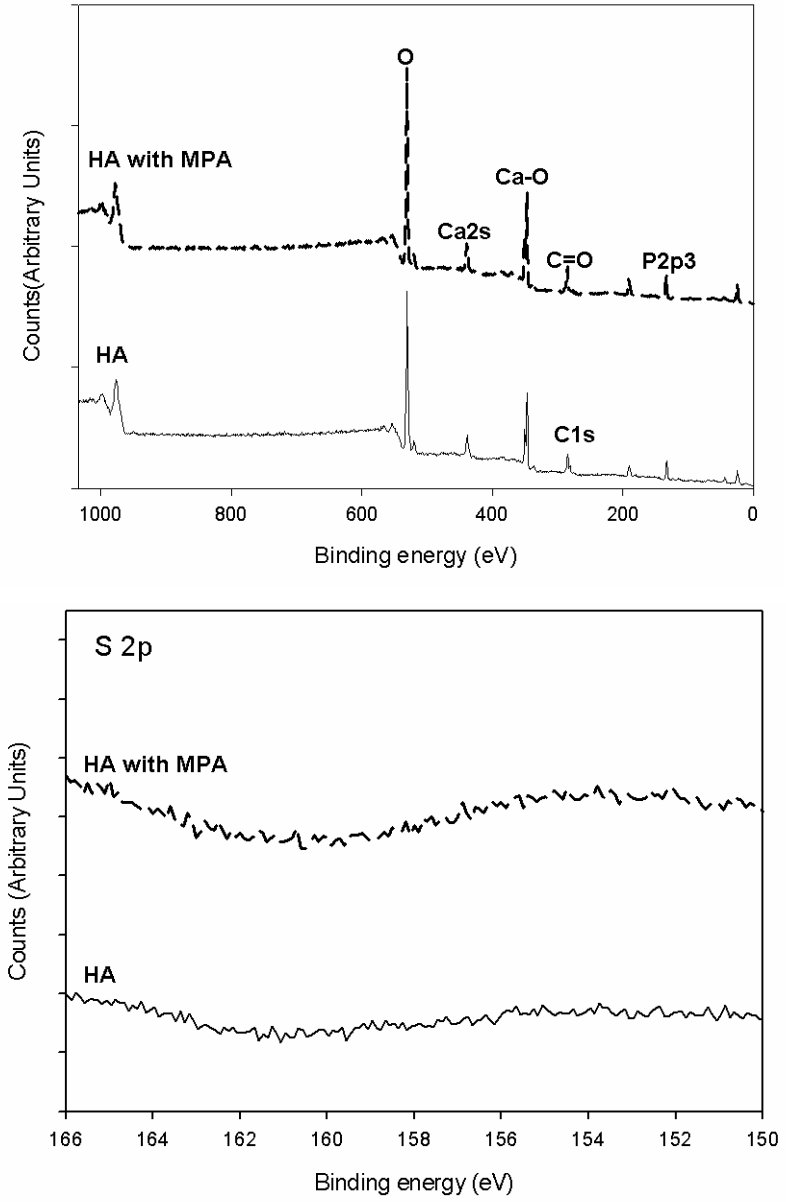

Figure 10.4 The XPS wide scan spectra of surface modification of the HA xerogels and the HA xerogel with MPA; and the elemental region of S narrowly scanned to provide high resolution. Not only calcium phosphate peaks of HA were exhibited but also few Ca-O peaks of calcite in the HA xerogel and the modified HA xerogel. No sulphur peaks appeared in the modified HA xerogel with MPA.

In addition to the XPS survey, the presence of sulphur was determined using EDS, XRF, and Ellman's reagent (Table 10.1). There no S signal showed in the EDS but the result of XRF by contrast, indicated 0.02 wt% of S in the HA xerogels with MPA, corresponding to Ellman's analysis. The Ca/P ratio from the EDS (1.60) was in accordance with that of XRF (1.62).

The other evidence of the sulphur can be evaluated through the alternative of particle characterisation. The true density of the HA xerogel with MPA (2.70 g cm^{-3}, Table 10.2) was not far from that of the unmodified HA gel (2.62 g cm^{-3}, Table 7.3). Although the mean particle size of HA xerogels with MPA was not much different from that of the pure MPA (Table 10.2), the number of particles of the HA xerogel with MPA distributed in the range of 300 to 400 nm increased (Figure 10.5 (a)-(b)). In comparison with the HA xerogel without the modification (ab. 565 nm), the mean particle size of the HA xerogel with MPA decreased which suggests the aggleromation of HA gel particles was reduced. The specific surface area of the HA xerogel with MPA (Table 10.2) was less than half times of the HA xerogel (98.0 ± 4.6 m^2 g^{-1}).

Table 10.1 Quantification of thiol groups on HA xerogel particles using EDS, XRF, and Ellman's reagent [one measurement].

Elemental analysis	Ca weight %	P weight %	S weight %	Other weight %	Ca/P mole ratio
EDS	35.55	17.19	0	47.26	1.60
XRF	32.96	15.73	0.02	50.29	1.62
Ellman's reagent	-	-	3.82E-05	-	-

Table 10.2 The physicochemical characterisation of pure MPA, and of HA xerogels with MPA

Samples	True Density (g cm^{-3})	Mean Particle Size (nm)	Specific surface area (m^2 g^{-1})
Pure MPA	-	313.0 ± 11.8	-
HA xerogels with MPA	2.70±0.01	316.7 ± 14.0	39.3 ± 13.1

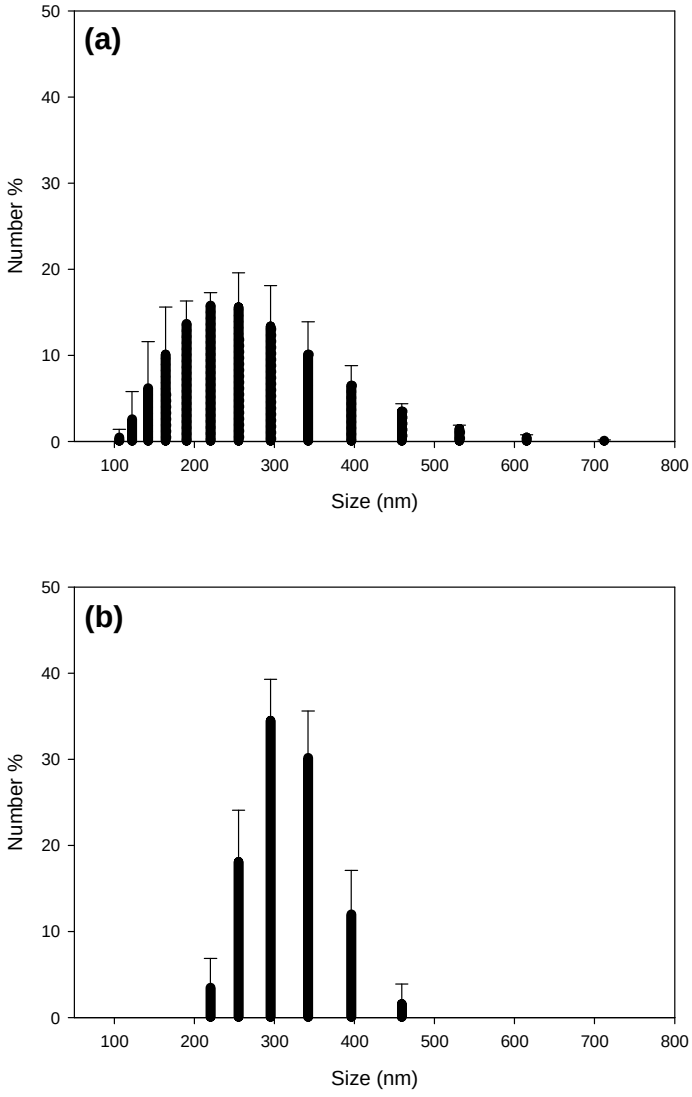

Figure 10.5 Particle size distribution of (a) pure MPA; (b) HA xerogels with MPA. There was an obvious increased in the number of particles in the range of 300 to 400 nm after the surface of HA xerogels was modified with MPA.

10.3.2 Characterisation of SiHA with thiol groups

The XRD patterns for the SiHA xerogels with and without modification of MPTS appeared to be identical (Figure 10.6). In addition to the main apatite phase at 26˚ and 32˚ 2θ, there was evidence of a small quantity of calcite as suggested by peaks in the range of 40˚ to 52˚ 2θ. The incorporation of silicon in the HA xerogels did not change the crystalline structure as a similar poorly crystalline apatite was shown to be present. After the surface of SiHA xerogels was functionalised by the thiol group of MPTS, the phase compositions of SiHA xerogels remained the same.

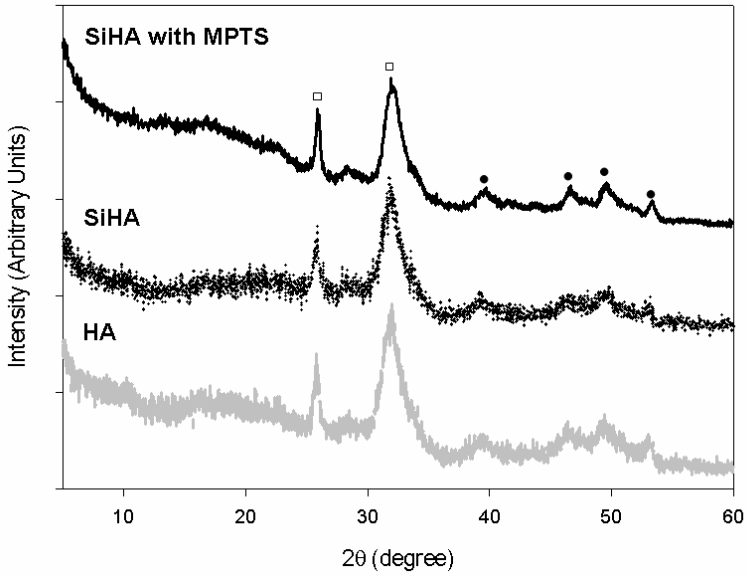

Figure 10.6 XRD patterns of the SiHA xerogel with and without modification as compared to the HA xerogel. The peaks of apatite phase at 26˚ and 32˚ 2θ are labelled as square (□); calcite at 40˚ to 52˚ 2θ as circles (●).

The effect of silicon substitution on the functional groups of HA xerogels, and the surface modification of SiHA xerogels can be respectively evaluated by FTIR analysis (Figure 10.7). The spectrum of the SiHA xerogel was expected to show the peak of silicate (or SiO_x where x=2-4) at approximately 760, and 890 cm^{-1}, but the absorbed bands of the

phosphate groups at these regions were dominant in the range of 876 to 1100 cm $^{-1}$, and 570 to 607 cm^{-1}. In addition, the carbonate abosorption was exhibited at 1644 cm^{-1} in all HA matrices. Moreover, all HA matrices contained some moisture as the peak of hydroxyl groups was present at 3280 cm^{-1}.

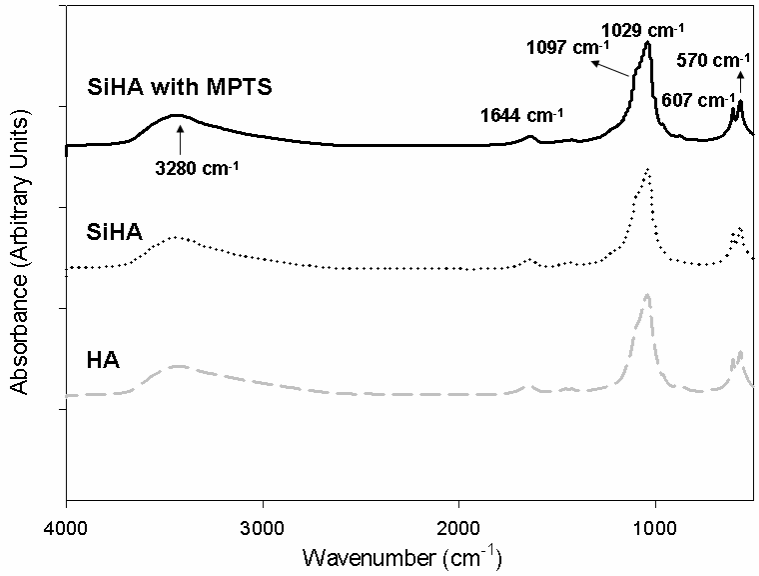

Figure 10.7 FTIR spectra of HA xerogels, SiHA xerogels, and SiHA xerogels with MPTS by pelletizing samples with KBr. There were mainly phosphate groups in the range of 960 to 1100 cm^{-1}, and 470 to 610 cm^{-1} in the HA.

As Figure 10.8 shows, the zeta potential at pH 7.4 of the SiHA xerogel (-3.7 mV) was lower than that of the HA xerogel (-1.3 mV).

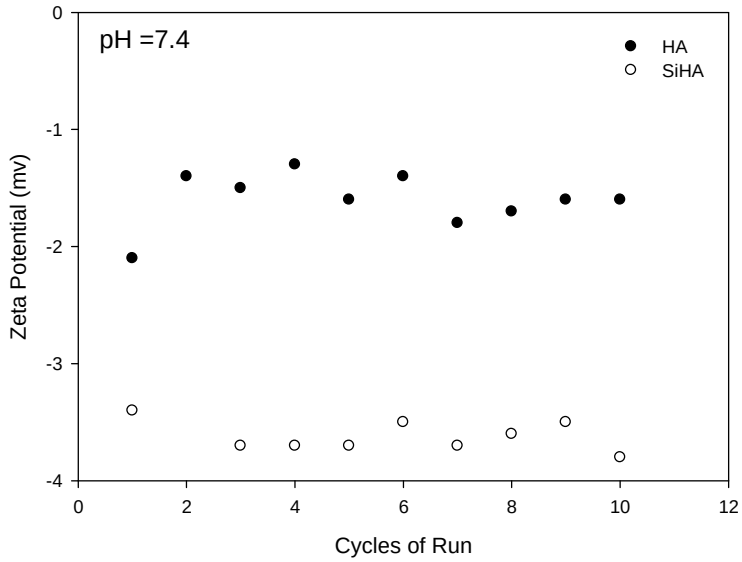

Figure 10.8 Zeta potential of HA and SiHA gels at pH of 7.4 was -1.3 mV and -3.7 mV respectively.

Using high resolution XPS analysis, the calcium peak of the calcite (Ca-O) was recorded at 349.5 eV, and that of the HA (Ca2p) at 346 eV (Figure 10.9). In addition, the phosphate peaks at 132.3 eV decreased with the addition of SiHA with MPTS. However, there was little difference between HA xerogels and SiHA xerogels. The presence of MPTS can be further demonstrated through the high resolution XPS of the Si, SiO_2, and S. Except for the calcium phosphate peaks of HA, the XPS spectra showed that there was an S2p peak of the SiHA xerogels with MPTS at 164 eV. In addition, the intensity of the SiO_2 (102.3 eV) and Si2s (153.3 eV) peaks respectively of the SiHA xerogels with MPTS increased compared with those of the SiHA xerogels (Figure 10.9). As reported by Balas et al., the SiO_2 can be assigned to the silicon atom resulting from the SiO_4 of SiHA [Balas et al. (2003)].

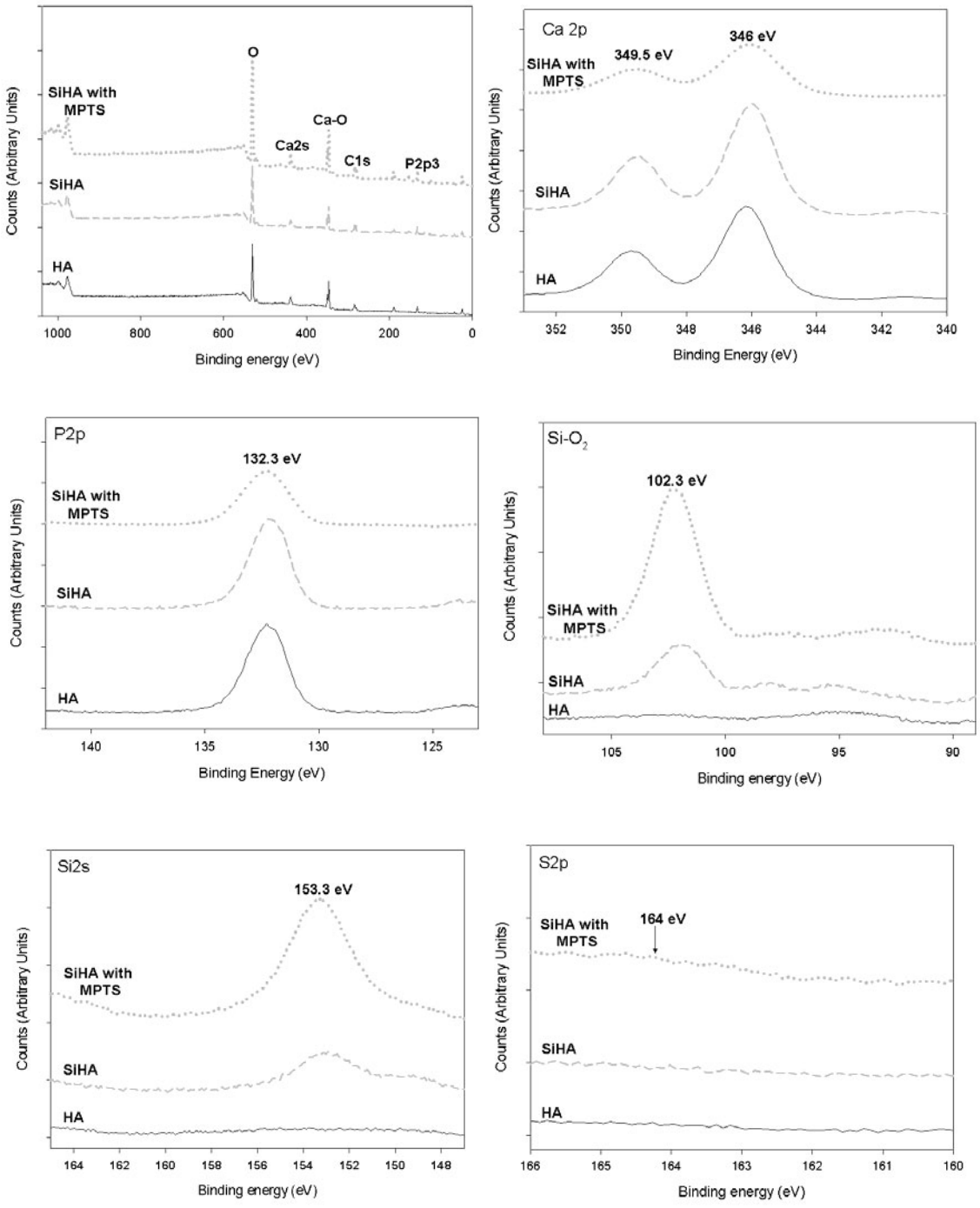

Figure 10.9 The XPS wide scan spectra of surface modification of the HA xerogels, SiHA xerogels and the SiHA xerogel with MPTS. The elemental region of C, Si, and S is narrowly scanned to provide high resolution.

The Ca/P ratio of SiHA xerogels (1.76) was higher than that of HA xerogels (Ca/P ratio of 1.58 as listed in Table 7.1 and 7.2). After counting the wt% of silicon, the Ca/(P+Si) of SiHA xerogels was 1.33. The amount of silicon (wt%) was reduced after the surface of the SiHA xerogels was functionalised by MPTS (Table 10.3) whereas there was 0.03 wt % of sulphur increase in the SiHA xerogel with MPTS. The Ca/P ratio of the SiHA xerogel, corresponding to that recorded in previous work [Gibson et al. (1999)] was the same as that of SiHA xerogels with MPTS, although the Ca/(P+Si) of the SiHA xerogels was less than the Ca/P (1.79) of the SiHA xerogels modified with MPTS.

Table 10.3 Chemical composition of the SiHA xerogels, and modified SiHA xerogels with MPTS using XRF [one measurement].

Samples	Ca weight %	P weight %	S weight %	Si weight %	Ca/P mole ratio
SiHA	32.66	14.30	0.00	4.29	1.76
SiHA with MPTS	32.41	13.98	0.03	3.50	1.79

To further confirm the existence of thiol groups, the SiHA xerogels with MPTS were stained with fluorescein containing maleimide. The maleimide groups react predominantly with sulphhydryl, and the fluorescein reagents are effective for observation using fluorescence microscopy. Figure 10.10 b and d show that the SiHA xerogels with MPTS, and control SiHA xerogels fluoresced green before washing. In contrast, the fluorescence was less intense for the control SiHA xerogels after washing once (Figure 10.11 d); however, the fluorescence of that with MPTS remained (Figure 10.11 b). After repeated washing, the fluorescence of the SiHA xerogel dissipated (Figure 10.12 d), but the SiHA gels with MPTS retained their fluorescence (Figure 10.12 b), this

suggests that the fluorescent dye had been covalently attached to the surface of the particles and hence provides proof for successful surface modification.

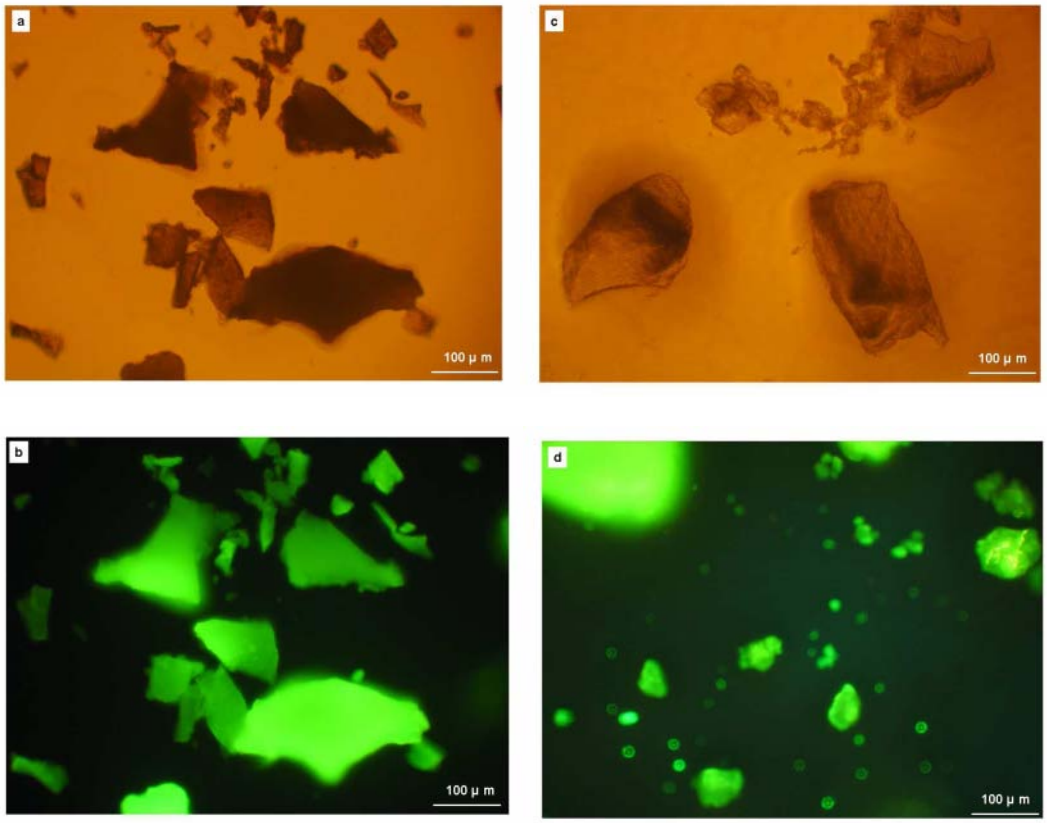

Figure 10.10 Fluorescence microscopy of a) SiHA modified with MPTS and b) SiHA, containing fluorescein-5-maleimide before extensively washing with water and ethanol. Observation was made under bright field (a and c), and with excitation at 490 nm (b and d).

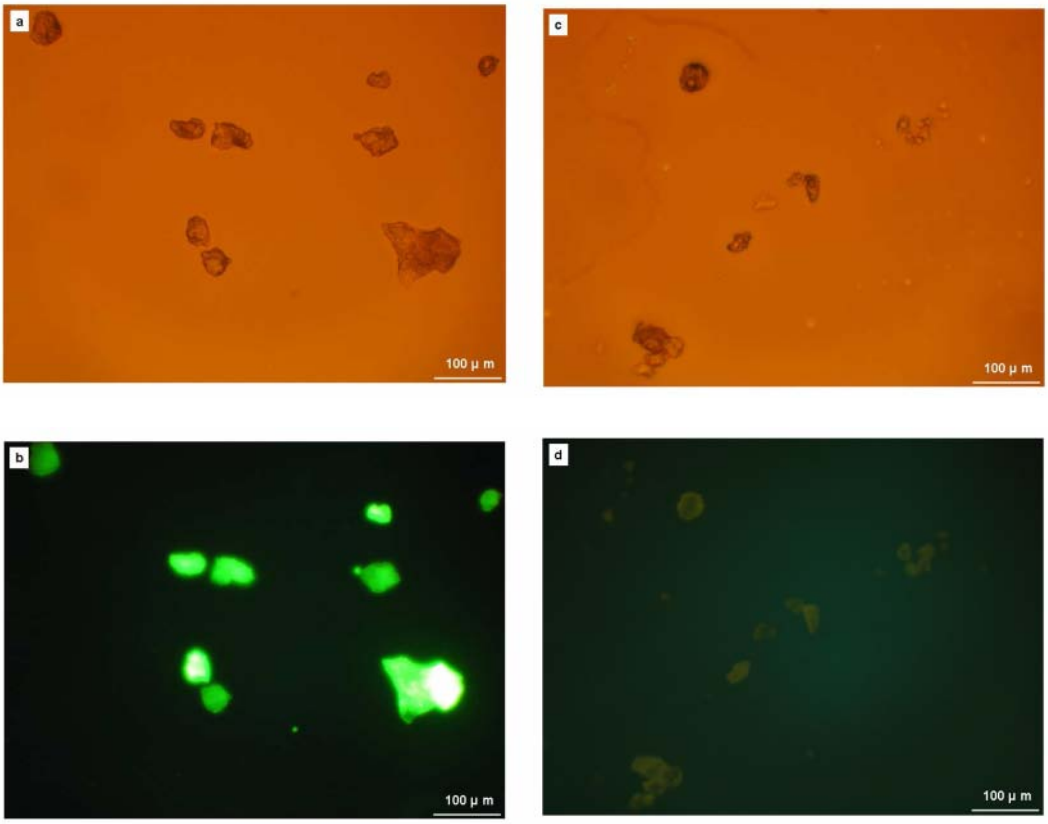

Figure 10.11 Fluorescence microscopy of a) SiHA modified with MPTS and b) SiHA, containing fluorescein-5-maleimide after washing first time with water and ethanol. Observation was made under bright field (a and c), and with excitation at 490 nm (b and d).

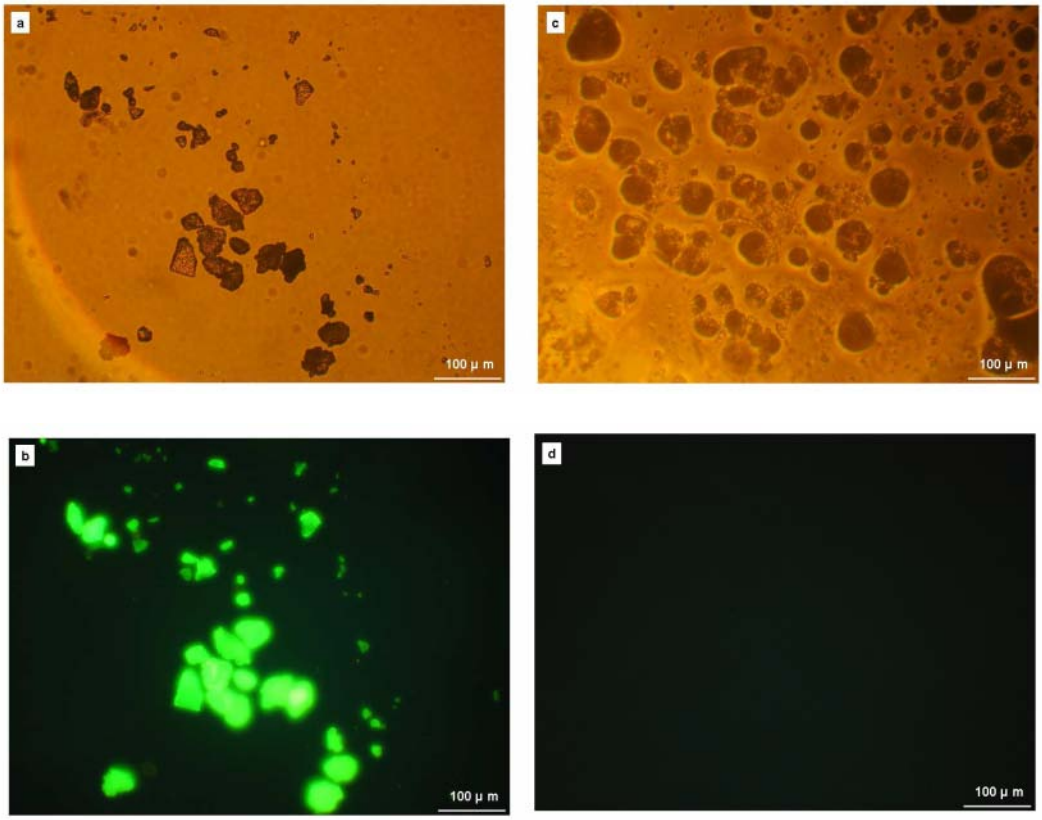

Figure 10.12 Fluorescence microscopy of a) SiHA modified with MPTS and b) SiHA, containing fluorescein-5-maleimide after washing ten times with water and ethanol. Observation was made under bright field (a and c), and with excitation at 490 nm (b and d).

The true density of the SiHA xerogel (2.27 g cm^{-3}) was 86 % of that of the HA xerogel (2.62 g cm^{-3}, Table 7.3). After the additional silicon of MPTS, the true density of the SiHA xerogel with MPTS increased to 2.35 g cm^{-3}, as the density of silica is 2.2 g cm^{-3}.

After modification of SiHA xerogels with MPTS, the particles were distributed in the higher range of 600 to 1300 nm in comparison with those of the SiHA xerogels (Figure 10.13 a and b), meaning the mean particle size of the SiHA xerogel with MPTS (928 nm) was larger than the SiHA xerogels (448 nm), suggesting the modified SiHA with MPTS gel particles agglomerated more readily the unmodified SiHA. However, the specific

surface area of the SiHA xerogel with MPTS (Table 10.4) was greater than that of the SiHA xerogels, because of the irregular shape of crystals of SiHA with MPTS as the TEM images show (Figure 10.14 b).

Table 10.4 Physicochemical characterization of the SiHA xerogels and SiHA xerogels modified with MPTS.

Samples	True Density (g cm^{-3})	Mean Particle Size (nm)	Specific surface area (m^2 g^{-1})
SiHA	2.27 ± 0.01	448.0 ± 72.8	53.5 ± 25.6
SiHA with MPTS	2.35 ± 0.01	928.0 ± 27.3	165.0 ± 0.7

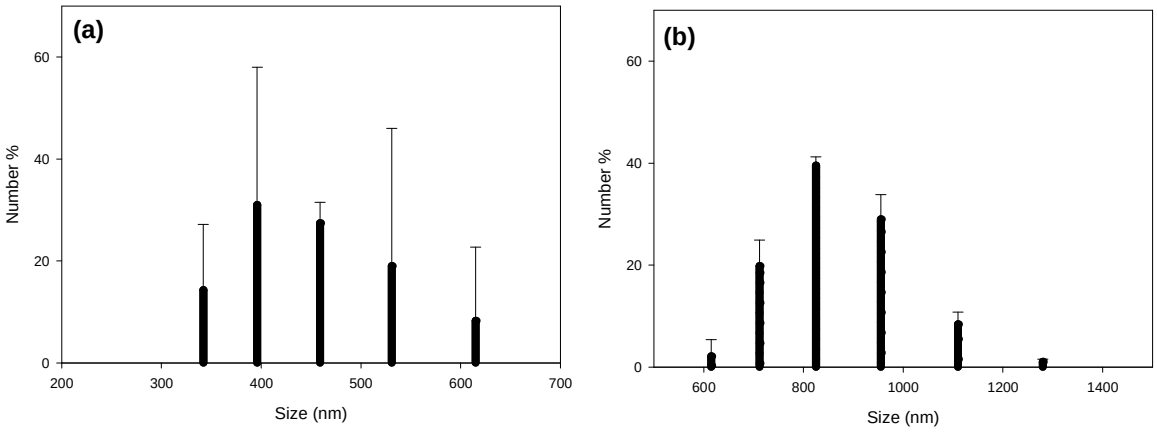

Figure 10.13 The particle distribution of (a) SiHA, and (b) SiHA modified with MPTS. The average particle size of SiHA xerogels with MPTS was increased as compared to the SiHA xerogels.

The crystal of SiHA xerogels without modification was approximately 63 nm in length, and 15 nm in width (Figure 10.14 a). The shape of crystals of SiHA xerogels was needle like. There was a slightly change in crystal shape between the SiHA xerogel and SiHA xerogel with MPTS (Figure 10.14 a and b). The crystal size of SiHA xerogels with MPTS was slightly less than that of SiHA xerogels. The size of fluorescein containing SiHA

xerogels with MPTS (ab. 57 nm) was smaller in length than of that of the SiHA xerogels without, and with modification, but was of greater width (Figure 10.14 c). In addition, the crystal of SiHA with MPTS was a rod shape.

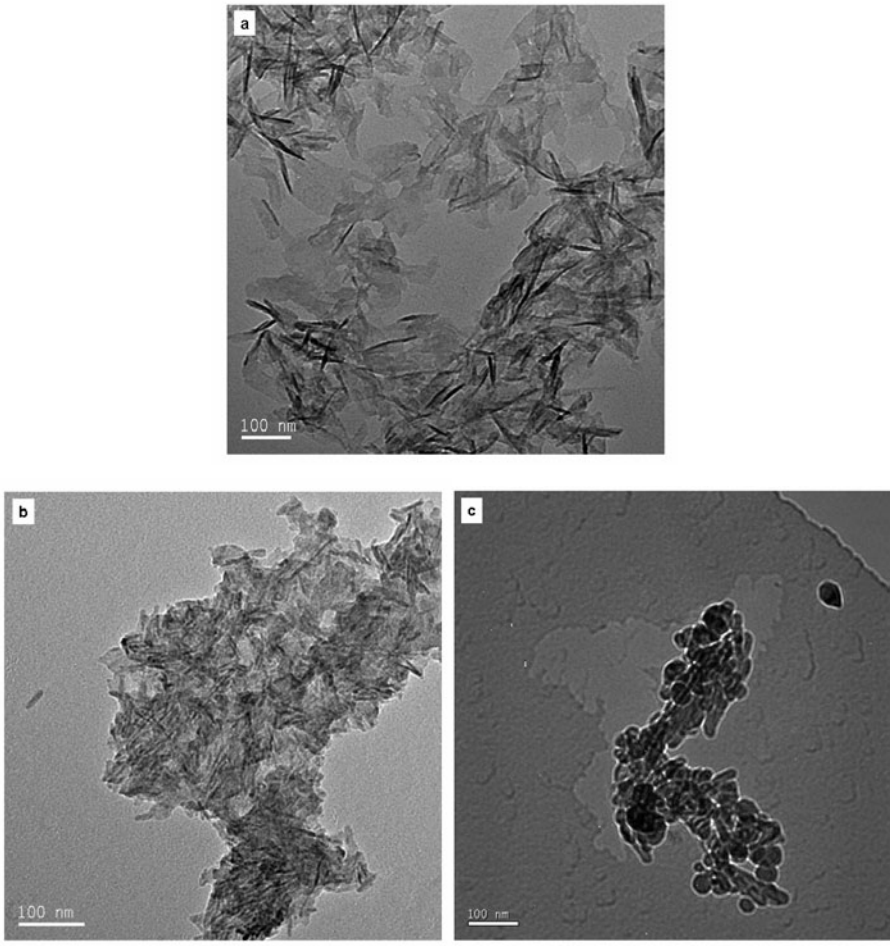

Figure 10.14 TEM images of (a) SiHA; (b) SiHA with MPTS; (c) SiHA with MPTS, containing fluorescein

The median pore diameter of SiHA xerogels was decreased when the silicon was incorporated into the HA xerogels. The pore distribution of SiHA xerogels with MPTS was bimodal; one was in the range of 10 to 100 nm and the other was distributed between 1 and 10 μm (Figure 10.15). Also, the numbers of pores of SiHA xerogels with MPTS increased in the range of 10 to 100 nm as compared to the SiHA xerogels (Figure 10.15). The porosity of SiHA xerogels with MPTS increased with the increased intrusion volume (Table 10.5).

Table 10.5 Characterisation of pore structure of SiHA xerogels without and with modification of MPTS.

Sample	Porosity (%)	Skeletal Density (g cm $^{-3}$)	Bulk Density (g cm^{-3})
SiHA	42.09 ± 5.86	1.82 ± 0.32	1.06 ± 0.29
SiHA with MPTS-	54.52 ± 1.31	2.04 ± 0.09	0.93 ± 0.02
Sample	**Total Intrusion Volume (g^{-1} cm^3)**	**Median Pore Diameter (nm)**	**Total Pore Area (g^{-1} m^2)**
SiHA	0.42 ± 0.17	13.35 ± 8.70	24.12 ± 17.49
SiHA with MPTS-	0.59 ± 0.01	12.45 ± 5.16	29.65 ± 11.22

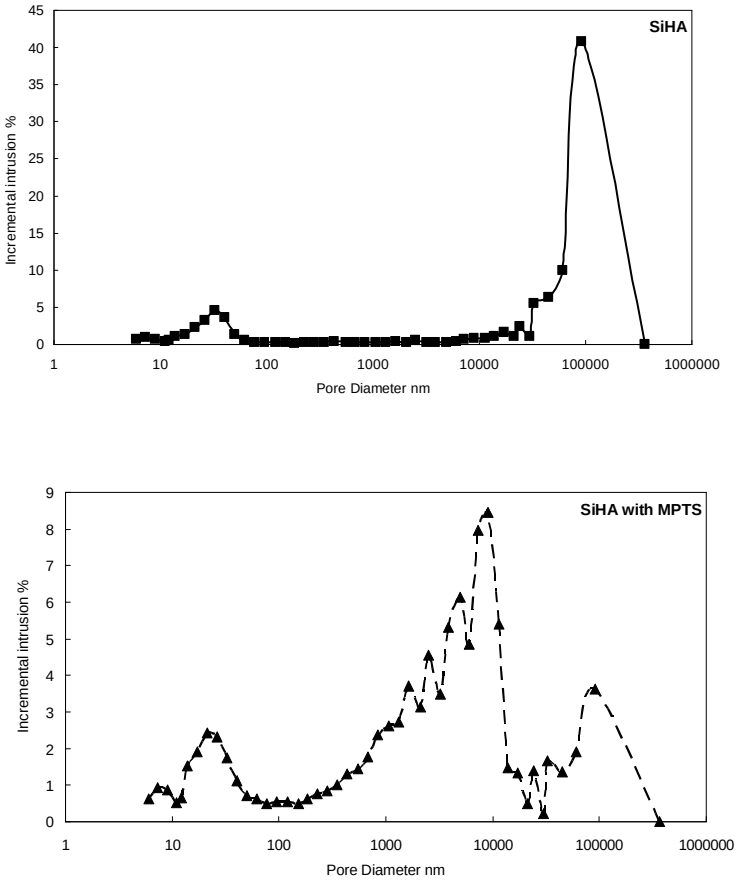

Figure 10.15 Mercury intrusion curves of the SiHA xerogels without, and with, MPTS. The interstitial pores were in the range of 10 to 100 nm for SiHA xerogels, and the interstitial pores of SiHA with MPTS were distributed in the range of 10 to 100 nm, and 1 to 10 µm.

10.4 Discussion

10.4.1 The effect of silicon on the structure of hydroxyapatite

Recently, Lee et al. confirmed that the sulphhydryl groups of MPA have been attached to the surface of HA as indicated by XPS spectra, and by Ellman's reagent analysis [Lee et al. (2007)]. However, their work is controversial since in the published paper, the proposed presence of the sulphur peak is not convincing. It could simply be noise, resulting from the background. Indeed, our findings suggest that this method of surface modification was highly ineffective. According to FTIR spectra (Figure 10.3), although there was a peak of carbonate at 1644 cm^{-1}, it was difficult to identify whether the absorption arise from C=O of MPA, or C-O of CO_2 because a small peak at 1644 cm^{-1} was present in the unmodified HA xerogels. The C-H bonding (2850-3000 cm^{-1}) was alternative measurement for MPA, but it might result from an overlap with the moisture in the sample as the absorption of water appeared approximately at 3280 cm^{-1} in the unmodified HA xerogels. From the high resolution XPS (S2p) spectra (Figure 10.4), there was no indication of sulphur at the binding energy, 164 eV although there was 0.02 wt% of sulphur present as determined using other analyses (Table 10.1).

It was proposed that the surface modification mechanism resulted from the carboxyl groups on the modifying chemical reacting with calcium ions, but it is more likely that they reacted with absorbed carbonate on the surface of HA, which would explain the trace amount of sulphur found using XRF, which is a surface characterisation method (Table 10.1). The hypothesis is further demonstrated by the particle size. In comparison to the MPA, the surface properties of HA modified with MPA did not show significant changes in particle size after modification (Table 10.2) although the particle size of HA

xerogel with MPA was smaller than the HA xerogel (565 nm as listed in Table 7.3). This might result from the reduction of adhesive forces between the HA xerogels with MPA.

Presuming that the surface modification was limited by the availability of carbonate absorbed to the surface of the precipitate, the decision was made to incorporate silicon into the CaP gels, which would provide further sites for modification with functional groups. The addition of silicon during the precipitation of the apatite, had no significant influence on the crystalline phase composition of the resulting gel when compared with the HA xerogel (Figure 10.6), suggesting the incorporation of silicon does not affect the formation of the apatitic phase. According to the XPS spectra, the silicon was present in the form of a SiO_4 group. Consequently, the mechanism of substitution was proposed as in Equation 10.2.

$$10Ca^{+2} + (6-x)PO_4^{3-} + SiO_4^{4-}x + (2-x)OH^- \rightarrow Ca_{10}(PO_4)_{6-x}(SiO_4)_x(OH)_{2-x}$$

Equation 10.2

The high concentration of silicon in the reaction medium substitutes for phosphate groups of the HA xerogel and results in a considerable reduction in the Ca/P ratio [Gibson et al. (2002)]. The low Ca/(P+Si) of SiHA xerogels (1.33) could also be due to the calcium deficiency of the HA xerogel (1.58) (Table 10.3 and Table 7.1 and Table 7.2). Furthermore, because the density of silica is 2.2 g cm^{-3}, it was more likely that there were some poorly X-ray amorphous calcium phosphates present (Table 10.4). Although it is unclear whether the intensity of hydroxyl increased after the substitution of silicon, the reduction of zeta potential of SiHA xerogels after the modification suggests a loss of charge because of the replacement of PO_4^{3-} by SiO_4^{4-} to maintain the charge balance

(Figure 10.8), which agrees with Botelho et al.'s finding [Botelho et al. (2002)]. The effect of silicon on the surface characterisation demonstrates the surface properties of the precipitate (Table 10.4). After the addition of silicon, the particle size of HA xerogels was distinctly reduced. This might result from a decrease of crystalline size with the addition of silicon, especially when the concentration of silicon is increasing [Thian et al. (2006)]. Therefore, the pores of HA xerogels shifted from 40 nm to 32 nm with increased mercury intrusion after the addition of silicon.

10.4.2 The effect of surface modification by thiol groups on the microstructure

To test the hypothesis that 'the addition of silicon enhances the number of binding sites for surface modification', the surface of the precipitate was modified using thiol groups. Amongst surface modified techniques, the self-assembled monolayer or mutilayers of organosilanes has been widely used to promote or inhibit specific molecular attachment [Ulman (1991)]. It has been confirmed that self assembly MPTS layers were deposited on silicon oxide [Hu et al. (2001)]. Here, it has been demonstrated that the thiol functional group can attach on the surface of the SiHA xerogel without the alteration of crystal structure (Figure 10.6). An XPS survey of the precipitate (Figure 10.9) showed that the sulphur peak was present in the SiHA xerogels with MPTS. These results correspond to the images of fluorescence microscopy (Figure 10.10-10.12). The SiHA xerogels with MPTS labelled with fluorescein fluoresced green when excited using the fluorescence microscope whereas the control SiHA xerogels after extensively washing with ultrasonic treatment did not. The attachment between fluorescein and SiHA xerogels with MPTS is covalent bonding. This is proven since the bond could not easily be destroyed either by washing with double distilled water/ethanol or by ultrasonic treatment. Furthermore, there was no difference between the SiHA xerogel, and the SiHA xerogel with MPTS,

implying that modification of thiol groups occurred on the surface of SiHA xerogels (Table 10.3). In addition, XRF showed 0.03 wt% of sulphur existed in the SiHA xerogels with MPTS.

The porous structures of the SiHA xerogels with MPTS were improved by an increase of 28 % porosity in comparison with the unmodified SiHA xerogel (Table 10.4). This is due to the formation of an Si-O-Si network. The formation of an Si-O-Si network results in a slightly denser structure as the true density of SiHA xerogels with MPTS is increased as compared to SiHA xerogels. The more dense structure of SiHA xerogels with MPTS also can be found in the reduction of large voids (Figure 10.15). Moreover, there is three times more specific surface area resulting from the increase of interstitial pore size (1-10 μm), which suggests more binding sites are available for attaching of biomolecules. The alteration of surface properties further explains the successful modification of SiHA xerogels with MPTS. It is critical to supply sufficient binding sites for surface modification.

10.5 Conclusion

In this study, it has been demonstrated that SiHA can be prepared by the sol-gel process. In addition, the presence of silicon groups on the surface of the particles provided a greater number of binding sites for surface modification than the HA xerogel without silicon groups. This method for surface modification of apatite, therefore, is a significant improvement on those currently reported in the literature. The surface properties of SiHA xerogel can be engineered through modification of the thiol functional groups. These results suggest that it is feasible to form covalent bonds on the surface of the apatite.

Chapter 11 Conclusions

Since the 1970's hydroxyapatite based calcium phosphate ceramics have been synthesised for use as bone graft replacements. These materials were traditionally synthesised using methods that required treatment at elevated temperatures. Although these materials are well tolerated in the body following implantation, they have not surpassed autograft as the 'gold standard' in bone replacement. One reason for this is although they exhibit a similar composition to the mineral component of bone, the crystals from which they are formed are significantly different. Calcium phosphate ceramics formed using sintering are typically microcrystalline rather than the nanocrystalline nature of the hydroxyapatite in bone or tooth. Also, the inclusion of heat treatment during processing means that it is impossible to incorporate heat sensitive therapeutic molecules into the material during processing. This study has shown that it is possible to form a predominantly apatitic ceramic monolith in ambient conditions. Importantly, the results have shown that this monolith can be used for the encapsulation and delivery of both heat sensitive drugs (vancomycin hydrochloride) and enzymes of therapeutic benefit (alkaline phosphatase). Furthermore, it has demonstrated a novel method for the surface modification of these apatite monoliths that will enable covalent immobilisation of molecules on the surface of the material.

11.1 Influence of process conditions on the physicochemical properties of CaP gels

It has been demonstrated that the physicochemical properties of CaP gels can be modified by varying process conditions. Following an investigation of the influence of process conditions on gel formation, it can be concluded that:

- By changing the relative humidity (RH) at which the gel monoliths are stored during processing, it is possible to exhibit some control over composition and the pore structure.
- Apatitic phases are formed within the CaP gels regardless of the RHs in which the gels are aged.
- The addition of carbonate causes a reduction of crystal size, but an increase in the relative porosity exhibited by the gel matrix.
- The formation of the secondary phases results from the dissolution-reprecipitation that can occur during the ageing process.

11.2 Comparing the efficacy of calcium phosphate based matrices for the release of vancomycin hydrochloride

The CaP gels were successful in delivering a therapeutic dose of vancomycin hydrochloride for an extended period of time, and were significantly more effective than calcium phosphate based cements. It can be concluded that:

- The therapeutic function of the incorporated vancomycin hydrochloride is maintained when encapsulated in a CaP gel, when compared with calcium phosphate cement based matrices.
- The effectiveness of the delivery matrix is determined by both the activity of the released vancomycin, and the rate of release from the ceramic matrix.
- The intrinsic pH of calcium phosphate matrices during the process determines the activity of vancomycin hydrochloride.

- The predictive kinetics of the incorporated vancomycin of the CaP gels suggests that vancomycin hydrochloride is homogeneously dispersed throughout the matrix, since the release curve follows the Higuchi and Peppas models.

11.3 Calcium phosphate cryogels for enzyme encapsulation

The CaP gels were shown to be effective at storing both HRP and ALP for an extended period of time following immersion in the eluent. It can be concluded that:

- The activity of HRP/ALP is preserved within the mesoporous structure of the apatitic cryogels.
- The encapsulation of HRP/ALP affects the microstructure of apatitic cryogels because of the high molecular weight of these enzymes.
- The loading efficiency of ALP (85 %) is higher than that of HRP (66 %).
- In contrast to that of the ALP, the catalytic behaviour of the incorporated HRP is affected by the mass transport of ABTS cations through the matrix.
- The catalytic behaviour of ALP can be expressed by the Michaelis-Menten or the Lineweaver-Burk equations. However, neither of these two kinetic equations is fitted by HRP as a result of unsteady state kinetics of HRP.

11.4 Surface modification of calcium phosphate gels via sulphhydryl groups

By considering the mechanism of surface modification of calcium phosphate based particles, it has been possible to design a method for surface modification that is considerably more efficient than those reported in the literature. From the findings of this study, it can be concluded that:

- The number of binding sites of calcium phosphate matrices for attaching functional groups can be increased by the incorporation of silicon.
- The crystalline structures of calcium phosphate gels were not changed following the incorporation of silicon.
- There was no difference shown between the apatitic phases following modification by thiol groups.
- The increased specific surface area and the fluorescence of silicon substituted apatites with the thiol modification demonstrated that surface modification using MPTS is more efficient than the method using MPA.
- The thiol terminated functional groups on the surface of the silicon substituted apatites can be introduced by forming the chemical bonding of silanol groups.

Chapter 12 Future Work

The calcium phosphate gels studied for this thesis have shown a variety of porosity consequent on applying different ageing regimes. In addition, the mild pH and mesopores of calcium phosphate gels enable the preservation of the activity of therapeutic molecules. For these materials to be used as bone replacements, it will be necessary to further characterise both mechanical performance of the ceramic monolith and also the biological reponse to the material.

12.1 The properties of calcium phosphate gels

The different ageing regimes have been shown to create different pore size distributions in the calcium phosphate gels. However, as the results showed, there were secondary phases produced because of the incomplete reaction between calcium and phosphate ions. According to the previous studies [Liu et al. (2001)], it has been found that sufficient ageing time is significant for the formation of the pure apatitic phase. Therefore, a further ageing study is required to determine the best ageing conditions to allow the formation of impurity free CaP gels.

Although it has been demonstrated that calcium phosphate gels can be used as drug carriers, their limited mechanical strength restricts their use in load bearing applications. It may be possible to form a calcium phosphate ‘concrete’ by combining granules of the CaP gel containing therapeutic molecules with calcium phosphate cements, which typically exhibit superior mechanical properties. In this material, the gel could protect the functionality of the drug/protein [Dion et al. (2005)], while the cement provides the mechanical integrity.

12.2 The evaluation of functionality of calcium phosphate gels

Calcium phosphate gels are known for their osteoconductivity, but they generally lack osteoinductivity. In Chapter 9, it was shown that calcium phosphate gels can entrap ALP and allow the activity to be maintained over a period of time *in vitro*. It is possible that ALP or another biological active moiety such as bone morphogenic protein (BMP) may cause the materials to be osteoinductive. In addition, it may be possible to attach BMPs to the surface of the ceramic using the attached thiol groups.

12.3 Formation of disulphide bonds to improve the mechanical properties of calcium phosphate gels

In the Chapter 10 of surface modification, it has demonstrated that it is feasible to attach the thiol groups on the surface of calcium phosphate gels. In addition, disulphide bridges can be formed by effectively oxidised thiol groups by reacting with hydrogen peroxide in the presence of a catalytic amount of iodine [Kirihara et al. (2007)]. By forming disulphide bonding between gel particulates, the adhesive forces within gel particulates can be enhanced. Also, with disulphide linkage, there is the opportunity to control the local delivery of proteins. Wright et al. have shown disulphide-linked conjugates are readily cleavable by cystein *in vitro* [Wright et al. (2006)].

Chapter 13 Appendix

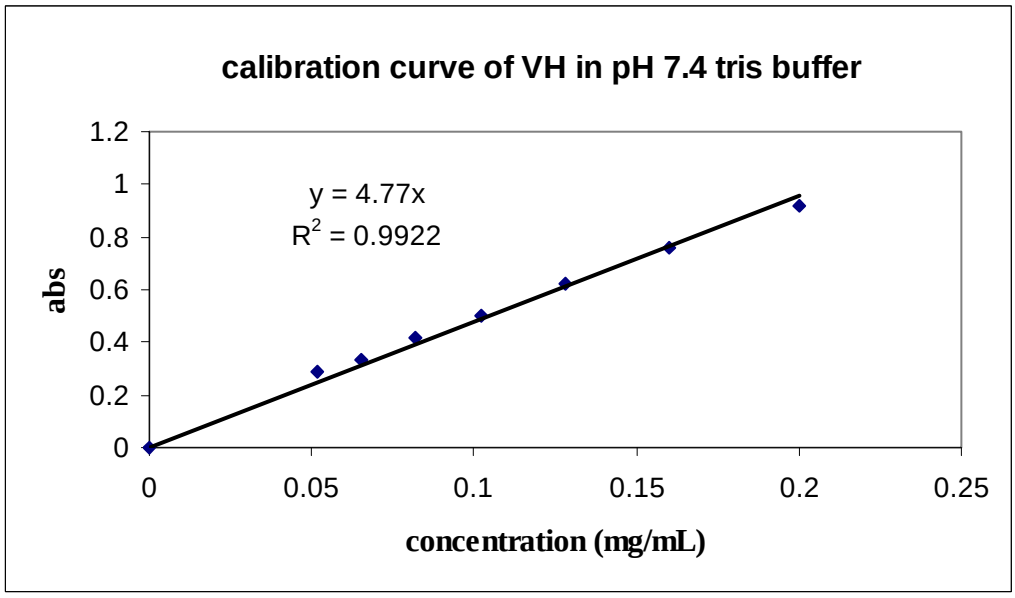

Figure 13.1 The calibration curve of vancomycin hydrochloride (VH) in pH 7.4 tris buffer solution

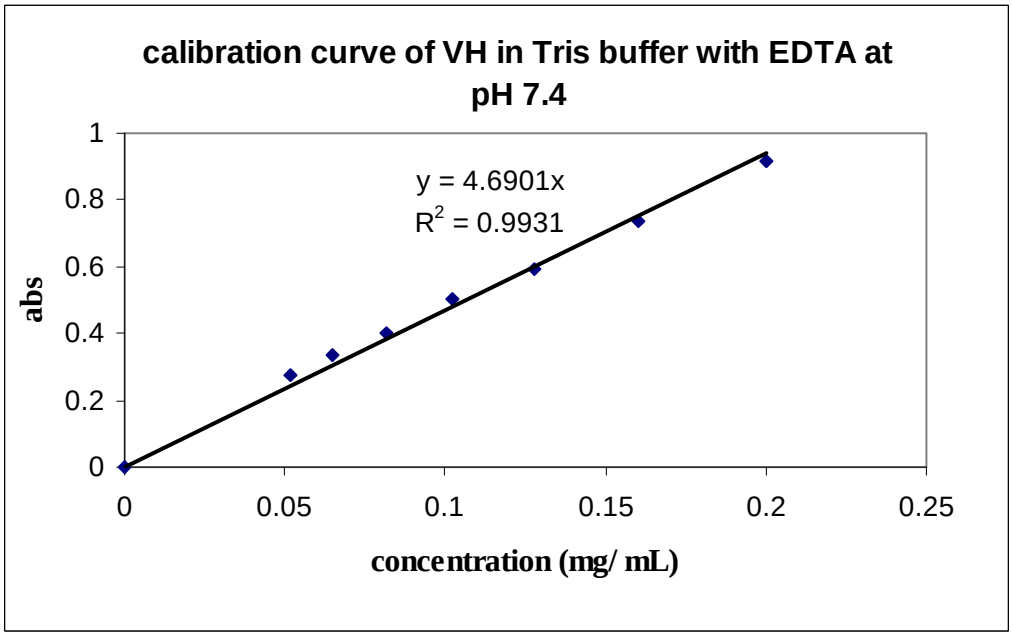

Figure 13.2 The calibration curve of VH in 3 wt% of ethylenediaminetetraacetatic acid tetrasodium salt hydrate (Na4 -EDTA) solution.

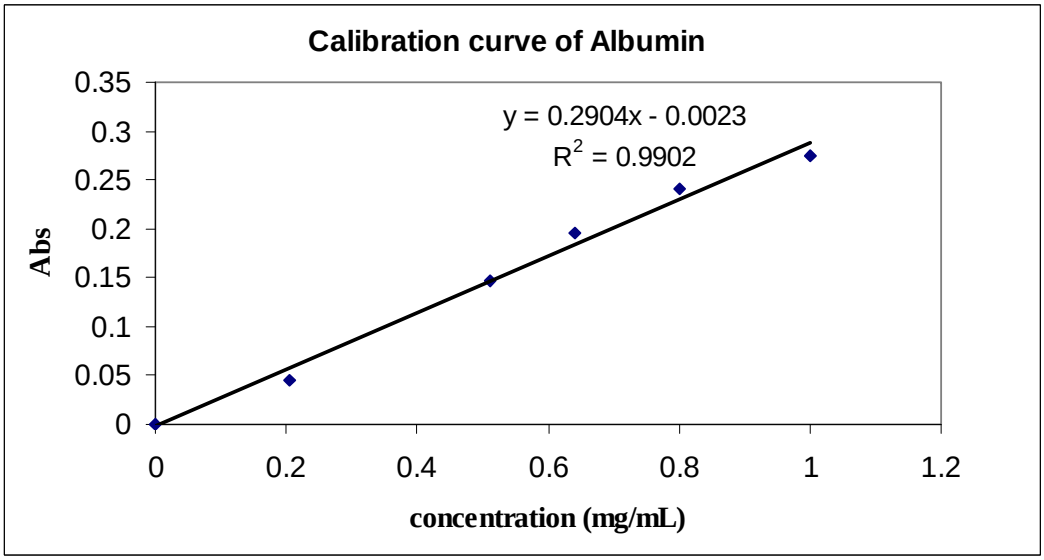

Figure 13.3 The calibration curve of albumin in phosphate solution.

Chapter 14 References

- Anderson, H. C. Sipe, J. B. Hessle, L. et al. 2004. Impaired calcification around matrix vesicles of growth plate and bone in alkaline phosphatase-deficient mice. Am. J. Pathol. 164: 841–847.
- Anderson, J. C. Leaver, K. D. Rawlings, R. D. et al. 1990. Materials Science. Fourth Edition, Chapman & Hall, London, UK. pp 294.
- Antipas, A. S. Van der Velde, D. G. Stella, V. J. 1994. Factors affecting the deamidation of vancomycin in aqueous-solutions. Int. J. Pharm. 109: 261-269.
- Appleford, M. R. Oh, S. Oh, N. et al. 2009. *In vivo* study on hydroxyapatite scaffolds with trabecular architecture for bone repair. J. Biomed. Mater. Res. A 89A: 1019-1027.
- Arora, S. K. 1981. Advances in gel growth: a review. Prog. Crystal. Growth. Charact. 4: 345-378.
- Baker, A. S. Greenham, L. W. 1988. Release of gentamicin from acrylic bone cement. J. Bone Joint Surg. [Am.] 70A:1551-1557.
- Balas, F. Pérez-Pariente, J. Vallet-Regí, M. 2003. In vitro bioactivity of silicon substituted hydroxyapatite. J. Biomed. Med. Res. 66A:364-375.
- Barralet, J. E. Best, S. M. Bonfield, W. 1996. Carbonate hydroxyapatite gel monolith formation and drying. Biomed. Mater. Eng. 6: 101-112.
- Barralet, J. E. Gaunt, T. Wright, A. J. et al. 2002. Effect of porosity reduction by compaction on compressive strength and microstructure of calcium phosphate cement. J. Biomed. Mater. Res. Part B: Appl. Biomater 63: 1-9.
- Barralet, J. E. Best, S. M. Bonfield, W. 1998. Carbonate substitution in precipitated hydroxyapatite: an investigation into the effects of reaction temperature and bicarbonate ion concentration. J. Biomed. Mater. Res. 41: 79-86.
- Barralet, J. E. Aldred, S. Wright, A. J. et al. 2002. In vitro behavior of albumin-loaded carbonates hydroxyapatite gel. J. Biomed. Mater. Res. 60: 360-367.
- Bassett, C. A. Mitchell, S. N. Schink, M. M. 1982. Treatment of therapeutically resistant non-unions with bone grafts and pulsing electromagnetic fields, J. Bone Joint Surg. Am. 64:1214-1220.
- Beortsen, W. van den Bos, T. 1992. Alkaline phosphatase induces the mineralization of sheets of collagen implanted subcutaneously in the rat. J. Clin. Invest. 89: 1974-1980.
- Best, S. M. Bonfield, W. 1994. Processing behaviour of hydroxyapatite powders with contrasting morphology. J. Mater. Sci. Mater. Med. 5: 516-521.

- Bernhardt, A. Lode, A. Boxberger, S. et al. 2008. Mineralised collagen-an artificial, extracellular bone matrix-improves osteogenic differentiation of bone marrow stromal cells. J. Mater. Sci. Mater. Med. 19: 269-275.
- Bickerstaff, G. F. 1987. Enzymes in industry and medicine. Edward Arnold, London.
- Bhatia, R.B. Brinker, C. J. Gupta, A. K. et al. 2002. Aqueous sol-gel process for protein encapsulation. Chem. Mater. 12: 2434-2441.
- Bilezikian, J. P. Raisz, L. G. Rodan, G. A. 1996. Principles of bone biology, Academic Press, London. pp 3-4.
- Bohner, M. Lemaître, J. Van Landuyt, P. et al. 1997. Gentamicin-loaded hydraulic calcium phosphate bone cement as antibiotic delivery system. J. Pham. Sci. 86: 565-572.
- Bohren, C. F. Huffman, D. R. 1983. Absorption and scattering of light by small particles. Wiley, London. pp 287.
- Botelho, C. M. Lopes, M. A. Gibson, I. R. et al. 2002. Structural analysis of Si-substituted hydroxyapatite: zeta potential and X-ray photoelectron spectroscopy. J. Mater. Sci. Mater. Med. 13: 1123-1127.
- Bonfield, W. 1988. Hydroxyapatite-reinforced polyethylene as an analogous material for bone replacement. Annals New York Acad. Sci. 532: 173-177.
- Boyan, B. D. Sylvia, V. L. Dean, D. D. et al. 1996. Cell biology of calcified tissues: experimental models of differentiation and mechanisms by which local and systemic factors exert their effects. Connect. Tissue Res. 35: 63-70.
- Boyer, L. Carpena, J. Lacout, J. L. 1997. Synthesis of phosphate-silicate apatites at atmospheric pressure. Solid State Ionics 95: 121-129.
- Brinker, C. J. Scherer. G. W. 1990. Sol-gel science. The physics and chemistry of sol-gel processing, Academic Press, London. pp 357-453.
- Braun, S. Rappoport, S. Zusman, R. et al. 1990. Biochemically active sol-gel glasses: the trapping of enzymes. Mater. Lett. 10: 1-5.
- Brown, P.W. Constatz, B. 1994. Hydroxyapatite and related materials, CRC, London.
- Brown, W. E. Chow, L. C. 1983. A new calcium phosphate setting cement. J. Dent. Res. 62: 672.
- Carlisle, E. M. 1970. Silicon: A possible factor in bone calcification. Science 167: 279-280.
- Carvalho Vila, M. M. D. Machado de Oliveira, R. Gonçalves, M. M. et al. 2007. Analytical methods for vancomycin determination in biological fluids in pharmaceuticals. Quimica. Nova. 30: 395 -399.

- Chibata, I. 1978. Immobilization enzymes. John Wiley & Sons, Halsted Press, London.
- Chu, G. T.-M. Orton, D. G. Hollister, S. J. et al. 2002. Mechanical and in vivo performance of hydroxyapatite implants with controlled architectures. Biomaterioals 23: 1283-1293.
- Colomban, Ph. 1989. Gel technology in ceramics, glass-ceramics and ceramic-ceramic composites. Ceram. Int. 15: 23-50.
- Conterno, L. O. da Silva Filho, C. R. 2009. Antibiotics for treating chronic osteomyelitis in adults, Cochrane Database of Systematic Reviews [CD004439 DOI: 10.1002/14651858.CD004439] [Accessed October 28th 2008]
- Costa, P. Lobo, J. M. S. 2001. Modeling and comparison of dissolution profiles. Eur. J. Pharm. Sci. 13: 123-133.
- Dahner, L. E. Funderburk, C. H. 1987. Gentamicin-loaded plaster of paris as a treatment of experimental osteomylitis in rabbits. Clin. Orthop. 219: 278-282.
- Damien, C. J. and Parsons, J. R. 1991. Bone graft and bone graft substitutes: A review of current technology and applications. J. Appl. Biomater. 2: 187-208.
- D'Andrea S. C. and Fadeev, A. Y. 2003. Covalent surface modification of calcium hydroxyapatite using n-alkyl- and n-fluoroalkylphosphonic acids. Langmuir 19: 7904-7910.
- De Groot, K. 1983. Bioceramics of calcium phosphate. CRC Press, Florida. pp 2-11.
- De Jonge, L. T. Leeuwenburgh, S. C. G. Wolke, J. G. C. et al. 2008. Organic-inorganic surface modifications for titanium implant surfaces. Pharm. Res. 25: 2357-2369.
- Dion, A. Langman, M. Hall, G. et al. 2005. Vancomycin release behaviour from amorphous calcium polyphosphate matrices intended for osteomyelitis treatment. Biomaterials 26: 7276-7285.
- Dorozhkin, S. V. Epple, M. 2002. Biological and medical significance of calcium phosphates. Angew. Chem. Int. Ed. 41: 3130-3146.
- Dorozhkin, S. V. 2007. Calcium orthophosphates. J. Mater. Sc. 42: 1061-1095.
- Dorozhkin, S. V. 2008. Calcium orthophosphates cements for biomedical application. J. Mater. Sc. 43: 3028-3057.
- Duan, K. Wang, R. 2006. Surface modifications of bone implants through wet chemistry, J. Mater. Chem. 16: 2309-2321.
- Ducheyne, P. Qiu, Q. 1999. Bioactive ceramics: the effect of surface reactivity on bone formation and bone cell function. Biomaterials 20: 2287-2303.
- Eggins, B. R. 2002. Chemical Sensors and Biosensors, John Wiley & Sons, Chichester. pp 98-102.

- Elliott, J.C. 1994. Studies in Inorganic Chemistry 18 Structure and Chemistry of the apatite and other calcium orthophosphates. Elsevier Science, Amsterdam.
- El-Hammari, L. Marroun, H. Laghzizil, A. et al. 2008. Organically modified porous hydroxyapatites: A comparison between alkylphosphonate grafting and citrate chelation. J. Solid Stat. Chem. 181: 848-854.
- Fellah, B. H. Josselin, N. Chappard, D. et al. 2007. Inflammatory reaction in rats muscle after implantation of biphasic calcium phosphate micro particles. J. Mater. Sci. Mater. Med. 18: 287-294.
- Fernandez, E. Gil, F. J. Ginebra, M. P. et al. 1999. Calcium phosphate bone cements for clinical applications Part I: Solution chemistry. J. Mat. Sci. Mat. Med. 10: 169-176.
- Ferraz, M. P. Monteiro, F. J. Manuel, C. M. 2004. Hydroxyapatite nanoparticles: A review of preparation methodologies. J. Appl. Biomater. & Biomech. 2: 74-80.
- Filmon, R. Baslé, M. F. Atmani, H. et al. 2002. Adherence of osteoblast-like cells on calcospherites developed on a biomaterial combining poly(2-hydroxyethyl) methacrylate and alkaline phosphatase. Bone 30: 152–158.
- Fleisch, H. Bisaz, S. 1962. Mechanism of calcification-inhibitory role of pyrophosphate. Nature 195: 911.
- Frenkel-Mullerad, H. D. Avnir, H. 2005. Sol-gel materials as efficient enzyme protectors: preserving the activity of phosphatases under extreme pH conditions. J. Am. Chem. Soc. 127: 8077-8081.
- Fricke, J. Tillotson, T. 1997. Aerogels: production, characterization, and applications. Thin Solid Film 297: 212-223.
- Gammill, L. S. Sive, H. 2000. Coincidence of otx2 and BMP4 signaling correlates with Xenopus cement gland formation. Mech. Dev. 92: 217-226.
- Gautier, H. Caillon, J. LeRay, A. M. et al. 2000a. Influence of isostatic compression on the stability of vancomycin loaded with a calcium phosphate-implantable drug delivery device. J. Biomed. Mater. Res. 52: 308-314.
- Gautier, H. Merle, C. Auget, J. L. et al. 2000b. Isostatic compression, a new process for incorporating vancomycin into biphasic calcium phosphate: comparison with a classical method. Biomaterials 21: 243-249.
- Gautier, H. Daculsi, G. Merle, C. 2001. Association of vancomycin and calcium phosphate by dynamic compaction: in vitro characterization and microbiological activity. Biomaterials 22: 2481-2487.
- Gbureck, U. Knappe, O. Grover, L. M. et al. 2005a. Antimicrobial potency of alkali ion substituted calcium phosphate cements. Biomaterials 26: 6880-6886.

- Gbureck, U. Spatz, K. Thull, R. et al. 2005b. Rheological enhancement of mechanically activated α-tricalcium phosphate cements. J. Biomed. Mater. Res. Part B: Appl. Biomater. 73B: 1-6.
- Gbureck, U. Thull, R. Barralet, J. E. 2005c. Alkali ion substituted calcium phosphate cement formation from mechanically activated reactants. J. Mater. Sci. Mater. Med. 16: 423-427.
- Gbureck, U. Vorndran, E. Barralet, J. E. 2008. Modeling vancomycin release kinetics from microporous calcium phosphate ceramics comparing static and dynamic immersion conditions. Acta. Biomater. 4:1480-1486.
- Gbureck, U. Vorndran, E. Müller, F. A. et al. 2007. Low temperature direct 3D printed bioceramics and biocomposites as drug release matrices. J. Controlled Release 122:173-180.
- Gibson, I. R. Best, S. M. Bonfield, W. 1999. Chemical characterization of silicon-substituted hydroxyapatite. J. Biomed. Mater. Res. 44: 422–428.
- Gibson, I. R. Bonfield, W. 2002. Novel synthesis and characterization of an AB-type carbonate-substituted hydroxyapatite. J. Biomed. Mater. Res. 59: 697–708.
- Gregg, S. J. Sing, K. S. W. 1982. Adsorption, surface area and porosity. Academic Press, London. pp 26, 41-45, 173-175.
- Grover, L. M. Knowles, J. C. Fleming, G. J. P. Barralet, J. E. 2003. In vitro ageing of brushite calcium phosphate cement. Biomaterials 24: 4133-4141.
- Gupta, D. Venugopal, J. Mitra, S. et al. 2009. Nanostructured biocomposite substrates by electrospinning and electrospraying for the mineralization of osteoblasts. Biomaterials 30: 2085-2094.
- Gupta R. Kumar, A. 2008. Bioactive materials for biomedical applications using sol-gel technology. Biomed. Mater. 3:1-15.
- Guelcher, S. A. Hollinger, J. O. 2006. An introduction to biomaterials. Taylor & Francis, New York. pp 3-14.
- Habraken, W. J. E. Boerman, O. C. Wolke, J. G. C. et al. 2009. In vitro growth factor release from injectable calcium phosphate cements containing gelatine microspheres. J. Biomed. Mater. Res. 91A: 614-622.
- Habraken, W. J. E. Wolke, J. G. C. Jansen, J. A. 2007. Ceramic composites as matrices and scaffolds for drug delivery in tissue engineering. Adv. Drug Deliv. Rev. 59: 234-248.
- Hamanishi, C. Kitamoto, K. Tanaka, S. et al. 1996. A self-setting TTCP-DCPD apatite cement for release of vancomycin. J. Biomed. Mater. Res. Part B: Appl. Biomater. 33: 139-143.

- Hancox, N. M. 1972. Biology of bone, Cambridge University Press, London. pp 18-35.
- Hench, L. L. 1998. Biomaterials: a forecast for the future. Biomaterials 19: 1419-1423.
- Hench, L. L. Ethridge, E. C. 1982. Biomaterials, An interfacial approach. Academic Press, London.
- Hench, L. L. and Jones, J. R. 2005. Biomaterials, artificial organs and tissue engineering. Woodhead Publishing Limited, Cambridge, England, pp 26-36.
- Hench L. L. and West, J. K. 1990. The sol-gel process. Chem. Rev. 90: 33-72.
- Hench, L. L. Wilson, J. 1993. An introduction to bioceramics. World Scientific, Singapore. pp 1-24.
- Heller, W. 1980. Polymer colloids II, Plenum, New York.
- Henisch, H. K. 1970. Crystal growth in gels. Pennsylvania State University Press, Pennsylvania.
- Hentrich, R. L. Jr. Graves, G. A. Jr. Stein, H. G. et al. 1971. An evaluation of inert and resorbable ceramics for further clinical applications. J. Biomed. Mater. Res. 5: 25-51.
- Hessle, L. Johnson, K. A. Anderson, H. C. et al. 2002. Tissue-nonspecific alkaline phosphatase and plasma cell membrane glycoprotein-1 are central antagonistic regulators of bone mineralization. PNAS 99: 9445–9449.
- Higuchi, T. 1963. Mechanism of Sustained-Action Medication. J. Pharm. Sci., 52: 1145-1149.
- Ho, W.-J. Yuan C.-J. and Ohara, R. 2006. Application of SiO_2–poly(dimethylsiloxane) hybrid material in the fabrication of amperometric biosensor. Analytica. Chimica. Acta. 572: 248-252.
- Hofmann M. P. 2003. Physikalische Charakterisierung von Calciumphosphat-Pulvern zur Einstellung von Prozessparametern für die Herstellung von Knochenzement. PhD thesis, University of Wüerzburg.
- Hsieh, M.-F. Perng, L.-H. Chin, T.-S. et al. 2001. Phase purity of sol-gel derived hydroxyapatite ceramic. Biomaterials. 22: 2601-2607.
- Hu, M. Noda, S. Okubo, T. et al. 2001. Structure and morphology of self assembled 3-mercaptopropyltrimethoxysilane layers on silicon oxide. Appl. Surf. Sci. 181: 307-316.
- Huang, X. Brazel, C. S. 2001. On the importance and mechanisms of burst release in matrix-controlled drug delivery systems. J. Controlled Release 73: 121-136.

- Itaka, K. Ohba, S. Miyata, K. et al. 2007. Bone regeneration by regulated in vivo gene transfer using biocompatible polyplex nanomicelles. Mol. Ther. 15: 1655-1662.
- Ishika K. and Eanes, E. D. 1993. The hydrolysis of anhydrous dicalcium phosphate into hydroxyapatite. J. Dent. Res. 72: 474-480.
- Ishizaki, J. Waki, Y. Takahashi-Nishioka, T. et al. 2009. Selective drug delivery to bone using acidic oligopeptides. J. Bone Miner. Metab. 27: 1-8.
- Itokazu, M. Yang, W. Aoki, T. et al. 1998. Synthesis of antibiotic-loaded interporous hydroxyapatite blocks by vacuum method and in vitro drug release testing. Biomaterials 19: 817-819.
- Jain, T. K. Rov, I. De, T. K. et al. 1998. Nanometer silica particles encapsulating active compounds: A novel ceramics drug carrier. J. Am. Chem. Soc. 120: 11092-11095.
- Jiang, P. J. Patel, S. Gbureck, U. et al. 2008. A comparison of the efficacy of hydroxyapatite based cements and gels as drug delivery matrices. Key Eng. Mater. 361: 327-330.
- Jillavenkatesa, A. Condrate Sr, R. A. 1998. Sol-gel processing of hydroxyapatite, J. Mater. Sci. 33: 4111-4119.
- Jin, W. Brennan, J. D. 2002. Properties and applications of proteins encapsulated within sol-gel derived materials. Anal. Chim. Acta. 461: 1–36.
- Joosten, U. Joist, A. Gosheger, G. et al. 2005. Effectiveness of hydroxyapatite-vancomycin bone cement in the treatment of *Staphylococcus aureus* induced chronic osteomyelitis. Biomaterials 26: 5251-5258.
- Kalita, S. Bhardwaj, J. A. Bhatt, H. A. 2007. Nanocrystalline calcium phosphate ceramics in biomedical engineering. Mater. Sci. Eng. C 27: 441-449.
- Kadnikova, E. N. Kostić, N. M. 2002. Oxidation of ABTS by hydrogen peroxide catalyzed by horseradish peroxidase encapsulated into sol-gel glass: Effects of glass matrix on reactivity. J. Mol. Catal. 18: 39-48.
- Kandimalla, V. B. Tripathi, V. S. and Ju, H. 2006. Immobilization of biomolecules in sol-gels: biological and analytical applications. Crit. Rev. Anal. Chem. 36: 73-1006.
- Kanellakopoulou, K. Galanakis, N. Giamarellos-Bourboulis, E. J. et al. 2000. Treatment of experimental osteomyelitis caused by methicillin-resistant *Staphylococcus aureus* with biodegradable system of lactic acid polymer releasing pefloxacn. J. Antimicrob. Chemother. 46:311-314.

- Kathuria, N. Tripathi, A. Kar, K. K. et al. 2009. Synthesis and characterization of elastic and macroporous chitosan-gelatin cryogels for tissue engineering. Acta. Biomaterialia. 5: 406–418.
- Kendall, K. 2001. Molecular adhesion and its applications. Kluwer Academic, New York. pp 245-266.
- Kim, H. W. Knowles, J. C. Kim, H. E. 2005. Porous scaffolds of gelatin-hydroxyapatite nanocomposites obtained by biomimetic approach: Characterization and antibiotic drug release. J. Biomed. Mater. Res. Part B: Appl. Biomater. 74B: 686-698.
- Kimakhe, S. Bohic, S. Larosse, C. et al. 1999. Biological activities of sustained polymyxin B release from calcium phosphate biomaterial prepared by dynamic compaction: An in vitro study. J. Biomed. Mater. Res. 47: 18-27.
- Kirihara, K. Asai, Y. Ogawa, S. Noguchi, T. Hatano, A. Hirai, Y. 2007. A mild and environmentally benign oxidation of thiols to disulfides. Synthesis 21: 3286-3289.
- Kitsugi, T. Nakamara, T. Oka, M. et al. 1995. Bone-bonding behavior of three heat-treated silica gels implanted in mature rabbit bone. Calcif. Tissue. Int. 57: 155-160
- Kitsugi, T. Yamamuro, T. Nakamura, T. et al. 1993. Four calcium phosphate ceramics as bone substitutes for non-weight-bearing, Biomaterials 14: 216-224.
- Kokubo, T. (Ed.) 2008. Bioceramics and their clinical applications. Woodhead Publishing in Material, Japan. pp 3-27.
- Komleva, V. S. Barinova, S. M. Koplok, E. V. 2002. A method to fabricate porous spherical hydroxyapatite granules intended for time-controlled drug release. Biomaterials 23:3449-3454.
- Korkusuz, F. Uchida, A. Shinto, Y. et al. 1993. Experimental implant-related osteomyelitis treated by antibiotic-calcium hydroxyapatite ceramic composites. J. Bone Joint Surg. [Br], 75B:111 -114.
- Koutsopoulos, S. 2002. Synthesis and characterization of hydroxyapatite crystals: A review study on the analytical methods. J. Biomed. Mater. Res. 62:600-612.
- Kovtun, A. Heumann, R. Epple, M. 2009. Calcium phosphate nanoparticles for the transfection of cells. Bio-Med. Mater. Eng. 19: 241-247.
- Kroese-Deutman, H. C. Ruhé, P.Q. Spauwen, P. H. M. et al. 2004. Bone inductive properties of rhBMP-2 loaded porous calcium phosphate cement implants in cranial defects in rabbits. Biomaterials 25: 2123-2132.
- Kumar, R. Prakash, K. H. Cheang, P. et al. 2004. Temperature driven morphological changes of chemically precipitated hydroxyapatite nanoparticles. Langmuir 20: 5196-5200.

- Laranjo, M. T. Stefani, V. Benvenutti, E. V. et al. Synthesis of ORMOSIL silica/rhodamine 6G: powders and compacts. 2007. J. Non-Cryst. Solids. 353: 24-30.
- Lee, S. C. Choi, H. W. Lee, H. J. et al. 2007. In-situ synthesis of reactive hydroxyapatite nano-crystals for a novel approach of surface grafting polymerization. J. Mater. Chem. 17: 174-180.
- Lee, Y. Hahm, Y. M. Lee, D. H. et al. 2006. Preparation and and characterization of macroporous carbonate-substituted hydroxyapatite scaffold. Ind. Eng. Chem. Res. 47: 2618-2622.
- LeGeros, R. Z. 2008. Calcium phosphate-based osteoinductive materials. Chem. Rev. 108: 4742-4753.
- LeGeros, R. Z. Apatite in biological systems. 1981. Prog. Crystal. Growth. 4: 1-45.
- Lehr, J. R. Brown, E. H. Smith, J. P. et al. 1963. Crystallographic properties of fertilizer compounds. Chemical Engineering Bulletin No 6. Muscle Shoals, Tennessee Valley Authority.
- Lim, F. 1985. Biomedical application of microencapsulation. CRC Press, Florida.
- Lin, T.-Y. Wu, C.-H. Brennan, J. D. 2007. Entrapment of horseradish peroxidase in sugar-modified silica monoliths: toward the development of a biocatalytic sensor. Biosensors and Bioelectronics 22: 1861-1867.
- Liu, D. M. Yang, Q. Troczynski, T. et al. 2002. Structural evolution of sol-gel-derived hydroxyapatite. Biomaterials 23: 1679-1687.
- Liu, Q. de Wijn, J. R. van Blitterswijk, C. A. 1998. Covalent bonding of PMMA, PBMA, and poly(HEMA) to hydroxyapatite particles. J. Biomed. Mater. Res. 40: 257–263,
- Liu, Q. de Wijn, J. R. de Groot, K. et al. 1998. Surface modification of nano-apatite by grafting organic polymer. Biomaterials. 19: 1067-1072.
- Liu, D. Troczynski, M. T. Tseng, W. J. 2001. Water-based sol-gel synthesis of hydroxyapatite: process development. Biomaterials 22: 1721-1730.
- Lobel, K. D. Hench, L. L. 1998. In vitro adsorption and activity of enzymes on the reaction layers of bioactive glass substrate. J. Biomed Mater. Res. 39: 575-579.
- Lode, A. Reinstorf, A. Bernhardt, A. et al. 2008. Heparin modification of calcium phosphate bone cements for VEGF functionalization. J Biomed Mater Res 86A: 749–759.
- Lode, A. Wolf-Brandstetter, C. Reinstorf, A. et al. 2007. Calcium phosphate bone cements functionalized with VEGF: release kinetics and biological activity. J. Biomed. Mater. Res. Part A 81A: 474-483.
- Loll, P. Axelsen, P. 2000. The structural biology of molecular recognition by vancomycin. Ann. Rev. Biophys. Biomol. Struct. 29: 265-289.

- Lu, H. Qu, Z. Zhou, Y.-C. 1998. Preparation and mechanical properties of dense polycrystalline hydroxyapatite through freeze-drying. J. Mater. Sci: Mater. Med. 9: 583- 587.
- Mark Jr., S. C. Popoff, S. N. 1988. Bone cell biology: The regulation of development, structure, and function in the skeleton. Am. J. Anat. 183: 1-4.
- Maitra, A. 2005. Calcium phosphate nanoparticles: second-generation nonviral vectors in gene therapy. Expert. Rev. Mol. Diagn. 5: 893-905.
- Masahiro, F. Kumi, S. Kaoru, H. et al. 2007. Direct encapsulation of BSA and DNA into silica microcapsules (hollow spheres). J. Biomed. Mater. Res. 81A: 103-112.
- Mastersizer 2000: intergrated systems for particle sizing. 2000. Malvern Ltd. pp 2.1-2.2.
- Miller, S. A. Hong, E. D. Wright, D. 2006. Rapid and efficient enzyme encapsulated in a dendrimer silica nanocomposite. Macromol. Biosci. 6: 839-845.
- Miller, S. C. 1987. The bone lining cell: A distinct phenotype? Calcif. Tissue. Int. 41: 1-5.
- Monroe, E. A. Votava, W. Bass, D. B. et al. 1971. New calcium phosphate ceramic material for bone and tooth implants. J. Dent. Res. 50: 860-861.
- Mooney, R. W. Aia, M. 1961. Alkaline earth phosphates. Chem. Rev. 61: 433-462.
- Mornet, E. 2008. Hypophosphatasia. Best practice & research clinical rheumatology. 22: 113-127.
- Müller, R. 1972. Spectrochemical analysis by x-ray fluorescence, Adam Hilger Ltd. London. pp 1-7.
- Nakamura M. and Ishimura K. 2007 Synthesis and characterization of organosilica nanoparticles prepared from 3-mercaptopropyltrimethoxysilane as the single silica source. J. Phys. Chem. C 111:18892-18898.
- Nelson, M. Balasundaram, G. Webster, T. J. 2006. Increased osteoblast adhesion on nanoparticulate crystalline hydroxyapatite functionalized with KRSR. Int. J. Nanomed. 1: 339-349.
- Nicoll, S. B. Radin, S. Santost, E. M. et al. 1997. In vitro release kinetics of biologically active transforming growth factor-ß1 from a novel porous glass carrier. Biomaterials 18: 853-859.
- Nishioka, T. Tomatsu, S. Gutierrez, M. A. et al. 2006. Enhancement of drug delivery to bone: Characterization of human tissue-nonspecific alkaline phosphatase tagged with an acidic oligopeptide. Mol. Gen. Metab. 88: 244-255.
- Nordström, E. G. Karlsson, K. H. Carbonate-doped hydroxyapatite. 1990. J. Mater. Sci. Mater. Med. 1:182-184.

- Norton, J. Malik, K. R. Darr J. A. et al. 2006. Recent developments in processing and surface modification of hydroxyapatite. Adv. Appl. Ceram. 105: 113-139.
- Obadia, L. Amador, G. Daculsi, G. et al. 2003. Calcium-deficient apatite: influence of granule size and consolidation mode on release and in vitro activity of vancomycin. Biomaterials 24: 1265-1270.
- Omae, H. Mochizuki, Y. Yokoya, S. et al. 2006. Effects of interconnecting porous structure of hydroxyapatite ceramics on interface between grafted tendon and ceramics. J. Biomed. Mater. Res. 79A: 329–337.
- Omelon, S. Georgiou, J. Henneman, Z. J. et al. 2004. Control of vertebrate skeletal mineralization by polyphosphates. PLoSONE. 4: 1-16.
- Orrego, C. E. Valencia, J. S. 2009. Preparation and characterization of chitosan membranes by using a combined freeze gelation and mild cross linking method. Bioprocess. Biosyst. Eng. 32:197–206.
- Osathanon, T. Giachelli, C. M. Somerman, M. J. 2009. Immobilization of alkaline phosphatase on microporous nanofibrous fibrin scaffolds for bone tissue engineering. Biomaterials 30: 4513-4521.
- Otsuka, M. Nakahigashi, Y. Matsuda, Y. et al. 1994. A novel skeletal drug delivery system using a self-setting calcium phosphate cement: VII. Effect of biological factors on indomethacin release from the cement loaded on bovine bone. J. Pham. Sci. 83: 1569-1573.
- Paital S. R. Dahotre, N. B. 2008. Review of laser based biomimetic and bioactive Ca-P coatings, Mater. Sci. and Tech. 24: 1144-1161.
- Palard, M. Champion, E. Foucaud, S. 2008. Synthesis of silicated hydroxyapatite $Ca_{10}(PO_4)_{6-x}(SiO_4)_x(OH)_{2-x}$. J. Solid. State. Chem. 181: 1950-1960.
- Palazzo, B. Sidoti, M. C. Roveri, N. et al. 2005. Controlled drug delivery from porous hydroxyapatite grafts: An experimental and theoretical approach. Mater. Sci. Eng. C 25: 207-213.
- Pan, H.-B. Darvell, B. W. 2009. Calcium phosphate solubility: the need for re-evaluation, Cryst. Growth Des. 9: 639-645.
- Park, J. B. Bronzino, J. D. 2003. Biomaterials principles and applications. CRC Press, London. pp 21-53.
- Pierre, A. C. 1997. Porous sol-gel Ceramics, Ceram. Int. 23: 229-238.
- Pietak, A. M. Reid, J. W. Stott, M. J. et al. 2007. Silicon substitution in the calcium phosphate bioceramics. Biomaterials 28: 4023-4032.
- Plieva, F. M. Andersson, J. Galaev, I. Y. et al. 2004. Characterization of polyacrylamide based monolithic columns. J. Sep. Sci. 27: 828–836.

- Plieva, F. M. Galaev, I. Y. Noppe W. et al. 2008. Cryogel applications in microbiology. Trends Microbiol. 16: 543-551.
- Potoczek, M. Zima, A. Paszkiewicz, Z. et al. 2009. Manufacturing of highly porous calcium phosphate bioceramics via gel-casting using agarose. Ceram. Int. 35: 2249-2254.
- Price N. C. and Stevens, L. 1999. Fundamentals of enzymology: The cell and molecular biology of catalytic proteins, Oxford University Press Inc. New York. pp 121-124.
- Putlyaev V. I. and Safronova, T. V. 2006. A new generation of calcium phosphate biomaterials: the role of phase and chemical compositions. Glass and Ceramics 63: 99-102.
- Radin, S. Campbell, J. T. Ducheyne, P. et al. 1997. Calcium phosphate ceramic coatings as carriers of vancomycin. Biomaterials 18: 777-782.
- Radin, S. Ducheyne, P. Kamplain, T. et al. 2001. Silica sol-gel for the controlled release of antibiotics. I. Synthesis, characterization, and in vitro release. J. Biomed. Mater. Res. 57:313-320.
- Radin, S. Ducheyne, P. 2007. Controlled release of vancomycin from thin sol-gel films on titanium alloy fracture plate material. Biomaterials 28: 1721-1729.
- Radin, S. Ducheyne, P. 2008. Sol-gel formulations for the controlled delivery of growth factors and proteins. Proceedings of the 8th World Biomaterial Congress, Amsterdam, May 28-June1 2008. 047-growth factor: 1298.
- Ratner, B. Hoffman, D. Schoen, A. S. F. J. et al. 2004. Biomaterials science: An introduction to materials in medicine. Academic Press, London. pp 153-170.
- Ramay, H. R. Zhang, M. 2003. Preparation of porous hydroxyapatite scaffolds by combination of the gel-casting and polymer sponge methods. Biomaterials 24: 3293-3302.
- Ravaglioli A. and Krajewski, A. 1992. Bioceramics: materials, properties, applications, Chapman & Hall, London. pp 1-15.
- Rawat, M. Singh, D. Saraf, S. et al. 2008. Development and in vitro evaluation of alginate gel-encapsulated, chitosan-coated ceramic nanocores for oral delivery enzyme. Drug Dev. Ind. Pharm. 34: 181-188.
- Reynolds, P. E. 1989. Structure, biochemistry and mechanism of action of glycopeptide antibiotics. Eur. J. Clinc. Microbiology & Infectious disease, 8: 943-950.
- Riggs, B. L. Melton, L. J. 1992. Drug therapy the prevention and treatment of osteoporosis. N. Engl. J. Med. 3: 620-627.

- Saito, T. Takeuchi, R. Hirakawa, K. et al. 2002. Slow-Releasing potential of vancomycin-loaded porous hydroxyapatite blocks implanted into MRSA osteomyelitis. J. Biomed. Mater. Res. Appl. Biomater. 63: 245-251.
- Saltzman, W. M. 2001. Drug Delivery-Engineering Principles for drug therapy. Oxford University Press, New York. pp 23-24, 69, 235.
- Sánchez-Salcedo, S. Werner, J. Vallet-Regí, M. 2008. Hierarchical pore structure of calcium phosphate scaffolds by a combination of gel-casting and multiple tape-casting methods. Acta Biomater. 4: 913–922.
- Santos, C. Luklinska, Z. B. Clarke, R. L. et al. 2001. Hydroxyapatite as a filler for dental composite materials: mechanical properties and *in vitro* bioactivity of composites. J. Mater. Sci. Mater. Med. 12: 565-573.
- Seshima, H. Yoshinari, M. Takemoto, S. et al. 2006. Control of bisphosphonate release using hydroxyapatite granules. J. Biomed. Mater. Res. Part B: Appl. Biomater. 78B: 215-221.
- Shackelford, J. F. 1999. Bioceramics volume 1. Gordon and Breach Science, Amsterdam, The Netherlands. pp 5-7, 31-38.
- Shi, D. 2004. Biomaterials and tissue engineering. Springer, New York. pp 1-26.
- Shinto, Y. Uchida, A. Korkusuz, F. et al. 1992. Calcium hydroxyapatite ceramic used as a delivery system for antibiotics. J. Bone Joint Surg. [Br.] 74B: 600-604.
- Sigma production information bicinchoninic acid protein assay kit. 2001. Sigma Ltd.
- Silva, R. A. Carmona-Ribeiro, A. M. Petri, D. F. S. 2007. Adsorption behavior and activity of horseradish peroxidise polysaccharide-decorated particles. Int. J. Biol. Macromol. 41: 404-409.
- St. Pierre PDS 1955. The preparation of dicalcium phosphate dehydrate and calcium pyrophosphate. J. Am. Chem. Soc. 77: 2197-2198.
- Stallmann, H. P. Faber, C. Bronckers, A. L. J. J. et al. 2006. In vitro gentamicin release from commercially available calcium-phosphate bone substitutes influence of carrier type on duration of the release profile. B. M. C. Musculosket. Disord. 7: 1-8.
- Stigter, M. Bezemer, J. de Groot, K. et al. 2004. Incorporation of different antibiotics into carbonated hydroxyapatite coatings on titanium implants, release and antibiotic efficacy. J. Controlled Release. 99: 127-137.
- Suchanek W. Yoshimura, M. 1998. Processing and properties of hydroxyapatite-based biomaterials for use as hard tissue replacement implants. J. Mater. Res. 13: 94-117.
- Tampieri, A. Celotti, G. Sprio, S. et al. 2001. Porosity-graded hydroxyapatite ceramics to replace natural bone. Biomaterials. 22: 1365-1370.

- Tanaka, H. Yasukawa, A. Kandori, K. et al. 1997. Modification of calcium hydroxyapatite using alkyl phosphates. Langumuir. 13: 821-826.
- Tanaka, H. Futaoka, M. and Hino, R. 2004. Surface modification of calcium hydroxyapatite with pyrophosphoric acid. J. Colloid Interface Sci. 269: 358–363.
- Teitelbaum, S. L. Bon e resorption by osteoclasts. 2000. Science. 289: 1504-1508.
- Teller, M. Gopp, U. Neumann, H.-G. et al. 2007. Release of gentamicin from bone regenerative materials: An in vitro study. J Biomed Mater Res Part B: Appl. Biomater. 81B: 23-29.
- Thian, E. S. Huang, J. Vickers, M. E. et al. 2006. Silicon-substituted hydroxyapatite (SiHA): A novel calcium phosphate coating for biomedical applications. J. Mater. Sci. 41: 709–717.
- Tovborg, J. A. and Rathlev, J. 1953. Calcium hydrogen orthophosphate 2-hydrate and calcium hydrogen orthophosphate. Inorg. Synth. 4: 19-22.
- Trevan, M. D. 1980. Immobilized Enzymes: an introduction and applications in biotechnology. John Wiley & Sons, Chichester.
- Ulman, A. 1991. An introduction to ultrathin organic films: From Langmuir-Blodgett to self assembly. Academic Press, New York.
- Urist, M. R. O'Connor, B. T. Burwell, R. G. 1994. Bone grafts, derivatives & Substitutes. Butterworth-Heinemann Ltd., Cambridge, UK. pp 123-131.
- Vallet- Regí, M. 2001. Ceramics for medical applications. J. Chem. Soc. Dalton Trans. 97-108.
- Vaughan, J. 1981. The physiology of bone, third edition, Oxford Science Publications, Oxford. pp 1-14.
- Vecsei, V. Barquet, A. 1981. Treatment of chronic osteomyelitis by necretomy and gentamicin-PMMA beads. Clin. Orthop. Relat. Res. 159: 201-207.
- Venugopal, J. R. Low, S. Choon, A. T. et al. 2008. Nanobioengineered electrospun composite nanofibers and osteoblasts for bone regeneration, Artificial organs. 32: 388-397.
- Vollet, D. R. Donatti, D. A. Ibańez Ruiz, A. 2004. Comparative study using small-angle x-ray scattering and nitrogen adsorption in the characterization of silica xerogels and aerogels. Phys. Rev. B. 69: 064202-1-6.
- Voss, R. Brook, M. A. Thompson, J. et al. 2007. Non-destructive horseradish peroxidase immobilization in porous silica nanoparticles. J. Mater. Chem. 17: 4854-4863.
- Wang, G. Xu, J.-J. Chen, H.-Y. et al. 2003. Amperometric hydrogen peroxide biosensor with sol-gel/chitosan network-like film as immobilization matrix. Biosensors Bioelectron. 18: 335-343.

- Wang. Y. Caruso, F. 2005. Mesoporous silica spheres as supports for enzyme immobilization and encapsulation. Chem. Mater. 17: 953-961.
- Webb, P. A. 2001. Volume and density determinations for particle technologist, Micromeritics Instrument Corp.
- Weber, C. Reiss, S. Langer, K. 2000. Preparation of surface modified protein nanoparticles by introduction of sulfhydryl groups. Int. J. Pharm. 211: 67-78.
- Wei, Y. Xu, J. Feng, Q. et al. 2000. Encapsulation of enzymes in mesoporous host materials via the nonsurfactant-templated sol–gel process. Mater. Lett. 44: 6-11.
- Wilkinson, J. M. Scott, B. W. Clarke, A. M. et al. 1998. Surgical stabilisation of the lower limb in osteogenesis imperfecta using the Sheffield telescopic intramedullary rod system. J Bone Joint Surg [Br] 80B: 999-1004.
- Woodward, J. 1985. Immobilised cells and enzymes a practical approach. IRL Press, Oxford, England.
- Wright, J. E. I. Gittens, S. Bansal, A.G. et al. 2006. A comparison of mineral affinity of bisphosphonate-protein conjugates constructed with disulfide and thioether linkages. Biomaterials 27: 769-784.
- Xu, Q. G. Tanaka, Y. Czernuszka, J. T. 2007. Encapsulation and release of a hydrophobic drug from hydroxyapatite coated liposomes. Biomaterials 28: 2687-2694.
- Xu, Y. Cruz, T. Pritzker, P. 1991. Alkaline phosphatase dissolves calcium pyrophosphate dihydrate crystals. J. Rheumatol. 18: 1606-1610.
- Yang, Y.-Z. Kim, K.-H. Ong, J. L. 2005. A review on calcium phosphate coatings produced using a sputtering process an alternative to plasma spraying. Biomaterilas 26: 327-337.
- Zelinski, B. J. J. and Uhlmann, D.R. 1984. Gel technology in ceramics. J. Phys. Chem. Solids. 45: 1069-1090.
- Zhang, Y. Yokogawa, Y. 2008. Effect of drying conditions during synthesis on the properties of hydroxyapatite powders. J. Mater. Sci.: Mater. Med. 19: 623–628.
- Zilch, H. Lambiris, E. 1986. The sustained release of cefotaxim from a fibrin-cefotax compound in treatment of osteitis. pharmaco-kinetic study and clinical results. Acta. Orthop. Trauma. Surg. 106: 36-41.